

**FERROELECTRIC, PIEZOELECTRIC AND PYROELECTRIC
PROPERTIES OF SOL-GEL DERIVED SODIUM BISMUTH
TITANATE AND CERAMIC POWDER-POLYMER
COMPOSITE**

NURAIN BINTI AB. HALIM

**FACULTY OF SCIENCE
UNIVERSITY OF MALAYA
KUALA LUMPUR**

2018

**FERROELECTRIC, PIEZOELECTRIC AND
PYROELECTRIC PROPERTIES OF SOL-GEL DERIVED
SODIUM BISMUTH TITANATE AND CERAMIC
POWDER-POLYMER COMPOSITE**

NURAIN BINTI AB. HALIM

**THESIS SUBMITTED IN FULFILMENT OF THE
REQUIREMENTS FOR THE DEGREE OF DOCTOR OF
PHILOSOPHY**

**DEPARTMENT OF PHYSICS
FACULTY OF SCIENCE
UNIVERSITY OF MALAYA
KUALA LUMPUR**

2018

UNIVERSITY OF MALAYA

ORIGINAL LITERARY WORK DECLARATION

Name of Candidate : **NURAIN BINTI AB. HALIM**

Registration/Matric No : **SHC130019**

Name of Degree : **DOCTOR OF PHILOSOPHY**

Title of Project Paper/Research Report/Dissertation/Thesis ("this Work"):

**FERROELECTRIC, PIEZOELECTRIC AND PYROELECTRIC
PROPERTIES OF SOL-GEL DERIVED SODIUM BISMUTH TITANATE
AND CERAMIC POWDER-POLYMER COMPOSITE**

Field of Study: EXPERIMENTAL PHYSICS

I do solemnly and sincerely declare that:

- (1) I am the sole author/writer of this Work;
- (2) This Work is original;
- (3) Any use of any work in which copyright exists was done by way of fair dealing and for permitted purposes and any excerpt or extract from, or reference to or reproduction of any copyright work has been disclosed expressly and sufficiently and the title of the Work and its authorship have been acknowledged in this Work;
- (4) I do not have any actual knowledge nor do I ought reasonably to know that the making of this work constitutes an infringement of any copyright work;
- (5) I hereby assign all and every rights in the copyright to this Work to the University of Malaya ("UM"), who henceforth shall be owner of the copyright in this Work and that any reproduction or use in any form or by any means whatsoever is prohibited without the written consent of UM having been first had and obtained;
- (6) I am fully aware that if in the course of making this Work I have infringed any copyright whether intentionally or otherwise, I may be subject to legal action or any other action as may be determined by UM.

Candidate's Signature

Date:

Subscribed and solemnly declared before,

Witness's Signature

Date:

Name:

Designation:

**FERROELECTRIC, PIEZOELECTRIC AND PYROELECTRIC
PROPERTIES OF SOL-GEL DERIVED SODIUM BISMUTH TITANATE
AND CERAMIC POWDER-POLYMER COMPOSITE**

ABSTRACT

The dielectric, piezoelectric, pyroelectric and ferroelectric properties of sodium bismuth titanate (BNT) ceramics and its polymer composites were studied. This work is divided into three parts. In the first part, the BNT nanoceramics of molar composition 50/50 ($\text{Na}_{0.5}\text{Bi}_{0.5}\text{TiO}_3$) was synthesized by a sol-gel processing method. The BNT nanoceramics were sintered at four different sintering temperatures; 900 °C, 1000 °C, 1100 °C and 1200 °C. BNT crystallized in the rhombohedra perovskites structure where $\text{Na}_{0.5}\text{Bi}_{0.5}\text{TiO}_3$ was obtained from the precursor gel by heating at 700 °C for 2 hours in air. The BNT nanoceramics sintered at 1100 °C temperature exhibits high crystallinity, good dielectric properties (at 1 kHz, $\epsilon' = 885$, $\tan \delta = 0.03$, $T_c = 370$ °C), piezoelectric properties ($k_{33} = 0.39$, $c_{33} = 170$ GPa, $e_{33} = 12.6$ C/m², $d_{33} = 74$ pC/N), high remnant polarization ($P_r = 47$ $\mu\text{C}/\text{cm}^2$) and low coercive field ($E_c = 55$ kV/cm). The pyroelectric coefficient, p obtained after effective poling process near depolarization temperature, T_d and field-cooled to room temperature improved tremendously (625 $\mu\text{C}/\text{m}^2\text{K}$) compared to those samples poled by hysteresis loop measurement which is only 141 $\mu\text{C}/\text{m}^2\text{K}$. In the second part, the pure BNT nanopowders doped with various weight percentages of CeO_2 from 0.0 - 5.0 wt.% were prepared by using solid state method. The BNT doped ceramic samples were sintered at 1100 °C. X-ray analysis shows that CeO_2 diffuses into the lattice of BNT during sintering process and form morphotropic phase boundary (MPB) between rhombohedral and tetragonal phase structure. The electrical properties of CeO_2 doped BNT ceramics were greatly improved compared to that of pure BNT.

For example, the 0.6 wt.% of CeO₂ ceramic exhibits high dielectric constant, $\varepsilon' = 1284$ at 10 kHz, high piezoelectric constant ($d_{33} = 90$ pC/N) and enhanced coupling factor ($k_p = 0.44$) at room temperature. The remnant polarization, P_r increased to 56 $\mu\text{C}/\text{cm}^2$ and the coercive field, E_c (53 kV/cm) is reduced as well. Moreover, the pyroelectric coefficient, p improved to 640 $\mu\text{C}/\text{m}^2\text{K}$. Finally, in the third part of this research, the optimized BNT doped with 0.6 wt.% of CeO₂ was mixed into P(VDF-TrFE) copolymer to form polymer/ceramic composites. Five different volume fractions ($\phi = 0.05$ -0.25) ceramic powder were incorporated into the polymer. The nanocomposite thin films were prepared on a glass substrate by spin coating method tested for dielectric, piezoelectric, pyroelectric and ferroelectric. Theoretical models such as Maxwell, Clausius-Mossotti, Furukawa and the effective medium theory (EMT) were employed to describe the effective dielectric permittivity of the composite. The incorporation of 0.2 volume fraction of BNT-0.6 CeO₂ into P(VDF-TrFE) as a nanocomposite films significantly enhanced the pyroelectric and ferroelectric properties of the P(VDF-TrFE) films to 43 $\mu\text{C}/\text{m}^2\text{K}$ and 166 mC/m². The piezoelectric constant, d_{33} of 0.2 volume fraction of P(VDF-TrFE) /BNT-0.6 CeO₂ bulk film observed after poling in the opposite direction was 49 pC/N.

Keywords: Sol-gel method, Polymer/ceramic nanocomposite, Ferroelectric, Pyroelectric, Piezoelectric properties

PENCIRIAN FEROELEKTRIK, PIZOELEKTRIK DAN PIROELEKTRIK
PENGHASILAN SOL-GEL NATRIUM BISMUTH TITANAT DAN
KOMPOSIT SERBUK SERAMIK-POLIMER

ABSTRAK

Kajian terhadap sifat-sifat dielektrik, pizoelektrik, piroelektrik dan feroelektrik bagi seramik natrium bismuth titanat (BNT) dan komposit polimernya. Dalam kajian ini terbahagi kepada tiga bahagian. Dalam bahagian pertama, nanoseramik BNT pada komposisi molar 50/50 ($\text{Na}_{0.5}\text{Bi}_{0.5}\text{TiO}_3$) telah dihasilkan dengan menggunakan kaedah sol-gel. Nanoseramik BNT disinter pada empat suhu sinter yang berbeza iaitu pada 900 °C, 1000 °C, 1100 °C and 1200 °C. Penghabluran BNT berstruktur perovskit rombohedral di mana $\text{Na}_{0.5}\text{Bi}_{0.5}\text{TiO}_3$ terhasil daripada pemanasan gel BNT pada suhu 700 °C selama dua jam di udara. Seramik BNT pada suhu sinter 1100 °C menunjukkan penghabluran yang tinggi, sifat dielektrik yang baik (pada 1 kHz, $\epsilon' = 885$, $\tan \delta = 0.03$, $T_c = 370$ °C), sifat pizoelektrik ($k_{33} = 0.39$, $c_{33} = 170$ GPa, $e_{33} = 12.6$ C/m², $d_{33} = 74$ pC/N), pengutuban remanen yg tinggi ($P_r = 47$ μC/cm²) dan medan daya elektrik yang rendah ($E_c = 55$ kV/cm). Pemalar piroelektrik, p terhasil selepas proses pengkutuban berkesan dilakukan berdekatan dengan suhu pengkutuban, T_d dan di sejuk-medan daya pada suhu bilik, menunjukkan peningkatan ketara (625 μC/m²K) berbanding pengutuban dengan menggunakan gelung hysteresis (141 μC/m²K). Dalam bahagian kedua, serbuknano BNT kemudian didop pada peratusan jisim CeO_2 yang berbeza dari 0.0 - 5.0 wt.% dengan menggunakan kaedah tindak balas pepejal. Suhu sinter iaitu 1100 °C telah digunakan dalam pensinteran seramik BNT dop. Analisis XRD menunjukkan kemasukan CeO_2 ke dalam kekisi BNT semasa proses pensinteran dan penghasilan sempadan fasa morfotropik (MPB) diantara fasa struktur rombohedral dan tetragonal. Sifat elektrikal seramik BNT

didopkan CeO_2 menunjukkan peningkatan yang memberangsangkan berbanding BNT tulen. Sebagai contoh, pada suhu bilik, 0.6 wt.% CeO_2 menghasilkan pemalar dielektrik ($\epsilon' = 1284$) yang tinggi pada 10 kHz, pemalar pizoelektrik ($d_{33} = 90 \text{ pC/N}$) dan peningkatan faktor gandingan ($k_p = 0.44$). Pengutuban remanen, P_r meningkat kepada $56 \mu\text{C/cm}^2$ dan medan daya elektrik, E_c (53 kV/cm) turut berkurang. Selain itu, terdapat sedikit peningkatan pada pemalar piroelektrik iaitu $640 \mu\text{C/m}^2\text{K}$. Dalam bahagian ketiga penyelidikan, sifat elektrik yang optimum yang didapati pada pendopan BNT- 0.6 wt.% CeO_2 telah dipilih untuk dicampurkan ke dalam kopolimer (P(VDF-TrFE)) bagi menghasilkan komposit polimer/seramik. Lima filem nipis nanokomposit dengan pecahan isipadu ceramik yang berbeza ($\phi = 0.05 - 0.25$) telah disediakan di atas substrat kaca dengan menggunakan teknik salutan putaran bagi menguji sifat dielektrik, pizoelektrik, piroelektrik and feroelektrik. Model teori seperti Maxwell, Clausius-Mossotti, Furukawa dan 'Effective medium theory (EMT)' telah diguna pakai untuk menerangkan keberkesanan ketulusan pemalar dielektrik komposit tersebut. Penambahan pecahan isipadu, $\phi = 0.2$ seramik BNT-0.6 CeO_2 ke dalam P(VDF-TrFE) sebagai filem komposit menunjukkan peningkatan ketara pada sifat-sifat piroelektrik dan feroelektrik P(VDF-TrFE) filem iaitu $43 \mu\text{C/m}^2\text{K}$ dan 166 mC/m^2 . Pemalar pizoelektrik, d_{33} pada pecahan isipadu P(VDF-TrFE) /BNT-0.6 CeO_2 filem tebal sebanyak 0.2 yang diperhatikan selepas pengkutuban pada arah bertentangan menunjukkan nilai 49 pC/N .

Kata kunci: Kaedah Sol-gel, Nanokomposit polimer/sermik, Pencirian feroelektrik, Pyroelektrik, Pizoelektrik

ACKNOWLEDGEMENTS

First and the foremost, I would like to thank Allah for giving me strength and good health to keep me moving on to accomplish this research thesis. I would like to express my deepest gratitude to my supervisors, Prof. Dr Wan Haliza Abd. Majid and Dr. Thamir Selvi a/p Velayutham for their guidance, supports, advices, motivation and patience throughout this research work, especially during thesis writing.

Special thanks to my helpful ferroelectric group mates, especially Mrs. Nurul Izzah, Mrs. Nur Azlin, Ms Mardiah, Ms. Hannah and Mr. Kelvin for their cooperation and support during my PhD work. I also wish my gratitude to Professor Dr. Takeo Furukawa from Tokyo University of Science and Dr. Gan Wee Chen for their extensive scientific discussions and willing to guide me in the experiment works. Many thanks to the Low Dimensional Material Research Centre (LDMRC) staff and friends for their contribution, direct or indirect during the completion of my research work.

My heart-felt gratitude and love is due to all my family members, especially my parents (Mr. Ab. Halim bin Baharum and Mdm. Che Puteh bt. Che Mat) for their support and prayers. Last but not least, I am indebted to my husband, Mr. Ba'dli Shah bin Zainal Abidin and my lovely children, Aqil Adli and Aysha Insyirah, who have continuously inspired, encouraged and support me in every single moment in my life. Without their continued support and interest, I would not be able to complete my PhD program.

This work is supported by Post-Graduate Research Fund under project number PG010-2013B affiliated by the University of Malaya and UM.C/C25/HIR/166.

TABLE OF CONTENTS

ABSTRACT.....	iii
ABSTRAK.....	v
ACKNOWLEDGEMENT.....	vii
TABLE OF CONTENTS.....	viii
LIST OF FIGURES.....	xii
LIST OF TABLES.....	xvi
LIST OF SYMBOLS AND ABBREVIATIONS.....	xvii
CHAPTER 1: INTRODUCTION.....	1
1.1 Introduction.....	1
1.2 Historical background.....	2
1.3 Objectives.....	4
1.4 Thesis structure.....	4
CHAPTER 2: LITERATURE REVIEW.....	6
2.1 Introduction.....	6
2.2 Ferroelectric materials.....	6
2.2.1 Crystal structure of BNT ceramics.....	8
2.2.2 Polyvinylidene fluoride-trifluoroethylene, P(VDF-TrFE) polymer.....	10
2.2.3 Ferroelectric composites.....	15
2.3 Dielectric properties.....	17
2.3.1 Analysis of dielectric spectra.....	22
2.4 Piezoelectric properties.....	25
2.4.1 Piezoelectric equations.....	27
2.5 Ferroelectric properties.....	30
2.5.1 Ferroelectric domains.....	31
2.5.2 Ferroelectric hysteresis loop.....	32

2.5.3	Ferroelectric Curie point and its phase transition temperatures.....	35
2.6	Pyroelectric properties.....	36
2.7	Summary.....	39
CHAPTER 3: EXPERIMENTAL METHODOLOGY.....		40
3.1	Introduction.....	40
3.2	Sample preparation.....	40
3.2.1	BNT sol gel.....	40
3.2.2	CeO ₂ doped BNT.....	42
3.2.3	P(VDF-TrFE) / BNT - 0.6 CeO ₂ nanocomposite thin films.....	43
3.2.4	Preparation of 0.2 (P(VDF-TrFE) / BNT - 0.6 CeO ₂) nanocomposite thick films.....	45
3.2.5	Poling process.....	46
3.2.5.1	Experimental considerations.....	48
3.3	Structural analysis.....	49
3.3.1	Thermo gravimetric / differential thermal analysis.....	49
3.3.2	X-ray diffraction.....	49
3.3.3	Fourier transform infrared spectroscopy.....	50
3.3.4	Surface morphology.....	50
3.4	Electrical measurements.....	51
3.4.1	Dielectric measurements.....	51
3.4.2	Piezoelectric measurements.....	53
3.4.3	Ferroelectric measurements.....	53
3.4.4	Pyroelectric measurements.....	55
3.4.4.1	Experimental considerations.....	55
3.5	Summary.....	56

CHAPTER 4: BNT CERAMICS PREPARED BY SOL-GEL METHOD.....57

4.1 Introduction.....	57
4.2 BNT samples at different sintering temperatures.....	58
4.3 Thermogravimetric analysis.....	58
4.4 XRD analysis	59
4.4.1 Determination of crystallite size by Scherrer analysis.....	61
4.5 HRTEM analysis of the nanocrystalline structure.....	61
4.6 FESEM analysis.....	63
4.7 Dielectric properties.....	64
4.8 Piezoelectric properties.....	65
4.9 Ferroelectric properties.....	68
4.10 Pyroelectric properties.....	70
4.11 Discussion.....	72
4.12 Conclusion.....	73

CHAPTER 5: CeO₂ DOPED Na_{0.5}Bi_{0.5}TiO₃ CERAMICS.....75

5.1 Introduction.....	75
5.2 BNT samples at various weight percentages of CeO ₂	75
5.3 XRD analysis.....	76
5.3.1 Determination of crystallite size.....	77
5.4 FESEM analysis.....	79
5.5 Dielectric properties.....	80
5.6 Piezoelectric properties.....	81
5.7 Ferroelectric properties.....	84
5.8 Pyroelectric properties.....	87
5.9 Leakage current analysis.....	89
5.10 Discussion.....	90

5.11 Conclusion.....	92
----------------------	----

CHAPTER 6 : P(VDF-TrFE)/Na_{0.5}Bi_{0.5}TiO₃-0.6 CeO₂ NANOCOMPOSITES..93

6.1 Introduction.....	93
6.2 XRD analysis.....	94
6.3 FTIR analysis.....	95
6.4 FESEM analysis.....	96
6.5 Dielectric properties.....	99
6.6 Ferroelectric properties.....	107
6.7 Pyroelectric properties.....	109
6.8 Leakage current analysis.....	113
6.9 Piezoelectric constant of (P(VDF-TrFE)/BNT-0.6 CeO ₂) thick film at Ø=0.20.....	114
6.10 Conclusion.....	116

CHAPTER 7: CONCLUSION.....118

7.1 Conclusion.....	118
7.2 Future Works.....	121

REFERENCES.....122

LIST OF PUBLICATIONS.....132

LIST OF FIGURES

Figure 2.1	: The relationship between ferroelectrics, pyroelectrics and piezoelectrics.....	7
Figure 2.2	: The crystal structure of BNT (perovskite-type structure); (a) cubic, (b) rhombohedral ferroelectric (F_R) and (c) tetragonal ferroelectric (F_T) structures.....	10
Figure 2.3	: (a) unit, (b) molecule, (c) crystal and (d) bulk structures of PVDF.....	12
Figure 2.4	: Chain conformations and crystal structure of PVDF; green, blue, white colour indicate the fluorine, hydrogen and carbon atom, respectively.....	13
Figure 2.5	: Schematic diagram of crystalline transformation among polymorphs of PVDF due to electrical, mechanical and thermal treatments.....	14
Figure 2.6	: Representative unit of a two-phase system composed of a polymer matrix (phase 1) and ceramic inclusion (phase 2).....	16
Figure 2.7	: Frequency dependence of various polarization mechanisms: (a) The electronic, (b) ionic and (c) orientation polarization mechanisms.....	18
Figure 2.8	: The real, ϵ' (black line) and imaginary, ϵ'' (red line) part of the complex dielectric function for a relaxation process.....	23
Figure 2.9	: Piezoelectricity; the relationship of electric and elastic phenomena.....	26
Figure 2.10	: Piezoelectric effect with a simple molecular model: (a) An unperturbed molecule with no piezoelectric polarization; (b) An external force F , applied to the molecule resulting in to polarization P ; (c) The polarizing effect on the surface when piezoelectric material is subjected to an external force.....	26
Figure 2.11	: Linear electromechanical equations.....	28
Figure 2.12	: A typical P - E hysteresis loop in ferroelectric materials.....	34
Figure 2.13	: A typical S - E loop indicating switching.....	34

Figure 2.14	: A typical triangular waveform and the rectangular short-circuited pyroelectric current from the quasi-static pyroelectric measurements.....	37
Figure 2.15	: The relationships between the thermal, mechanical and electrical properties of a crystal. The solid line illustrates the primary pyroelectric effect (with strain remain constant). The red dash line illustrates the secondary pyroelectric effect when the crystal is freely deformed.....	39
Figure 3.1	: The BNT ceramics (a) solution, (b) gel and (c) dried.....	41
Figure 3.2	: Flowcharts of BNT nanoceramics synthesis by sol gel method.....	42
Figure 3.3	: The BNT ceramics pellet with silver electrodes on the surface.....	43
Figure 3.4	: Fabrication flowchart of the polymer/ceramic composite thin films.....	44
Figure 3.5	: MIM structure of P(VDF-TrFE) / BNT-0.6 CeO ₂ thin films.....	44
Figure 3.6	: The 0.2 (P(VDF-TrFE) / BNT-0.6 CeO ₂) nanocomposite thick film.....	45
Figure 3.7	: A schematic drawing of a polycrystalline ferroelectric with random orientation of grain (a) before and (b) after poling.....	47
Figure 3.8	: Schematic drawing of d.c poling system.....	48
Figure 3.9	: The d_{33} meter (model YE2730A).....	53
Figure 3.10	: Schematic circuit of a Sawyer-Tower bridge for ferroelectric characteristic.....	54
Figure 4.1	: BNT pellets at the different sintering temperatures (a) 900 °C, (b) 1000 °C, (c) 1100 °C and (d) 1200 °C.....	58
Figure 4.2	: TG/DTA curves of BNT dried xerogel.....	59
Figure 4.3	: XRD patterns; (a) BNT powder calcined at 700 °C and sintered pellets at 900 °C, 1000 °C, 1100 °C and 1200 °C. (b) 2θ between 32°- 33°.....	60
Figure 4.4	: (a) and (b) are the HRTEM images of BNT powder and (c) is the histogram of particle size.....	62

Figure 4.5	: FESEM micrograph of (a) a BNT pellet sintered at 1100 °C and (b) is a grain size histogram of BNT pellet.....	63
Figure 4.6	: Frequency and temperature dependence of dielectric constant, ϵ' and dissipation factor, $\tan \delta$ for unpoled and poled BNT ceramic at 10 kHz - 1 MHz.....	65
Figure 4.7	: Piezoelectric resonance spectra of BNT ceramics at (a) various temperatures and (b) observed and fitted dielectric spectra.....	67
Figure 4.8	: Room temperature P - E hysteresis loops of BNT ceramics measured at 5 Hz with various electric fields.....	69
Figure 4.9	: Leakage current density of BNT ceramics.....	70
Figure 4.10	: a) The pyroelectric current of poled BNT ceramics at the heating rate 0.6 °C/min and (b) Graph of I_p versus dT/dt for poled BNT ceramics.....	71
Figure 5.1	: BNT- x wt.% CeO ₂ pellets, ($x = 0.0 - 5.0$).....	76
Figure 5.2	: X-ray diffraction patterns of CeO ₂ doped BNT (a) different amount of CeO ₂ and (b) 2θ between 38° - 48°.....	78
Figure 5.3	: The FESEM micrograph of BNT ceramics with CeO ₂ additives (a) 0.0 wt.%, (b) 0.4 wt.%, (c) 0.8 wt.% and (d) 1.0 wt.%.....	79
Figure 5.4	: Temperature dependence of dielectric constant, ϵ' and dissipation factor, $\tan \delta$ of CeO ₂ doped BNT at 10 kHz.....	81
Figure 5.5	: Piezoelectric resonances at various weight percentages of CeO ₂	83
Figure 5.6	: Dielectric constant, ϵ' and piezoelectric properties of CeO ₂ doped BNT; (i) piezoelectric constant d_{33} , (ii) Young Modulus c_{33} and (iii) mechanical coupling factor k_p	84
Figure 5.7	: P - E hysteresis loops of BNT - x wt.% CeO ₂ ceramics measured at 5 Hz with various electric fields.....	86
Figure 5.8	: (a) P - E hysteresis loops at various weight percentages of CeO ₂ and (b) P_r and E_c of the BNT ceramics as a function of CeO ₂	87
Figure 5.9	: (a) The pyroelectric current of poled BNT-0.6 wt.% CeO ₂ ceramics at the heating rate of 0.6 °C/min and (b) pyroelectric coefficient of BNT ceramics.....	88
Figure 5.10	: Leakage current density of BNT- x wt.% CeO ₂ ceramics.....	89

Figure 5.11	: (a) The replacement of Ce^{4+} ion in the BNT perovskite structure and (b) the distortion of Ce^{4+} influence of electric field.....	91
Figure 6.1	: XRD pattern of (a) P(VDF-TrFE), BNT-0.6 CeO_2 and P(VDF-TrFE) /BNT-0.6 CeO_2 composite, (b) peak intensity of P(VDF-TrFE).....	95
Figure 6.2	: FTIR spectra of P(VDF-TrFE) and composite thin films.....	96
Figure 6.3	: FESEM microstructure of BNT-0.6 CeO_2 ceramics, pure P(VDF-TrFE) and P(VDF-TrFE) /BNT-0.6 CeO_2 with various values of volume fractions, ϕ	98
Figure 6.4	: A schematic diagram of P(VDF-TrFE) /BNT-0.6 CeO_2 composite of (a) 0-3 and (b) 1-3 connectivity.....	99
Figure 6.5	: Dielectric spectra of P(VDF-TrFE) /BNT-0.6 CeO_2 composite films with various volume fractions as measured at room temperature.....	101
Figure 6.6	: Various models of the effective dielectric constant as a function of volume fraction of BNT-0.6 CeO_2 , ϕ	104
Figure 6.7	: Observed (circles) and fitted (solid line) dielectric spectra of P(VDF-TrFE) and P(VDF-TrFE) /BNT-0.6 CeO_2 at 25 °C to 120 °C.....	106
Figure 6.8	: (a) P - E hysteresis loops and (b) remanent polarization, P_r and coercive field, E_c of P(VDF-TrFE) /BNT-0.6 CeO_2 composite films with various volume fractions, ϕ	109
Figure 6.9	: (a) Change in pyroelectric current with time and temperature of $\phi = 0.20$ and (b) pyroelectric coefficient, p with volume fractions.....	112
Figure 6.10	: Leakage current density of P(VDF-TrFE) and P(VDF-TrFE) /BNT-0.6 CeO_2 composite with various volume fractions.....	114
Figure 6.11	: The d_{33} meter measurements.....	116

LIST OF TABLES

Table 2.1	: Symbol of the 32 point groups on crystallography. Remarks: (*) implies that piezoelectric effect may be exhibited and (+) implies that pyroelectric and ferroelectric effects may be exhibited.....	8
Table 4.1	: The BNT ceramics in different synthesis method.....	73
Table 5.1	: The crystallite size of BNT- x wt.% CeO_2	77
Table 6.1	: The P(VDF-TrFE)-based composite systems.....	116

LIST OF SYMBOLS AND ABBREVIATIONS

A	:	Area
C	:	Capacitance
C_0	:	Capacitive component
c_{33}	:	Stiffness compliance constant (Young modulus)
D	:	Electric displacement
d	:	Crystallite size
d_{33}	:	Piezoelectric coefficient
E	:	Electric field
E_c	:	Coercive field
E_0	:	Amplitude of electric field
e	:	Piezoelectric modulus
F	:	Force
f	:	Frequency
f_t	:	Resonance frequency
g	:	Piezoelectric coefficient
h	:	Piezoelectric modulus
hkl	:	Diffraction peak at half-maximum intensity
I	:	Current
I_c	:	Capacitive component of the current
I_p	:	Pyroelectric current
I_R	:	Resistive component of the current
J	:	Current density
k	:	Shape factor / Scherrer constant
k_{33}	:	Electromechanical coupling coefficient
L	:	Inductance

P	:	Polarization
P_r	:	Remanent polarization
P_s	:	Spontaneous polarization
p	:	Dipole moment
p	:	Pyroelectric coefficient
$p_{ primary\ effect }$:	Primary pyroelectricity
$p_{ secondary\ effect }$:	Secondary pyroelectricity
q	:	Charge
S	:	Entropy
S	:	Strain
s_{jl}	:	Elastic compliance constant
T	:	Stress
T_c	:	Curie transition temperature
T_d	:	Depolarization temperature
T_m	:	Maximum temperature
T_0	:	Curie-Weiss temperature
t	:	Thickness
V	:	Applied voltage
V	:	Volume
v	:	Domain wall motion
X	:	Curie constant
Z	:	Impedance
β	:	Inverse dielectric constant
δ	:	Phase lag
ε'	:	Real permittivity
ε''	:	Imaginary permittivity

ϵ^*	:	Complex dielectric permittivity
ϵ_s	:	Instantaneous relative permittivity
ϵ_∞	:	Static dielectric permittivity
ϵ_{33}^S	:	Dielectric constant tensor under constant strain
ϵ_{33}^T	:	Dielectric constant tensor under constant stress
ϵ	:	Strain
$\Delta\epsilon$:	Dielectric strength
ΔP	:	Change in spontaneous polarization
ΔT	:	Change of temperature
dT/dt	:	Heating rate
τ	:	Relaxation time
μ	:	Dipole moment per unit volume
ϑ	:	Mobility of the domain wall
ω	:	Angular frequency
θ	:	Bragg diffraction angle in X-ray diffraction
λ	:	Wavelength
ρ	:	Density
σ^*	:	Complex conductivity
ϕ	:	Volume fractions
BNT	:	Sodium bismuth titanate
BaTiO ₂	:	Barium titanate
Bi ₂ Ti ₂ O ₇	:	Bismuth titanate
CeO ₂	:	Cerium Oxide
CH ₃ COONa	:	Anhydrous sodium acetate
(CH ₃ COO) ₃ Bi	:	Bismuth (III) acetate
DEC	:	Diethyl carbonate

DMF	:	Dimethylformamide
DMSO	:	Dimethyl sulfoxide
DRAM	:	Dynamic random access memory
DTA	:	Differential thermal analysis
EMT	:	Effective medium theory
FESEM	:	Field electron scanning electron microscopy
FeRAMs	:	Ferroelectric random access memories
FTIR	:	Fourier transform infrared
HRTEM	:	High-resolution transmission electron microscopy
KNbO ₃	:	Potassium niobate
La ₂ O ₃	:	Lanthanum oxide
MIM	:	Metal-insulator-metal structure
MPB	:	Morphotropic phase boundry
Nd ₂ O ₃	:	Neodymium oxide
PbO	:	Lead oxide
PMN-PT	:	Lead magnesium niobate
PT	:	Lead titanate
PVDF	:	Polyvinylidene fluoride
P(VDF-TrFE)	:	Polyvinylidene fluoride-trifluoroethylnene
PZT	:	Lead zicronate titanate
PbZrO ₃	:	Lead zicronate
RT	:	Room temperature
TE	:	Thickness extensional
TeFE	:	Tetrafluoroethylene
Ti[O(CH ₂)CH ₃] ₄	:	Titanium (IV) butoxide
TrFE	:	Trifluoroethylene
TG	:	Thermo gravimetric

XRD : X-ray diffraction

Y_2O_3 : Yttrium oxide

University of Malaya

CHAPTER 1: INTRODUCTION

1.1 Introduction

Ferroelectric ceramics such as lead titanate (PT) and lead zirconate titanate (PZT) are used widely in capacitor, actuator, sensor and transducer applications. These ceramics exhibit superior ferroelectric, pyroelectric and piezoelectric properties. However, these materials contain lead, which caused serious environmental pollution. The toxicity nature of lead alarms the world for elimination of its use in various devices. Thus, the search in novel lead free material for replacing the lead containing ceramics is in demand. Sodium bismuth titanate, $\text{Na}_{0.5}\text{Bi}_{0.5}\text{TiO}_3$ (BNT) is a perovskite ferroelectric discovered in 1960 by Smolenski et al. (Smolenskii et al., 1961). BNT exhibits high ferroelectric properties ($P_r = 38 \mu\text{C}/\text{cm}^2$) and Curie temperature ($T_c = 320^\circ\text{C}$). Synthesis of BNT using solid state reaction method as well as chemical route were reported previously (Smolenskii et al., 1961; Takenaka & Sakata, 1989; Hao et al., 2005; Xu et al., 2005). Synthesis method plays an important role in determination of the particle size which will affect the physical properties of the material. Preparation of BNT using sol-gel method will be able to produce a nanoparticle size of the BNT powder. The only setback of BNT is the polling effectiveness of the material is fair due to high leakage current. This can be solved by doping rare earth element such as cerium into the BNT ceramics.

In general, ferroelectric ceramics have poor mechanical strength and relatively high value of acoustic impedance, thus it is not so desirable for flexible electronic device applications. One of the promising solution to overcome this problem is to prepare a polymer/ceramic composite. For example, a ferroelectric ceramic (BNT) and a polymer ferroelectric such as poly(vinylidene fluoride)-trifluoroethylene

copolymer, P(VDF-TrFE). P(VDF-TrFE) is a ferroelectrics polymer which has high voltage sensitivity and good electromechanical properties.

The motivation of this study is to produce a novel ferroelectric which is highly flexible, with relatively high compliance and low density. In order to comply all the important characteristic that are interest in this research, the BNT ceramic is synthesized using sol-gel method with controlled particle size; doped with cerium to reduce the leakage current and the optimized BNT ceramic was incorporated in the polymer matrix to prepare a highly flexible novel functional polymer/ceramic nanocomposite film for the potential application such as thermal/infrared detector, energy storage and micro-electromechanical system.

1.2 Historical background

Ferroelectrics are widely used in various forms, including single crystal polycrystalline ceramics and polymer thin films. Most of the ferroelectric ceramics have perovskite-type structure such as barium titanate (BaTiO_3), lead titanate (PbTiO_3), lead zirconate titanate (PZT), potassium niobate (KNbO_3) and lead zirconate (PbZrO_3). In fact, the first ferroelectric ceramics, BaTiO_3 with perovskite structure was discovered in 1943-1947 with an anomalous dielectric, ferroelectric and piezoelectric properties (Xu, 1991). PZT was first reported by Jaffe et al. in 1954 (Jaffe et al., 1954) and became the main industrial product in piezoelectric field in the following ten years due to its extraordinary ferroelectric and piezoelectric properties. Due to the toxicity of lead in PZT, many researchers started researching on lead free ferroelectric ceramics. In 1961, Smolenskii et al. discovered sodium bismuth titanate (BNT), which is a lead-free piezoelectric ceramic. This compound has a similar perovskite structure as PZT and exhibited strong ferroelectric properties as well as high Curie temperature (Smolenskii et al., 1961).

Piezoelectricity in polymers such as poly(methy methacrylate) and poly(vinyl chloride) was first found in 1963 by Kocharyan (Kocharyan & Pachadzhyan, 1968). The following year, poly(vinylidene fluoride), PVDF was discovered by Kawai (Kawai, 1969) in the form of electret. PVDF was poled by applying high electric field either by orienting the permanent dipoles or creating space charge by injecting free chargers with an effective macroscopic separation of positive and negative charges. Soon afterward, Bergman in 1971 reported the finding of the pyroelectricity in the non-linear optical properties of PVDF (Bergman et al., 1971). Londo and Doll in 1968 suggested that by incorporating a small amount of trifluoroethylnene (TrFE) and tetraluoroethylnene (TeFE) into PVDF from the melt crystallization can induce a direct crystallization of polar β phase PVDF (Lando & Doll, 1968). Therefore, PVDF and its copolymers are widely investigated for the flexible systems and used in soft transducers and fast display applications (Furukawa, 1989).

In 1970's, piezoelectric composite composed of PZT powder as inclusion in PVDF matrix was developed (Xu, 1991). The embedded ferroelectric ceramic inclusions in a polymer matrix as a filler to form 0-3 type composites can enhance the functional properties of the polymer. The polymer/ceramic composite exhibit high dielectric permittivity, large spontaneous polarization and due to its high degree of flexibility compared to that of the inorganic ferroelectrics, it offers a promising potential for functional electronic application.

1.3 Objectives

Developing a wet mechanical method that is suitable for preparing nanostructured ceramic is one of the purposes in this study. The nano size ceramic particles affect the morphology and physical properties of the sample. These efforts were made to gain insight to the fundamental understanding of the structure and functional electrical properties of the BNT nanoceramics and its polymer nanocomposites. The dielectric, piezoelectric, pyroelectric and ferroelectric properties of the BNT nanoceramic and its polymer nanocomposite were thoroughly investigated. The specific objectives of this research are:

- To prepare BNT with homogenous nanograin using sol-gel method.
- To improve the piezoelectric properties, pyroelectric coefficients and the remnant polarization of BNT by doping with CeO_2 .
- To identify true values of k_{33} , d_{33} and c_{33} of the BNT ceramics using piezoresonance method.
- To investigate the effect of ferroelectric inclusion in P(VDF-TrFE) and enhance its piezo-, pyro- and ferroelectric properties.

1.4 Thesis structure

In chapter one, a brief introduction of ferroelectric materials and its potential application were given. This chapter also includes historical development of ferroelectric material. It is followed by the objectives of the research, where the understanding of structure and electrical properties of the BNT ceramic nanoparticles and its polymer nanocomposite becomes the main concern to improve the performance of the ferroelectric materials.

Chapter two of this thesis reviews the background of the materials including ferroelectric ceramic, polymer and composite. The mechanism involved in the

polarization of dielectric, piezoelectric, pyroelectric and ferroelectric materials are discussed as well. Chapter three discusses the methodology and theoretical aspects of the experiment. The synthesis of BNT using sol gel method, the fabrication of nanocomposite and the preparation of the samples for electrical measurements are discussed in depth. The principle and equipment setup for the electrical measurement used in this study were explained as well.

In chapter four, the physical functional properties (dielectric, piezoelectric, pyroelectric and ferroelectric) of the BNT nanoceramic synthesized using sol gel processing method are elaborated. The prepared BNT powder was sintered at four different sintering temperatures in order to study the relationship between structure and crystallinity of the sample. The piezoelectric, pyroelectric and ferroelectric properties are strongly influenced by the degree of crystallinity and homogeneity of the grain growth. Chapter five discusses the properties of the BNT nanoceramic by doping with various weight percentages of CeO_2 . The electro-mechanical properties of the pure and doped-BNT ceramics measured by using piezoelectric resonance method were discussed in chapter four and five, respectively.

Chapter six focuses on the PVDF-TrFE/ BNT composites. The associated theory, analysis of the experimental results and discussion were included in this chapter. Finally, chapter seven concludes the results of the overall study in this thesis and suggest a several possible research works that can be explored in the future.

CHAPTER 2: LITERATURE REVIEW

2.1 Introduction

This chapter presents the background of the ferroelectric materials such as BNT ceramics, P(VDF-TrFE) polymer and polymer/ceramic composites. The mechanisms involved in the polarization of dielectric, ferroelectric, pyroelectric and piezoelectric are discussed. The essential concept of ferroelectric phenomenon, which is related to the application of ferroelectricity is included. This chapter also discusses the unresolved issues and the motivation of the research.

2.2 Ferroelectric materials

Structural symmetry of a crystal depends on its lattice structure and it affects geometrically the structure and physical properties of the crystal such as dielectric, mechanical, piezoelectric, ferroelectric, nonlinear optical properties and etc. In the crystal, the lattice structure is described by Bravais unit cell. Even though there are more than thousands of crystals in nature, but there are only thirty-two macroscopic symmetry types of crystals (32 point groups) exists (see Table 2.1) (Xu, 1991). In a point group, the eight symmetry elements (excluding translation symmetry) consist of rotation axes such as: 1 (without rotation), 2 (rotation diad), 3 (rotation triad), 4 (rotation tetrad), 6 (rotation hexad), $\bar{4}$ (rotation-inversion tetrad axis), I (inversion center) and m (reflection mirror), respectively (Xu, 1991).

According to the Neumann's principle, symmetry elements of the physical properties in a crystal should include all symmetry elements of the 32 point groups of this crystal. Thus, if a crystal has physical parameter subjected to a symmetry operation, the value of this physical parameter should remain unchanged. Among the 32 point groups, 11 point groups are centrosymmetry with a symmetry center. A

symmetric center crystal does not have any polarity and possesses one or more crystallographically unique direction axis. Among these, 20 point groups (*) exhibit piezoelectricity, while 10 point groups (*+) have only one unique direction axis. A crystal with point-group symmetry has a unique rotation axis, but does not have any mirror perpendicular to this axis. Along a unique rotation axis, the atomic arrangement at one end is different from the other opposite end. These crystals are called polar crystals and exhibit spontaneous polarization.

A crystal with spontaneous polarization is regarded to be ferroelectric material when it has two or more orientation stages in the absence of an electric field, which can be switched from one state to the other. The identical crystal structure of two orientation states has differed only in electrical polarization vector when electric field is zero. However, not all piezoelectrics are pyroelectric, and not all pyroelectrics are ferroelectric, but all ferroelectric materials are dielectrics and exhibits pyroelectricity and piezoelectricity (Bernard Jaffe, 2012). The relationship between ferroelectric and piezoelectric is shown in Figure 2.1.

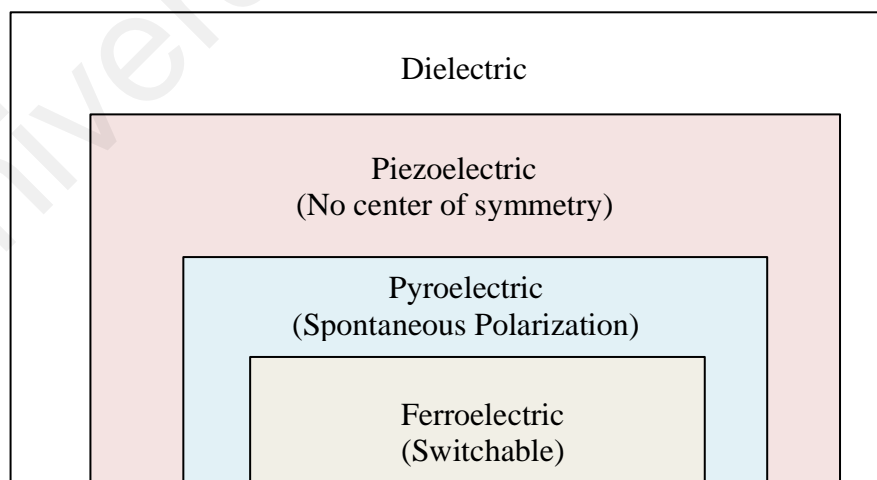


Figure 2.1: The relationship between ferroelectric, pyroelectric and piezoelectric.

Table 2.1: Symbol of the 32 point groups on crystallography. Remarks: (*) implies that piezoelectric effect may be exhibited and (+) implies that pyroelectric and ferroelectric effects may be exhibited (adapted from Xu, 1991).

Crystal system	International notation	Scönflies' notation	Remarks
Triclinic	1	C_1	*+
	$\bar{1}$	$C_1(S_2)$	-
Monoclinic	2	C_2	*+
	$m(\bar{2})$	$C_s(C_{1h})$	*+
	$2/m$	C_{2h}	-
Orthorhombic	2mm	C_{2v}	*+
	222	$D_2(V)$	*
	mmm	$D_{2h}(V_h)$	-
Tetragonal	4	C_4	*+
	$\bar{4}$	S_4	*
	4_2m	$D_{2d}(V_d)$	*
	422	D_4	*
	4mm	C_{4v}	*+
	4/m	C_{4h}	-
	4/mmm	D_{4h}	-
Trigonal (Rhombohedral)	3	C_3	*+
	$\bar{3}$	$C_{3i}(S_6)$	-
	3m	C_{3v}	*+
	32	D_3	*
	$\bar{3}m$	D_{3d}	-
Hexagonal	6	C_6	*+
	$\bar{6}$	C_{3h}	*
	6mm	C_{6v}	*+
	6/m	C_{6h}	-
	622	D_6	*
	$\bar{6}m2$	D_{6h}	*
	6/mmm	D_{6h}	-
Cubic	23	T	*
	$\bar{4}3m$	T_d	*
	m3	T_h	-
	43	O	-
	m3m	O_h	-

2.2.1 Crystal structure of BNT ceramics.

Sodium Bismuth Titanate, $\text{Na}_{0.5}\text{Bi}_{0.5}\text{TiO}_3$ (BNT) belongs to the perovskite family. This oxide ceramic has the general chemical formula ABO_3 , where O is the oxygen, A represents a cation with a large ionic radius and B is a cation with a smaller ionic radius. The cubic perovskite structure of BNT is shown in Figure 2.2(a). BNT crystallites exhibit cubic symmetry structure (point group $m\bar{3}m$) above

the Curie temperature, 320 °C (Smolenskii et al., 1961) with Na^+ and Bi^{3+} ions at the cube corners, O^{2-} ions at the face centers and Ti^{4+} ion at the body center. Below the Curie temperature, the structure is slightly deformed to rhombohedral and tetragonal (point group $4mm$) thereby creating dipoles (see Figure 2.2(b and c)). Each pair of positive and negative ions act as an electric dipole, and the spontaneous polarization (dipole per unit volume) refers to an assembly of these dipoles, pointing at the same direction when applying electric field (Xu, 1991).

BNT is an excellent candidate for lead-free piezoelectric ceramic. It has perovskite structure similar to that of the commercial lead ferroelectric material such as lead zirconate titanate, PZT ceramic. BNT exhibits strong ferroelectric properties with large remnant polarization, $P_r = 38 \mu\text{C}/\text{cm}^2$ at room temperature and high Curie temperature, $T_c = 320 \text{ }^\circ\text{C}$ (Smolenskii et al., 1961) comparable with PZT which has $P_r = 31 \mu\text{C}/\text{cm}^2$ and $T_c = 490 \text{ }^\circ\text{C}$ (Rukmini et al., 1998). BNT, however has a relatively high coercive field, $E_c = 73 \text{ kV/m}$ thus requires higher field for the poling process (Smolenskii et al., 1961). Conventional solid state reaction method is frequently used to synthesis BNT-based ceramics. However, this technique usually results in larger particle size and difficult to maintain a chemical homogeneity of the obtained powder since the reaction among the solid powders of the starting materials is heterogeneous (Kim et al., 2007). To date, many alternative methods have been developed to replace the conventional solid state method such as emulsion, pyrosol and sol gel method using either citrate and steric acid as a solvent, which produces nano scale particle size and improved chemical homogeneity, and consequently improve the electrical properties of the BNT ceramic (Cernea et al., 2010; Ghitulica et al., 2013; Hao et al., 2005; Kim et al., 2007; Smolenskii et al., 1961). Furthermore, modifying the compound by element substitution or doping such as rear earth oxide

materials such as La_2O_3 , CeO_2 , Y_2O_3 , and Nd_2O_3 onto BNT-based ceramic, effectively improve the piezoelectric properties of the ceramic (Xu, 1991).

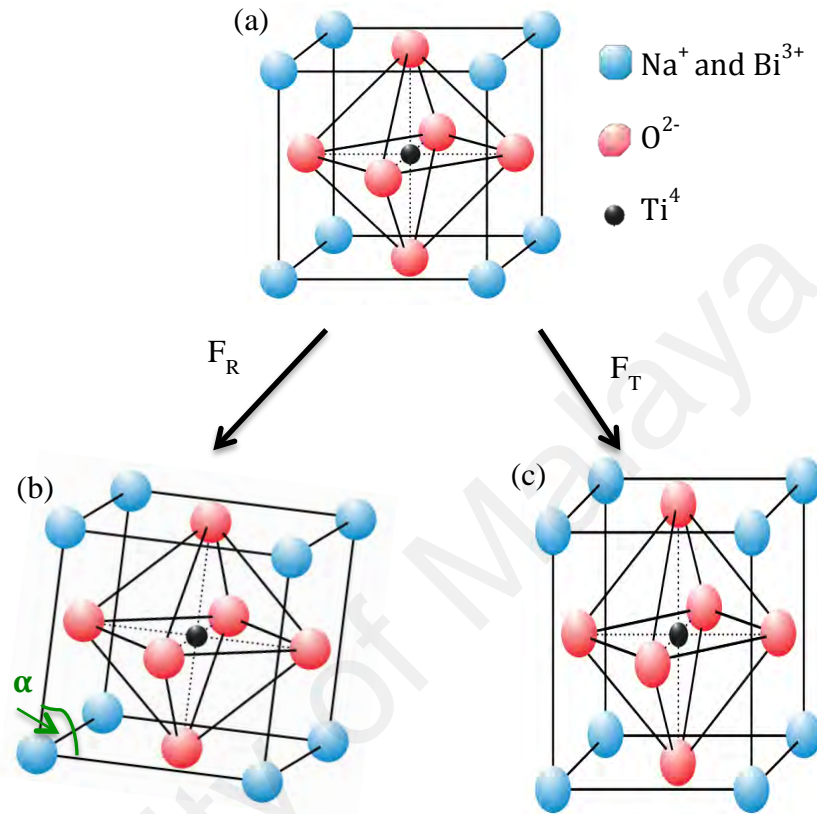


Figure 2.2: The crystal structure of BNT (perovskite-type structure); (a) cubic, (b) rhombohedral ferroelectric (F_R) and (c) tetragonal ferroelectric (F_T) structure.

2.2.2 Polyvinylidene fluoride-trifluoroethylene, P(VDF-TrFE) Polymer

Polyvinylidene fluoride (PVDF) was discovered by Kawai in 1969 (Kawai, 1969). It consists of a repeat unit of $(-\text{CH}_2\text{CF}_2-)$ monomer with positively charged H-atoms and negatively charged F-atoms which are aligned in one direction and perpendicular to the chain axis. The dipoles are rigidly attached to the main chain carbons and carries a vacuum dipole moment of $\mu_v = 7 \times 10^{-30}$ Cm (2.1 Debyes) (see Figure 2.3(a)). The dipoles orientation is subjected to the conformation and packing of molecules. If the molecule adopts an all-*trans* (TT) planar zigzag chain conformations (refer to Figure 2.3(b)) with a parallel packing and form β phase or

Form I (see Figure 2.3(c)). The bulk samples of PVDF, which is used widely in research and practical application are a mixture of both crystalline and noncrystalline regions. The sum of dipole moment, μ_v over a unit volume yields a large crystalline polarization, P_s .

$$P_s = \frac{2\mu_v}{abc} = 130 \text{ mC/m}^2 \quad (2.1)$$

where a , b and c are the lattice constants with $a = 0.858 \text{ nm}$, $b = 0.491 \text{ nm}$ and $c = 0.256 \text{ nm}$, respectively. The dipoles in the β phase conformation is switchable by applying electric field, thus β phase is responsible for the PVDF's ferroelectricity (Furukawa, 1989).

PVDF exhibits four crystalline polymorphs, known as Form I (β phase), II (α), III (γ) and IV (δ). Figure 2.4 shows the various crystalline polymorphs and crystal structures of PVDF (Furukawa, 1989; Lovinger, 1983; Scott, 2007). The β phase crystal has an all-trans (TT) planar zigzag chain conformation. Conventional β phase PVDF samples prepared by melt crystallization and cold drawing exhibit 50 % crystallinity. Special treatment like high-pressure crystallization and ultra-drawing could increase the crystallinity of the β phase and P_r to 100 mC/m^2 . The α phase consists of $\text{TGT}\bar{\text{G}}$ molecules packed in an antiparallel fashion (non polar crystalline). For γ phase, the molecules adopt an intermediate $\text{T}_3\text{GT}_3\bar{\text{G}}$ conformation, which form a polar crystalline due to its parallel packing. The δ phase is a parallel version of the α phase, which consists of $\text{TGT}\bar{\text{G}}$ molecular packing. The parallel and antiparallel molecular packing are related to the dipole orientation in the direction perpendicular to the chain axis. In $\text{TGT}\bar{\text{G}}$ and conformations, molecular dipoles are oriented not only perpendicular to the chain axis, but also along the chain axis. Among the four polymorphs, only the α phase is nonpolar, while the remaining three are polar

crystallines. From a vector sum of the constituent dipoles, the spontaneous polarization, P_s of the γ and δ is around one half of the β phase.

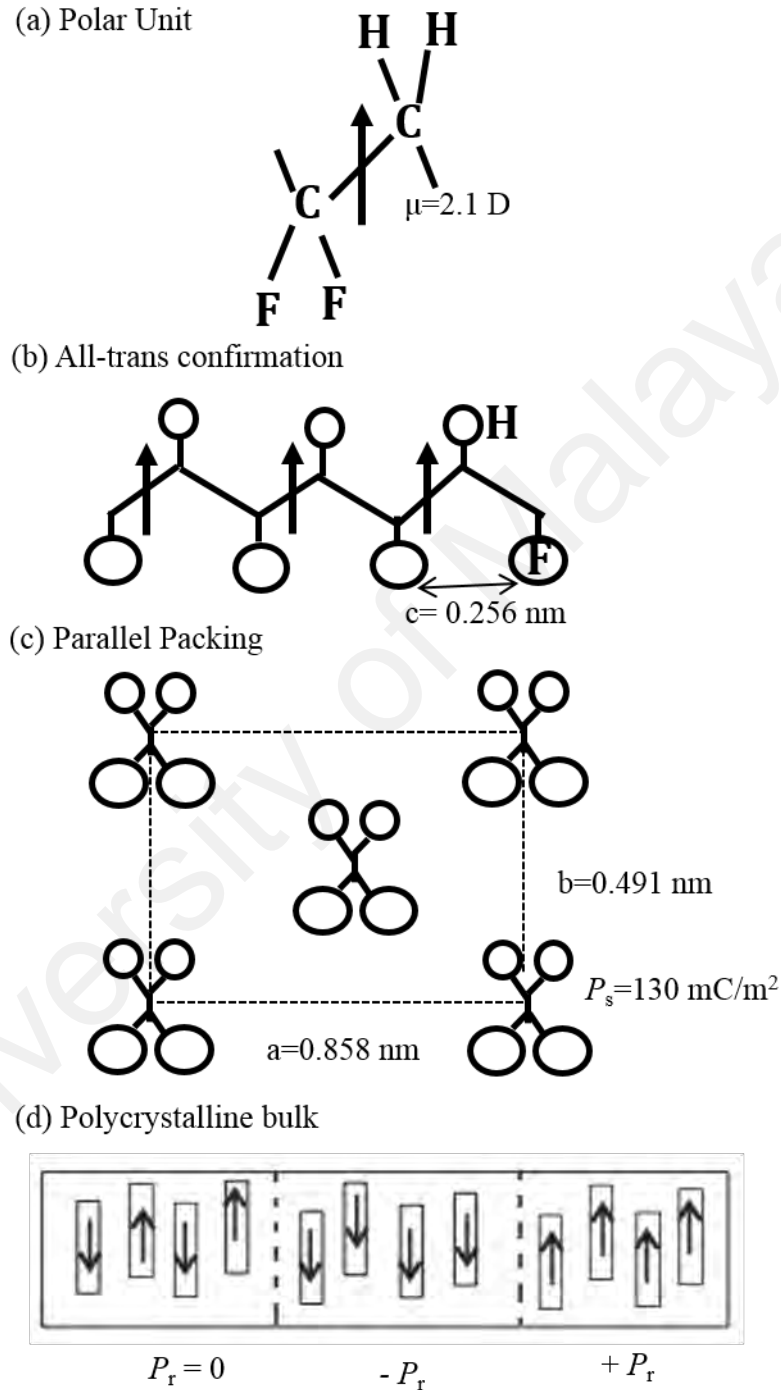


Figure 2.3: (a) unit, (b) molecule, (c) crystal and (d) bulk structures of PVDF (Furukawa, 1989).

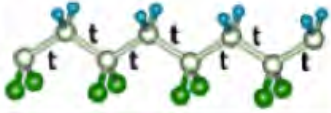
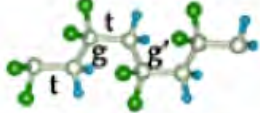
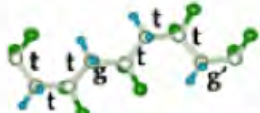
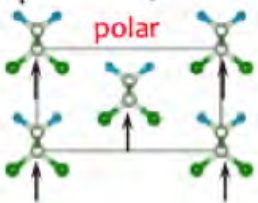
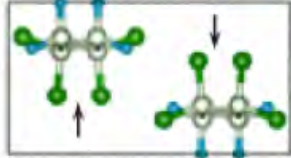
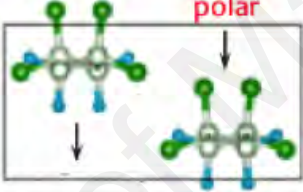
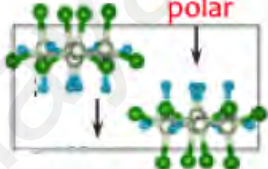
(a) TT	(b) TGT \bar{G}	(c) T ₃ GT ₃ \bar{G}
(i) Chain conformations		
		
(ii) Crystal structures		
	<p>α-PVDF nonpolar</p>  <p>δ-PVDF polar</p> 	

Figure 2.4: Chain conformations and crystal structure of PVDF; green, blue, white colour indicate the fluorine, hydrogen and carbon atom, respectively.

Figure 2.5 shows the phase transformation schemes of crystalline polymorph PVDF. The combination of thermal, mechanical and electrical treatments produce a specific crystalline polymorph of PVDF (Furukawa, 1989). Melt-crystallization produces the α phase film. Mechanical drawing, stretches the chain molecules and thus cause the conversion of α phase to β phase, where chain elongates from TGT \bar{G} conformation extend to all-trans conformation. Annealing of the α phase film at an appropriate temperature induces transformation to the γ phase. Annealing under high pressure causes conversion of the γ phase into the β phase due to close packing of the molecules. The transformation of the β phase into its polar, δ phase is obtained by applying high electric field. Further increase in applied electric fields will induce

additional conversion into the β phase via the γ phase (Das Gupta & Doughty, 1977; Davis et al., 1978).

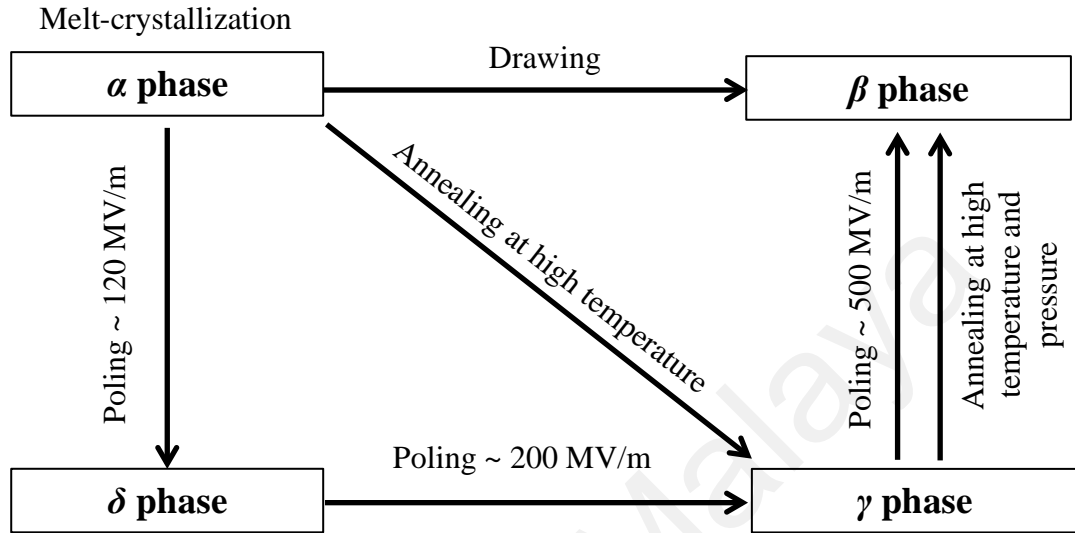


Figure 2.5: Schematic diagram of crystalline transformation among polymorphs of PVDF due to electrical, mechanical and thermal treatments

Londo and Doll in 1968 suggested that the introduction of a small amount of trifluoroethylene (TrFE) and tetrafluoroethylene (TeFE) into PVDF induce direct crystallization into the polar β phase from the melt crystallization (Lando & Doll, 1968). Similar to PVDF, P(VDF-TrFE) has been reported to crystallize into four types of crystalline phases which are β , α , γ and δ . However, P(VDF-TrFE) exhibits a much higher crystalline β phase compare to that of the pure PVDF and thus it has the tendency to crystallize in the polar β phase by heat treatment at a temperature between the Curie transition temperature (T_c) and the melting temperature (T_m) without the requirement of mechanical stretching (Furukawa, 1989; Weber et al., 2010). One should note that P(VDF-TrFE) exhibits a Curie point, while pure PVDF has none.

Choosing a suitable solvent and annealing temperature can prepare a specific crystalline phase. Samples prepared with a low evaporation rate and a high boiling

point solvents such as dimethylformamide (DMF), dimethyl sulfoxide (DMSO) and polar solvent of diethyl carbonate (DEC) are favorable to form the polar β phase PVDF. In this research, P(VDF-TrFE) is used as a polymer matrix to form a polymer nanocomposite with the BNT nanoparticle ceramic because it exhibits high voltage sensitivity and electromechanical properties and easily form the β phase conformation compared to the PVDF (Furukawa et al., 2006).

2.2.3 Ferroelectric Composites

The unique combination of ferroelectric ceramic and polymer promises an outstanding piezoelectric properties, low density and mechanical flexibility of the composite (Newnham et al., 1978). In general, ferroelectric ceramics exhibit high dielectric permittivity, large spontaneous polarization and high electromechanical coupling factor, but they are brittle and stiff, thus lacking the flexibility. In contrast, the ferroelectric polymers are highly flexible but with low density and weak piezoelectric properties. The desirable combination of both component (i.e. polymer and ceramic) with the right properties and coupling them in a right manner will maximize the characteristic advantages of each material in one component. Connectivity of the individual phases is important, because it controls the electric flux pattern and the mechanical properties of the combined materials (Newnham et al., 1978).

In a composite of 0-3 connectivity (see Figure 2.6), the ceramic inclusions are homogenously dispersed throughout the polymer matrix without being in contact with one another (Newnham et al., 1978). The 0-3 composite is one of the most studied material. Previous studies on polymer/ceramic composites such as lead titanate (PT), lead zirconate titanate (PZT), lead magnesium niobate (PMN-PT), barium titanate (BaTiO_3) and BNT embedded in the ferroelectric polymer matrix of

poly(vinylidene fluoride) (PVDF) and its copolymer P(VDF-TrFE) shows a great improvement in the ferroelectric properties of the polymer (Chan et al., 1998; Ploss et al., 1998; Furukawa et al., 1979; Ploss et al., 2001; Ploss et al., 2000b; Fang et al., 2009; Mahdi et al., 2015). It is possible to tailor a composite film to a specific application of interest by varying the constituent components and its volume fraction of ceramic filler (Ploss et al., 2000b). The filler aspect ratio, filler dispersion, filler alignment and orientation, polymer-polymer interaction, polymers and filler interaction, and the poling status are the key variables that determine the attributes of the ferroelectric nanocomposite. The extensive surface area of the filler may present benefits or limitations for such system.

The 0-3 connectivity composites are easy to produce by using a well-establish technique such as casting, hot pressing and spin coating. They exhibit low acoustic impedance, high piezoelectric voltage coefficient but lower electromechanical coupling factor and permittivity value, which are remarkable advantages for the composites being used as sensor elements (Hilczner et al., 2002). In this study, BNT synthesized by sol gel method will be doped with CeO_2 to improve its electrical properties. BNT with the optimized electrical properties will be selected as a ceramic inclusion to be embedded in P(VDF-TrFE) to form 0-3 connectivity ferroelectric composite. The functional electrical properties of the P(VDF-TrFE) matrix embedded with CeO_2 doped BNT nanoparticles will be thoroughly investigated.

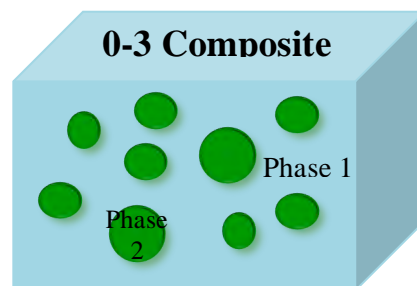


Figure 2.6: Representative unit of a two-phase system composed of a polymer matrix (phase 1) and ceramic inclusion (phase 2).

2.3 Dielectric Properties

In general, there are two types of dielectrics, namely polar and non-polar. The polar dielectrics have permanent dipole moments, but the non-polar dielectrics do not possess any permanent dipole moment. Polarization in dielectric (non-conductive materials) arises from the electronic, ionic (atomic) and dipolar (orientation) polarization (Schönhals & Kremer, 2003). The polarization phenomenon occurs when an external electric field is applied on a dielectric material. Perturbation is created by dynamically changing the position of the nuclei and electrons and constantly the dipoles are aligned under the influence of an applied electric field. Figure 2.7 shows a various polarization mechanism that can occur depending on the frequency of the applied electric field. An electronic polarization is induced from a slight displacement of the electron cloud of any atom in the dielectrics, relative to its positive nucleus by the electric field. This type of polarization occurs within the frequency range of 10^{15} Hz (see Figure 2.7(a)). Ionic or atomic polarization occurs only in ionic materials. An electric field acts to displace the cations in one direction and anions in the opposite direction, which consequently increase the net dipole moment (see Figure 2.7(b)). The electronic and ionic polarizations occur in the optical frequency ($\sim 10^{13}$ Hz) and govern the high frequency dielectric properties that produce low value of dielectric constant. The orientation polarization is exhibited only in the materials that possess permanent dipole moments. The polarization induced from a rotation of the permanent dipoles into the direction of the applied field, is represented in Figure 2.7(c) (Dahiya & Valle, 2013). The orientation polarization results in dielectric relaxation phenomenon that associates to the molecular motion of the material.

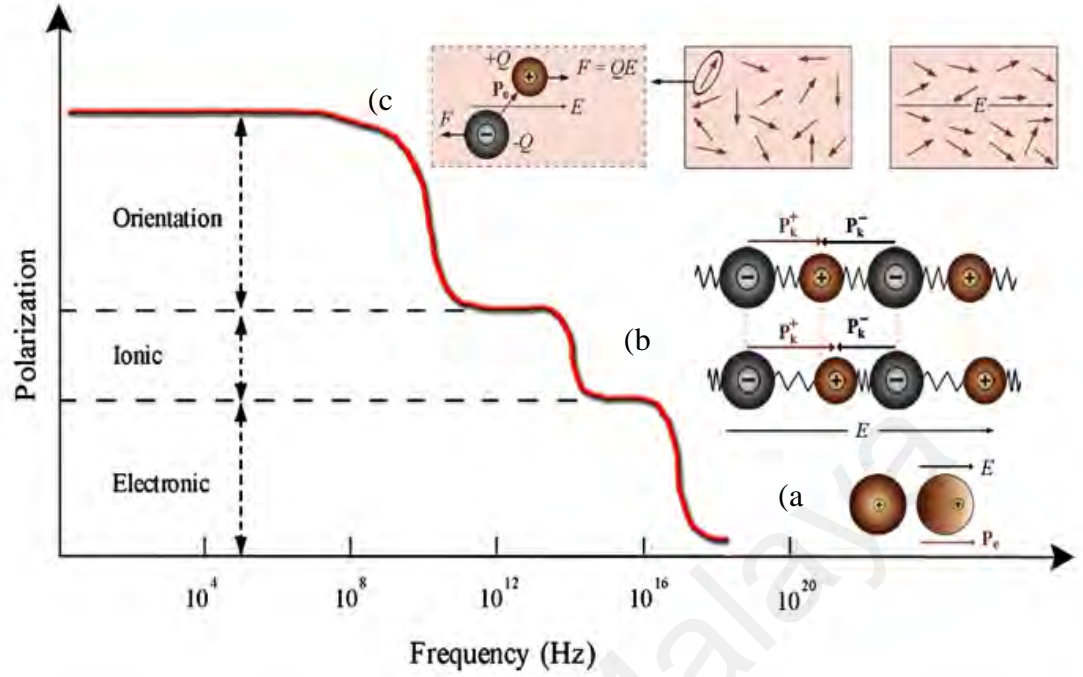


Figure 2.7: Frequency dependence of various polarization mechanisms: (a) The electronic, (b) ionic and (c) orientation polarization mechanisms (Dahiya & Valle, 2013).

Another source of polarization is known as interfacial polarization. It exists due to the space charges that are trapped in electrodes and at heterogeneous structure of grain boundaries. The total electric polarization of a dielectric substance is equal to the sum of electronic, atomic, orientation and interfacial (if there are some influence of impurities in the system) polarizations. The average polarization, \mathbf{P} is produced by N amounts of electric dipole moments, \mathbf{p} which are all aligned per unit volume, V . \mathbf{P} can be describe by the following equation (Schönhals & Kremer, 2003):

$$\mathbf{P} = \frac{1}{V} \sum_{i=0}^N \mathbf{p}_i \quad (2.2)$$

where i is the number of dipole moments in the system. Molecules or particles exhibit dipole moment if the electric centers of gravity of positive and negative charges do not match. For example for a system with a positive charge $+q$ and

negative charge $-q$ being separated by distance \mathbf{r} with the dipole moment of $\mathbf{p} = q\mathbf{r}$.

For any distribution of density charges $\rho_e(\mathbf{r})$, the dipole moment can be express by:

$$\mathbf{p} = \int_V \mathbf{r} \rho_e(\mathbf{r}) d^3\mathbf{r} \quad (2.3)$$

In dielectric materials, the dielectric constant and dielectric loss are important practical parameters. Investigating the dielectric properties of a given material provide a great deal of information in understanding the mechanism of electric polarization and the relaxation phenomenon of the system. The dielectric constant and dielectric loss of substances vary with frequency. A relaxation phenomenon is related to the orientation polarization or molecular fluctuation of dipoles due to the molecules, while resonance effect is due to electronic or atomic polarization. When an external electric field is applied on the substance, relaxation is occurred when there is a lag in attaining of equilibrium state. The dielectric relaxation phenomenon exponentially decayed with polarization with time when the applied electric field is removed.

Orientation polarization of molecular dipoles is a slower process which occurs at the lower frequency range compared to the electronic and atomic polarization. In order to obtain equilibrium maximum orientation polarization, a sufficient time is required to allow the applied electric field to be realized in the material. If enough time is provided during the measurement (at low frequency), the relative permittivity known as static dielectric permittivity, ϵ_s can be observed. In contrast, if the polarization is measured right after the field is applied, then a low magnitude of instantaneous relative permittivity, ϵ_∞ will be produced.

The polarization phenomenon can be observed by considering the applied alternating electric field, E with an amplitude, E_0 , angular frequency, ω and time, t across a dielectric material. The applied electric field, E given as:

$$E = E_0 \cos \omega t \quad (2.4)$$

The orientation of any dipoles will be lagged behind the applied field. The phase lag in the electric displacement, D can be defined as:

$$D = D_0 \cos (\omega t - \delta) \quad (2.5)$$

where δ is the phase lag. The electric displacement can be rewritten as:

$$D = D_1 \cos \omega t - D_2 \sin \omega t \quad (2.6)$$

where $D_1 = D_0 \cos \delta$ and $D_2 = D_0 \sin \delta$

Thus, the real permittivity, ϵ' and imaginary permittivity, ϵ'' can be obtained as:

$$\epsilon' = \frac{D_1}{\epsilon_0 E_0} \quad \text{and} \quad \epsilon'' = \frac{D_2}{\epsilon_0 E_0} \quad (2.7)$$

The tangent loss is:

$$\tan \delta = \frac{\epsilon''}{\epsilon'} \sim \frac{\text{energy dissipated per cycle}}{\text{energy per cycle}} \quad (2.8)$$

The complex relative permittivity is:

$$\epsilon^* = \epsilon' - i\epsilon'' \quad (2.9)$$

With an applied alternating voltage is given by the real part of $V(V = V_0 e^{i\omega t})$, the current, I that flows in the circuit is evaluated from the complex relative permittivity:

$$I = \epsilon^* C_0 \frac{dV}{dt} = i\omega \epsilon^* C_0 V = \omega C_0 (\epsilon'' + i\epsilon') V \quad (2.10)$$

a capacitive component of the current leads the voltage by 90 ° is given by:

$$I_c = i\omega C_0 \varepsilon' V \quad (2.11)$$

where a resistive component is in phase with the voltage:

$$I_R = \omega C_0 \varepsilon'' V \quad (2.12)$$

The relaxation time, τ is defined as time required for the polarization to reduce to 1/e times to its original value. It is a measure of the time where the dipoles become oriented in with the electric field. The relaxation time, τ is given by:

$$f(\tau) = \frac{1}{e} \quad (2.13)$$

where e is the base of natural logarithm. For the maximum loss factor, the angular frequency, ω_m is written as:

$$\omega_m = \frac{1}{\tau} \quad (2.14)$$

When an electric field is applied to the liquid or solid materials that are in a condensed molecular state, there is some limitation in the freedom of the motion. Constant collisions of molecules cause internal friction, thus the molecules turn slowly and exponentially approach the final state of the orientation polarization with a relaxation time constant. When the field reaches zero, the sequence is reversed and random distribution is restored at the same time constant. The critical frequency, f_m can be expressed in terms of angular frequency, ω_m as:

$$f_m = \frac{\omega_m}{2\pi} = \frac{1}{2\pi\tau} \quad (2.15)$$

2.3.1 Analysis of dielectric spectra

The complex dielectric permittivity, ϵ^* is dependence on the frequency and temperature. It originates from different processes such as microscopic fluctuations of molecular dipoles (rotational diffusion), the propagation of mobile charge carriers (translational diffusion of electrons, holes or ions), and the separation of charges at interfaces, which gives rise to additional polarizations.

Relaxation processes are due to rotational fluctuations of molecular dipoles and characterized by a peak in the imaginary part, ϵ'' and a step-like decrease of the real part, ϵ' of the complex dielectric permittivity, ϵ^* (Equation 2.9) with increasing frequency (see Figure 2.8). In contrast, conduction phenomenon can be observed when the imaginary part of the dielectric function increases with decreasing frequency. The real part of a complex dielectric function for pure ohmic conduction is independent of frequency. The real part increases with decreasing frequency for non-ohmic conduction or polarization effect (at inner boundaries or external electrodes) (Schönhals & Kremer, 2003). This is due to the phase lag between the dipole alignment and the electric field.

The alternating electric field is slow enough at low frequency, so that the dipoles are able to move smoothly with the field vibrations. The dielectric loss, ϵ'' is directly proportional to the frequency if the polarization is fully developed. As the frequency increases, dielectric loss, ϵ'' keep increasing but the storage of real part of dielectric constant, ϵ' begins to decrease. This is due to the phase lag between the dipole alignment and the electric field. At high frequency which is above the relaxation frequency, the ϵ' and ϵ'' decrease as the electric field is too fast to influence the dipole rotation and eventually the orientation polarization disappears.

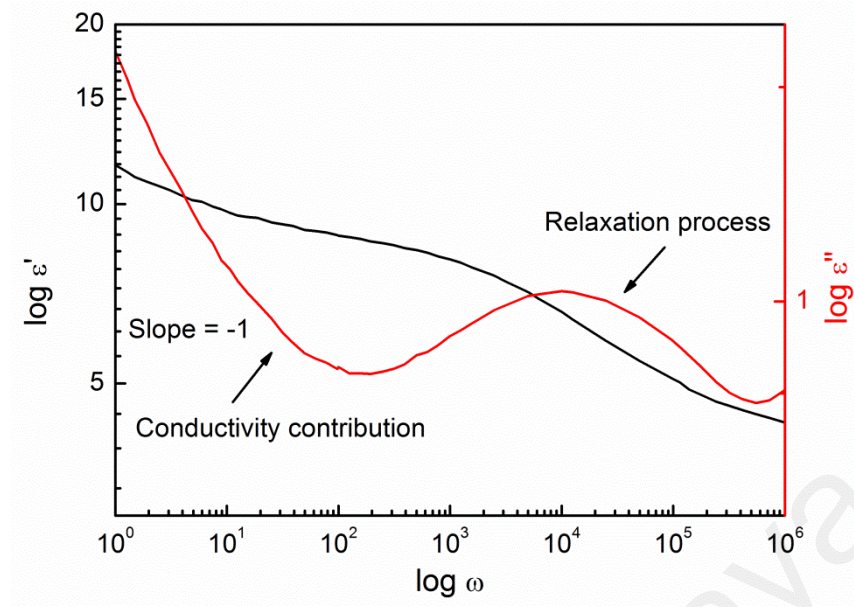


Figure 2.8: The real, ϵ' (black line) and imaginary, ϵ'' (red line) part of the complex dielectric function for a relaxation process (Gan, 2015).

Dielectric relaxation processes are usually analyzed using several models. Debye function serves as an essential theoretical function where both the frequency and the time domain have been suggested to describe the experimentally observed spectra. The Debye function for the frequency dependence of ϵ^* is written as:

$$\epsilon^* = \epsilon_\infty + \frac{\Delta\epsilon}{1+i\omega\tau_D} \quad (2.16)$$

where $\Delta\epsilon = \epsilon_s - \epsilon_\infty$ is the dielectric relaxation strength, where ϵ_s is the static dielectric permittivity, ϵ_∞ is the infinite relative dielectric and τ_D is the Debye relaxation time where the maximal loss occurs. In most cases, the relaxation peaks are asymmetric with high frequency tail where its half width of measured loss peaks is much broader as predicted by the Debye function and it is called as a non-Debye (non-ideal) relaxation behavior. As a result, the broadening of the dielectric function can be described by the Cole-Cole function (Schönhals & Kremer, 2003):

$$\varepsilon^* = \varepsilon_\infty + \frac{\Delta\varepsilon}{1+(i\omega\tau_{cc})^\alpha} \quad (2.17)$$

where α describes the symmetrical broadening of the relaxation peaks. In the Debye function, $\alpha = 1$ while in the Cole-Cole function α is $0 < \alpha \leq 1$. The Cole-Cole relaxation time, τ_{cc} denotes the position of a maximal loss by $\omega = 1/\tau_{cc}$.

The complex dielectric function can have an asymmetric broadening peak and can be described by the Cole-Davidson function as (Schönhals & Kremer, 2003):

$$\varepsilon^* = \varepsilon_\infty + \frac{\Delta\varepsilon}{(1+i\omega\tau_{CD})^\beta} \quad (2.18)$$

The parameter β ($0 < \beta \leq 1$) describes an asymmetric broadening of the relaxation function. When $\beta = 1$, the Debye-function is recovered again. It should be noted that the characteristic relaxation time of this asymmetric model function like the Cole-Davidson function does not coincide with the relaxation time which is related to the position of maximal loss. The relationship of both quantities depends on the shape parameter.

A more general function was then introduced by Havriliak and Negami (HN-function) by including both combination of the Cole-Cole and the Cole-Davidson function (Schönhals & Kremer, 2003):

$$\varepsilon^* = \varepsilon_\infty + \frac{\Delta\varepsilon}{(1+(i\omega\tau_{CD})^\alpha)^\beta} \quad (2.19)$$

The symmetric and asymmetric broadening of the complex dielectric function can be described by the fractional shape parameters, α and β in which $0 < \alpha, \alpha\beta \leq 1$. The parameters α and β are related to the limiting behavior of the complex dielectric function at low and high frequencies. By analyzing the frequency and temperature

dependence of the complex permittivity; the dielectric strength, phase transition, transition temperature and frequency relaxation involved in the system can be identified. The HN-function will be applied to fit the complex permittivity for a complete description of the isolated regions that involved in the system.

2.4 Piezoelectric properties

The piezoelectric effect is a linear electromechanical interaction which crystalline materials with no inversion symmetry. The relationship between electric and elastic phenomenon is shown schematically in Figure 2.9. The piezoelectric material becomes electrically polarized when an external stress or force applied on it. This phenomenon is referred to the direct piezoelectric effect. If the material becomes strained when placed in an electric field is called the converse piezoelectric effect. The microscopic origin of the piezoelectric effect is the displacement of ionic charges within a crystal structure. In the absence of external strain or force, the charge distribution within the crystal is symmetric and thus, the net electric dipole moment is zero (see Figure 2.10(a)). However, when an external stress or force is applied, the charges are displaced and the charge distribution becomes asymmetric. The internal reticular can be deformed causing the separation of the positive and negative charges in the molecule generating dipoles and causing internal electric field (refer to Figure 2.10(b)). The opposite facing poles inside the material cancel each other and fixed charges appear on the surface (see Figure 2.10(c)). This polarization generates an electric field that can be used to transform the mechanical energy into the electrical energy (Dahiya & Valle, 2013; Jordan & Ounaies, 2001).

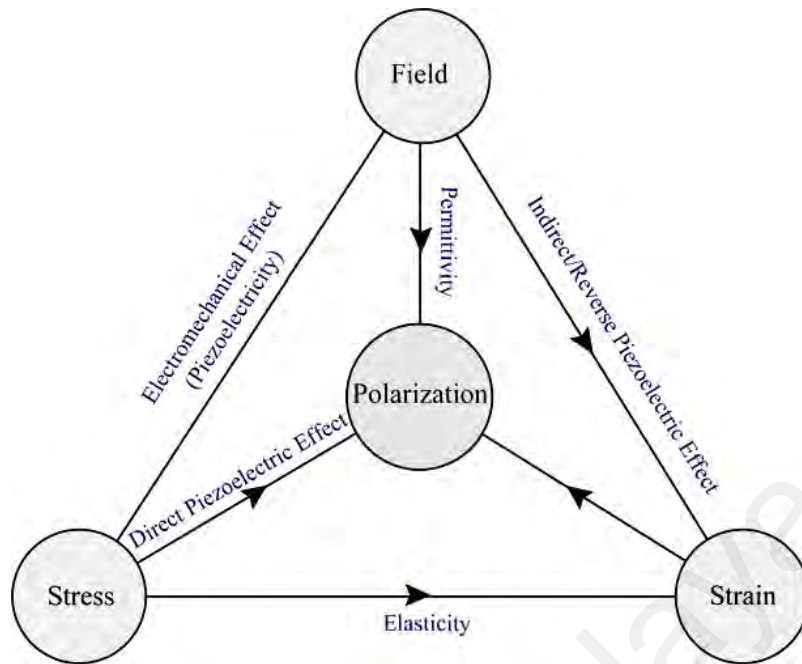


Figure 2.9: Piezoelectricity; the relationship of electric and elastic phenomena (Dahiya & Valle, 2013).

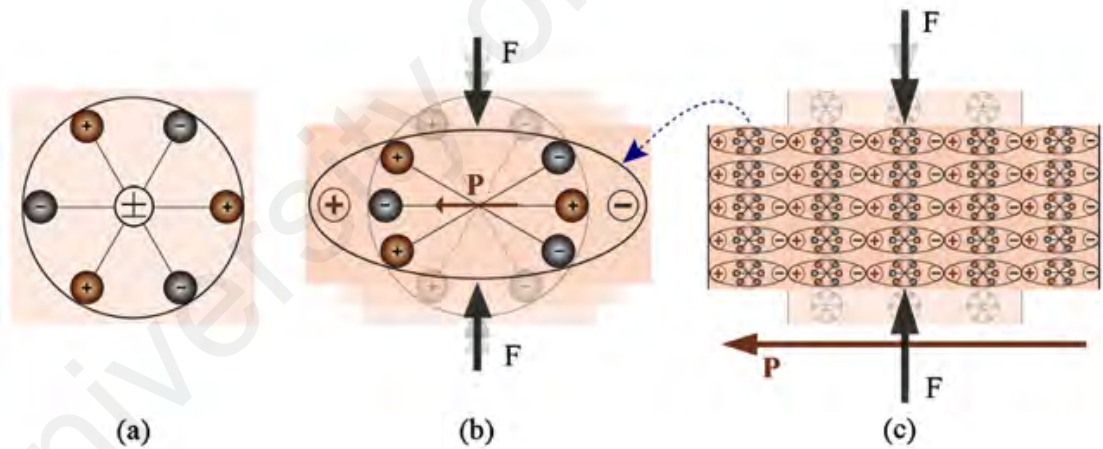


Figure 2.10: Piezoelectric effect with a simple molecular model: (a) An unperturbed molecule with no piezoelectric polarization; (b) An external force F , applied to the molecule resulting in to polarization P ; (c) The polarizing effect on the surface when piezoelectric material is subjected to an external force (Dahiya & Valle, 2013).

2.4.1 Piezoelectric equations

On the basis of the thermodynamic principles of the piezoelectric effect, piezoelectric constant can be derived from the Gibbs free energy as demonstrated in Figure 2.11 (Tichý et al., 2010). These equations describe the linear relationships between mechanical quantities; stress, T or strain, S and electric quantities; electric field, E or electric displacement, D of piezoelectric effect. The electromechanical equations using the combinations of these variables are shown as below (Furukawa & Fukada, 1976; Tichý et al., 2010):

$$D_i = \varepsilon_{ik}^T E_k + d_{il} T_l \quad (2.20)$$

$$S_j = d_{jk} E_k + s_{jl}^E T_l \quad (2.21)$$

$$E_i = \beta_{ik}^T D_k + g_{il} T_l \quad (2.22)$$

$$S_j = g_{jk} D_k + s_{jl}^D T_l \quad (2.23)$$

$$D_i = \varepsilon_{ik}^S E_k + e_{il} S_l \quad (2.24)$$

$$T_j = -e_{jk} E_k + c_{jl}^E S_l \quad (2.25)$$

$$E_i = \beta_{ik}^S D_k + h_{il} S_l \quad (2.26)$$

$$T_j = -h_{jk} D_k + c_{jl}^D S_l \quad (2.27)$$

where $i, k = 1, 2, 3$ and $j, l = 1, 2, \dots, 6$, adopted whereby repetition of suffix implies summation with respect to that suffix. The symbol ε_{ik} is the dielectric constant, β_{ik} is the inverse dielectric constant, s_{jl} is the elastic compliance constant and c_{jl} is the stiffness compliance constant. Superscripts S and T denote the clamped and free mechanical boundary conditions, respectively, while D and E denote the short-

circuited and open-circuited electrical boundary conditions, respectively (Furukawa & Fukada, 1976). Equations 2.20, 2.22, 2.24 and 2.26 describe the direct piezoelectric effect while the rest of the equations describe the converse effect. The arrows in the Figure 2.11 represent relations between variables. Arrow always begins at the independent variable and ends at the dependent. Arrows pointing from mechanical to electrical quantity represent direct piezoelectric effect. While, arrows pointing from electrical to mechanical quantity belong to the converse piezoelectric effect (Tichý et al., 2010).

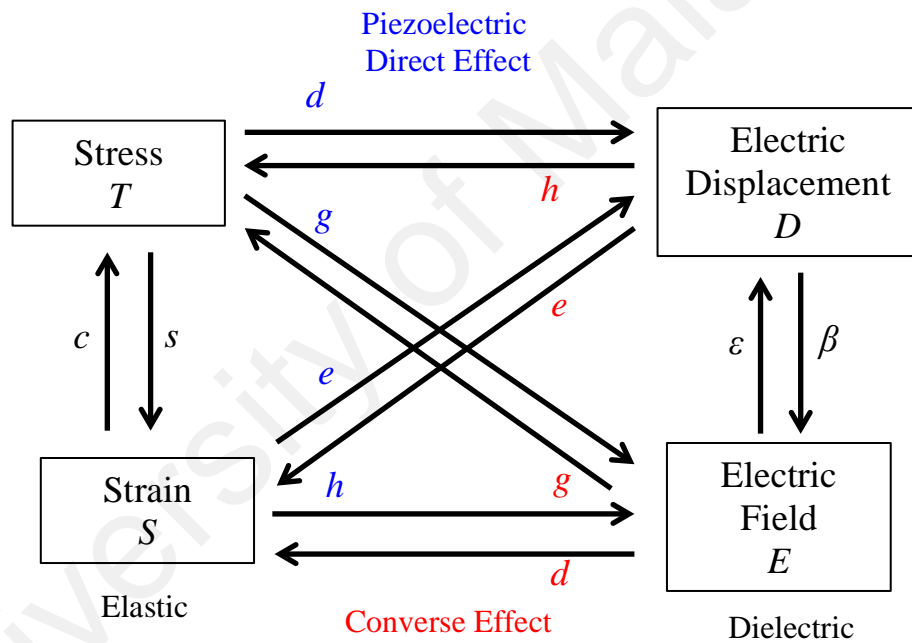


Figure 2.11: Linear electromechanical equations.

The piezoelectric constants of d_{ij} , e_{ij} , g_{ij} and h_{ij} defined as (Furukawa & Fukada, 1976; Bernard Jaffe, 2012; Tichý et al., 2010):

$$\begin{array}{cc} \text{Direct} & \text{Converse} \\ d_{ij} = \left(\frac{\partial D_i}{\partial T_j} \right)_E & = \left(\frac{\partial S_j}{\partial E_i} \right)_T \end{array} \quad (2.28)$$

$$e_{ij} = \left(\frac{\partial D_i}{\partial S_j} \right)_E = - \left(\frac{\partial T_j}{\partial E_i} \right)_S \quad (2.29)$$

$$g_{ij} = - \left(\frac{\partial E_i}{\partial T_j} \right)_D = \left(\frac{\partial S_j}{\partial D_i} \right)_T \quad (2.30)$$

$$h_{ij} = - \left(\frac{\partial E_i}{\partial S_j} \right)_D = - \left(\frac{\partial T_j}{\partial D_i} \right)_S \quad (2.31)$$

The first term expresses the direct piezoelectric effect, and the second term is the inverse piezoelectric effect. These constants are related by:

$$\frac{d_{ij}}{e_{il}} = S_{jl}^E \quad (2.32)$$

$$\frac{d_{ij}}{g_{kj}} = \varepsilon_{ik}^T \quad (2.33)$$

$$\frac{g_{ij}}{h_{il}} = S_{jl}^D \quad (2.34)$$

$$\frac{e_{ij}}{h_{kj}} = \varepsilon_{ik}^S \quad (2.35)$$

The piezoelectric effect is alternatively expressed by the electromechanical coupling coefficient:

$$k_{ij}^2 = \frac{d_{ij}^2}{\varepsilon_{ij}^T S_{ij}^E} \quad (2.36)$$

The dependences of s and ε on the boundary conditions are described by the electromechanical coupling coefficient, k :

$$\frac{s^E}{s^D} = \frac{\varepsilon^S}{\varepsilon^T} = 1 - k^2 \quad (2.37)$$

Piezoelectric measurement is done either by a direct method or a resonance method. The former determines the piezoelectric constants via Equation 2.28 to Equation 2.31 and the latter determines the electromechanical coupling coefficient. The piezoelectric resonance measured in terms of dielectric measurement. Analyses of the spectra give the piezoelectric constants and electromechanical coupling coefficient. In this study, broadband dielectric spectra will be used to observe the piezoelectric resonance of the poled ceramic samples. The equations above were fitted with the experimental result in order to measure the true values of piezoelectric constants and electromechanical coupling coefficient.

2.5 Ferroelectric properties

From a physical point of view, ferroelectric crystals possess one or more ferroelectric phases. The ferroelectric phase is a state that exhibits spontaneous polarization, \mathbf{P}_s in a certain temperature range and the direction of the spontaneous polarization can be reoriented by an external electric field. Spontaneous polarization is defined as the value of the dipole moment per unit volume, or the value of the charge per unit area on the surface perpendicular to the axis of the spontaneous polarization. Since the electrical properties are strongly correlated with the crystal structure, the axis of spontaneous polarization is always the crystal axis. A spontaneous polarization can be described as:

$$\mathbf{P}_s = (\iiint \mu \, dV) / \text{volume} \quad (2.38)$$

where μ is the dipole moment per unit volume, V . Although a polar axis crystal might exhibit piezoelectric effect, but not all piezoelectric crystals necessarily have a spontaneous polarization vector. This is due to the sum of electric moments along the polar axes may be equal to zero. Only a crystal with a unique polar axis exhibits a spontaneous polarization vector, \mathbf{P}_s along this axis.

2.5.1 Ferroelectric domains

In general, uniform alignment of electric dipoles only occurs in some regions of a crystal, whereas in some regions the spontaneous polarization may be in the reverse direction. The uniform polarization regions are called as ferroelectric domains. The interface between the two domains is known as domain wall. The orientation of the dipoles usually coincides with the direction of the spontaneous polarization. The ferroelectric domain structure depends on the structure of the ferroelectric crystal. A ferroelectric crystal has a polydomain structure and it acts as a single domain when enough high external electric field strength is applied on it. A strong field may reverse the spontaneous polarization of domain and this phenomenon is known as ‘domain switching’. When an electric field, \mathbf{E} is applied, the velocity of the domain wall motion \mathbf{v} can be written as:

$$\mathbf{v} = \vartheta \mathbf{E} \quad (2.39)$$

where ϑ is the mobility of the domain wall. The motion of the domain wall is contributed from the stress distribution, space charges and defects in the crystal (Xu, 1991).

2.5.2 Ferroelectric hysteresis loops

The important characteristic of ferroelectrics is the P - E hysteresis loop, where the polarization, P is a double-valued function of the applied electric field, E . At large signals, both the electric displacement, D and the polarization, P are nonlinear functions of the electric field, E given as the linear equation below:

$$\mathbf{D} = \mathbf{P} + \epsilon_0 \mathbf{E} \quad (2.40)$$

where ϵ_0 is the permittivity of free space (8.85×10^{-12} C/Vm). For most ferroelectric materials, the second term in the above equation is negligible, and a D - E and P - E loop become interchangeable.

If a small amount of electric field is applied on the ferroelectric sample, it will exhibit only linear relationship of P and E . This is because the applied field is not enough to switch any domain or dipoles, and the ferroelectric crystal will behave as a normal dielectric material (paraelectric). This corresponds to the segment OA of the curves in Figure 2.12. When the electric field strength increases, the negative domains (which have a polarization opposite to the direction of the applied electric field) will be switched to the positive direction (along the field direction). If the electric field is increased, the polarization will increase rapidly (segment AB) until all the domains are aligned in the positive direction (segment BC). This state is the saturation state in which the crystal is composed of just a single domain.

As the electric field strength decrease and reduce to zero, the polarization will generally decrease (at the point D), but does not return back to zero, because some of the domains will remain aligned in the positive direction and the crystal will exhibit a remanent polarization, P_r . The extrapolation of the linear line from segment BC back to the polarization axis (zero electric field at the point E) represents the value of the spontaneous polarization, P_s .

The remanent polarization, P_r in a crystal remains unless an opposite (negative sign) direction of electric field is applied (point F). The strength of the electric field required to reduce the polarization to zero is called the 'coercive field', E_c . Further increase of the electric field in the negative direction will cause a complete alignment of the dipoles in the opposite direction. Thus, the cycle of the hysteresis loop can be completed by reversing the electric field direction once again (see Figure 2.12) (Xu, 1991).

In addition to the P - E hysteresis loop, polarization switching leads to strain-electric field hysteresis. The typical strain-field loop resembles a butterfly shape and it is often referred to as the “butterfly loop” (see Figure 2.13). As the electric field is applied to the ferroelectric crystal, the converse piezoelectric effect dictates the strain results. When the electric field increases, the strain is no longer linear with the field as the domain walls start switching (Jordan & Ounaies, 2001). When the electric field is removed, the crystal experiences permanent strain or permanent change in the dimensions. In this research, only P - E hysteresis loop will be used to analyze the remanent polarization, P_r and coercive field, E_c of BNT ceramic and its composite.

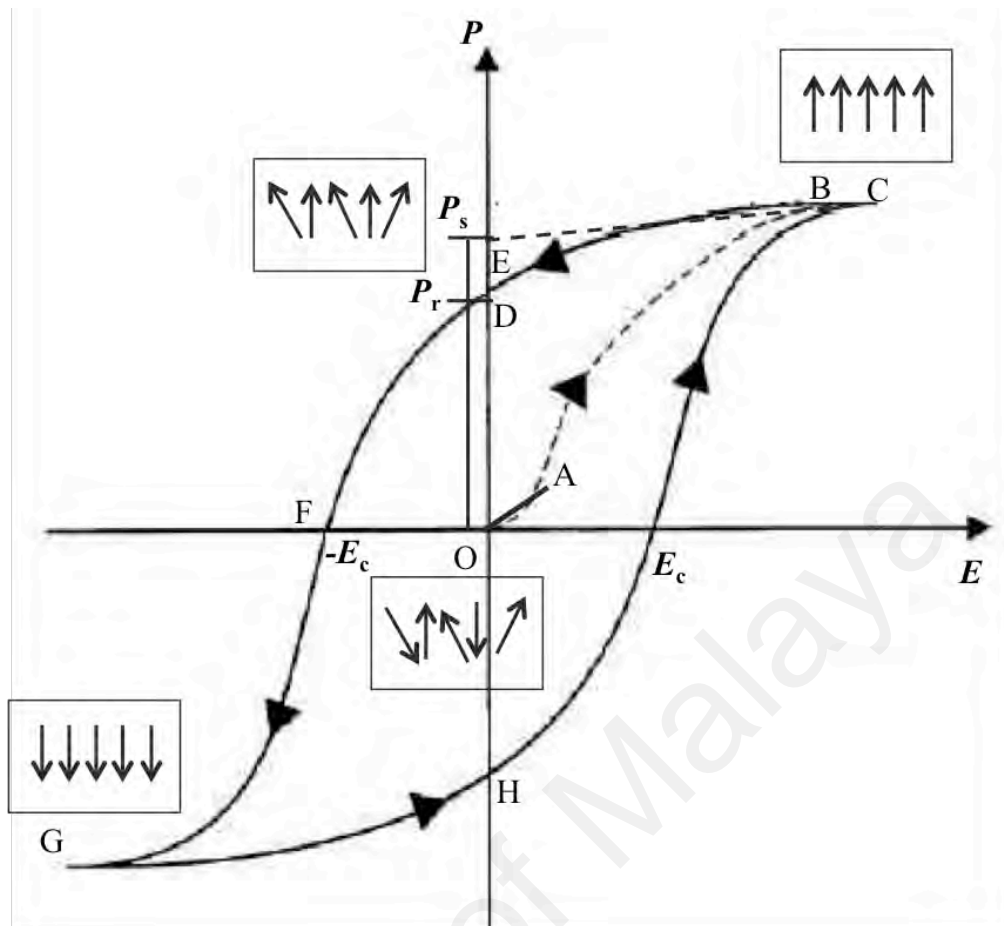


Figure 2.12: A typical P - E hysteresis loop in ferroelectric materials.

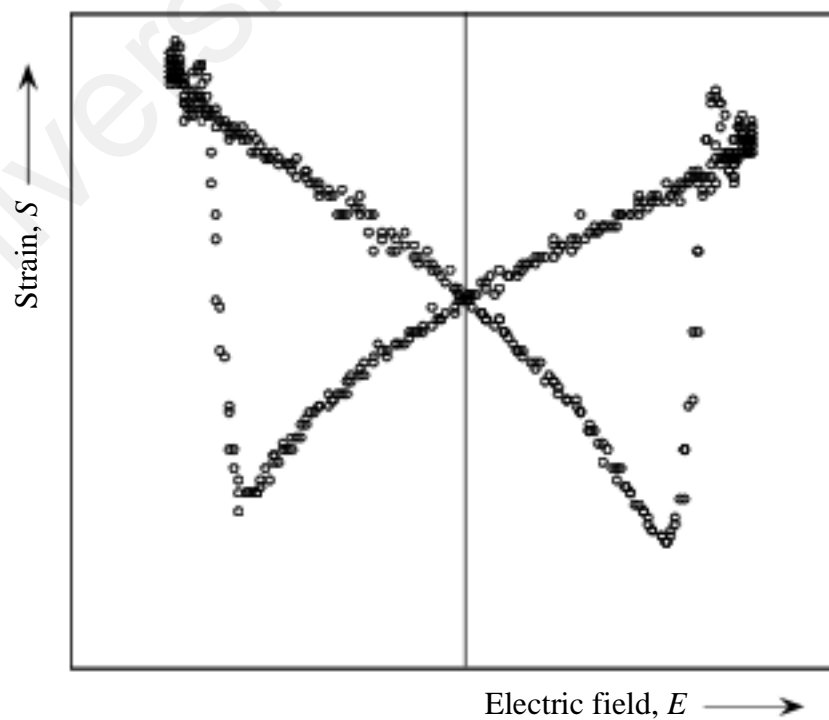


Figure 2.13: A typical S - E loop indicating switching (Jordan & Ounaies, 2001).

2.5.3 Ferroelectric Curie point and its phase transition temperatures

Another important ferroelectric characteristic is the phase transition temperature called as the Curie temperature, T_c . When the temperature increases above the Curie point, a ferroelectric crystal experiences a structural phase transition from a ferroelectric phase to a paraelectric phase. When the temperature is above T_c , the crystal is at a paraelectric state and loses its ferroelectricity. While, when the temperature is below the T_c the crystal exhibits ferroelectricity. The ferroelectric structure of a crystal is created by a small distortion of the paraelectric structure such that the lattice symmetry in the ferroelectric phase is always lower than the symmetry of the paraelectric phase. If two or more ferroelectric phases exist in a crystal, a transition temperature known as depolarization temperature, T_d occurs. The crystal transform from one ferroelectric phase to another ferroelectric phase above the T_d . Generally, above the Curie point, the temperature dependence of the dielectric permittivity can be described according to the Curie-Weiss Law (Xu, 1991).

$$\varepsilon = \varepsilon_0 + \frac{X}{T-T_0} \approx \frac{X}{T-T_0} , (T > T_0) \quad (2.41)$$

where X and T_0 denote to the Curie constant and Curie-Weiss temperature, respectively. In general, the transition into a ferroelectric phase leads to anomalies in the dielectric, elastic and optical properties, and is always accompanied with the changes in the dimensions of the crystal unit cell. The phase transition temperature of BNT can be obtained from the temperature dependence of complex dielectric spectrum.

2.6 Pyroelectric properties

In 1824, Pyroelectric effect was first discovered in tourmaline by Teophrast (S. B. Lang, 1974). Pyroelectric effect occurs in crystals that exhibit spontaneous polarization and in materials with remanent polarization. As mentioned before, all ferroelectric materials exhibit pyroelectricity but not all pyroelectric materials exhibit ferroelectricity. If there is a small uniform change of temperature, ΔT in the crystal, the change in the spontaneous polarization vector, $\Delta \mathbf{P}_i$ is written as:

$$\Delta \mathbf{P}_i = \mathbf{p}_i \Delta T \quad (2.42)$$

where \mathbf{p}_i is the pyroelectric coefficient. It is a vector with three components and describes the change in the electrical charge per unit surface area with a small temperature change. The unit of pyroelectric coefficient is either $\text{C}/\text{m}^2\text{K}$ or $\mu\text{C}/\text{m}^2\text{K}$ (Furukawa et al., 1984):

$$p = \frac{1}{A} \left(\frac{\partial Q}{\partial T} \right) \quad (2.43)$$

Pyroelectricity is observed when a crystal is heated uniformly and thus induces the change in polarization. A typical temperature and pyroelectric current versus time obtained during the pyroelectric measurement is shown in Figure 2.14. Pyroelectricity can be measure either with ‘clamped’ or free samples. In the first case, the shape and size of a crystal held fixed during heating, and the effect observed with the clamped crystal is called as primary pyroelectricity. In the second case, the crystal may be in free form, thus the thermal expansion occurs freely. The additional effect that is easier to achieve experimentally with free expansion is called secondary pyroelectricity. The pyroelectric coefficient of mechanically free sample is given by:

$$p_{|total|} = p_{|primary\ effect|} + p_{|secondary\ effect|} \quad (2.44)$$

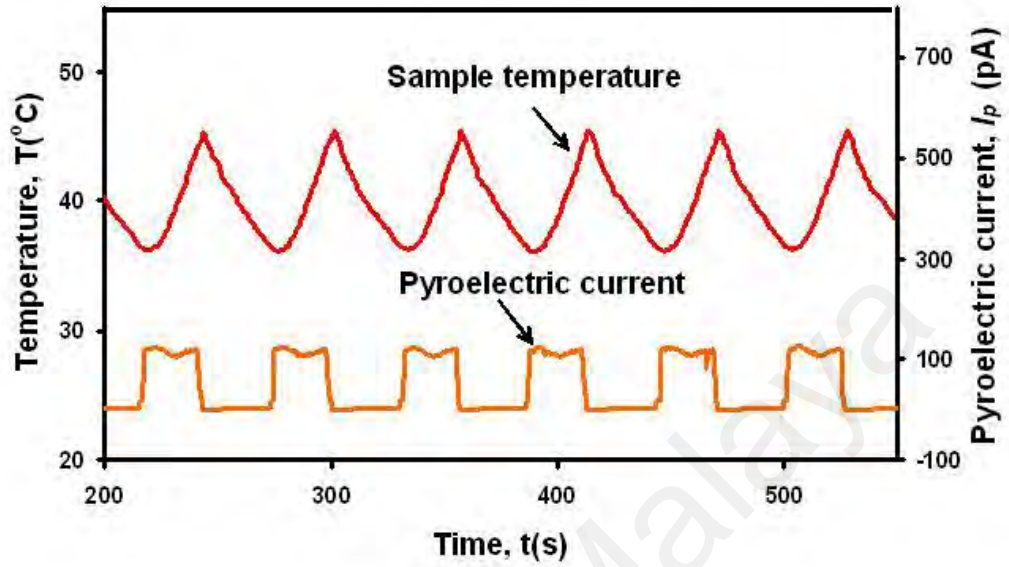


Figure 2.14: A typical triangular waveform and the rectangular short-circuited pyroelectric current spectra from the quasi-static pyroelectric measurement (Gan, 2015).

Based on thermodynamics, a relationship between electric displacement, D and the temperature change, ΔT could be derived through the “detour” demonstrated in Figure 2.15. The independent variables ΔT at electric field, E is constant. Since $D = f_1(\epsilon, T)$ and $\epsilon = f_2(\sigma, T)$, thus:

$$dD = \left(\frac{\partial D}{\partial \epsilon}\right)_T d\epsilon + \left(\frac{\partial D}{\partial T}\right)_\epsilon dT \quad (2.45)$$

$$d\epsilon = \left(\frac{\partial \epsilon}{\partial \sigma}\right)_T d\sigma + \left(\frac{\partial \epsilon}{\partial T}\right)_\sigma dT \quad (2.46)$$

When $\partial \sigma = 0$ and dividing by dT obtained:

$$\left(\frac{\partial D}{\partial T}\right)_\sigma = \overset{\text{primary}}{\left(\frac{\partial D}{\partial T}\right)_\epsilon} + \overset{\text{secondary}}{\left(\frac{\partial D}{\partial \epsilon}\right)_T \left(\frac{\partial \epsilon}{\partial T}\right)_\sigma} \quad (2.47)$$

This equation shows the measured effect divided by primary and secondary pyroelectric effect. The first term, $\left(\frac{\partial D}{\partial T}\right)_\epsilon$ in the system refers to the primary (true) pyroelectric effect at constant strain when the crystal is under clamped condition. In view of microscopic origin, this phenomenon is related to the crystal lattice reconstruction (without any deformation of the crystal) due to the temperature change.

The second term is the secondary pyroelectric effect, which describes both thermal expansion and piezoelectric effects. The term of $\left(\frac{\partial \epsilon}{\partial T}\right)_\sigma$ is defined as the pyroelectric effect measured at a constant stress when the crystal is free to change its shape. Another pyroelectric effect obtained from the pyroelectricity arises from the path $T \rightarrow \epsilon \rightarrow D$ as shown in Figure 2.15. As a result, when the crystal is free to deform or expand, an electrical displacement, D obtained from the thermal expansion. This causes a strain ($T \rightarrow \epsilon$), which in turn by the piezoelectric path ($\epsilon \rightarrow D$) contributes to the electrical displacement, D . This is called pseudo pyroelectric effect or false pyroelectric of the first kind. Temperature changes in lattice constant are related with the changes of elementary dipole moments, consequently result in the polarization (Tichý et al., 2010).

Moreover, pyroelectric effect might appear due to the internal thermal stresses. Uneven heating is the cause of this pyroelectric effect which causes non-uniform stresses and strains that produce a polarization by piezoelectric effects (Tichý et al., 2010). This phenomenon is referred as tertiary pyroelectric effect or the false pyroelectric effect of the second kind. Primary pyroelectric effect will be measured in this study to obtain the pyroelectric coefficient of ceramic and composite.

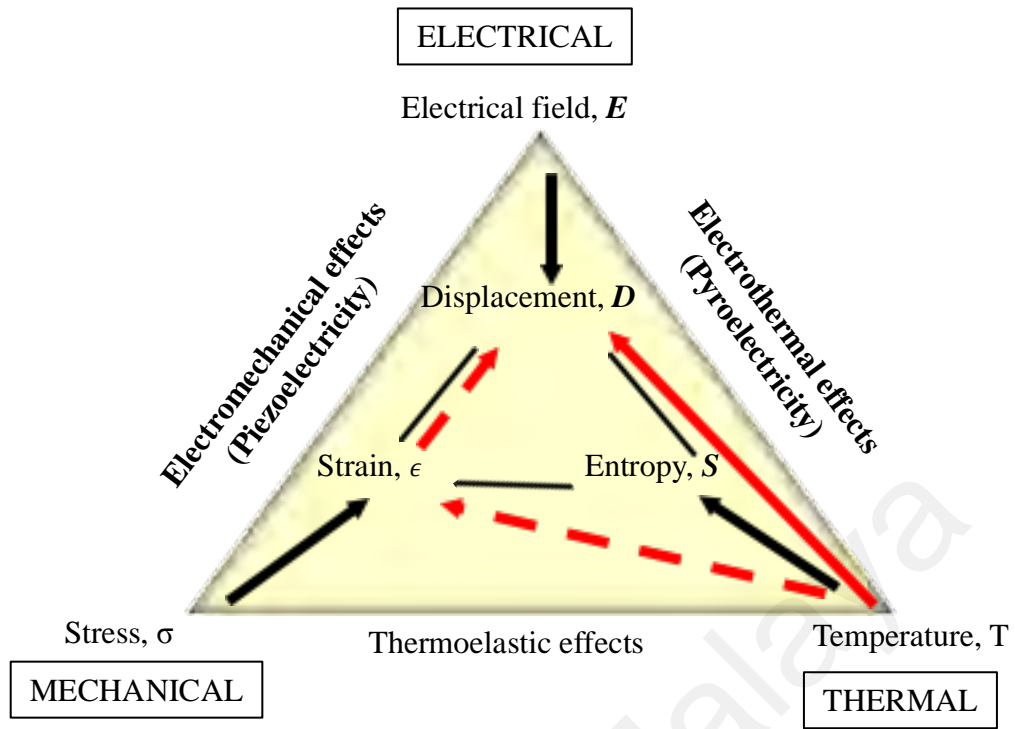


Figure 2.15: The relationships between the thermal, mechanical and electrical properties of a crystal. The solid line illustrates the primary pyroelectric effect (with strain remain constant). The red dash line illustrates the secondary pyroelectric effect when the crystal is freely deformed (Dahiya & Valle, 2013).

2.7 Summary

In this chapter, the fundamental properties of the BNT ceramic, P(VDF-TrFE) polymer and composite were presented. To date, no details of piezoelectric constants, ferroelectric and pyroelectric analysis on BNT sol gel, CeO₂ doped BNT and P(VDF-TrFE)/BNT-CeO₂ nanocomposite film are reported. By studying the structure, morphology and electrical properties, a fundamental understanding of the extra ordinary electrical properties of BNT and its polymer composite can be obtained.

CHAPTER 3: EXPERIMENTAL METHODOLOGY

3.1 Introduction

This chapter presents three major sections of experimental details. Sample preparation of BNT synthesized by sol-gel method, CeO₂ doped BNT and fabrication of P(VDF-TrFE) / BNT -0.6 CeO₂ nanocomposite either in thin or bulk films are briefly described in here. Section 3.3 presents the structural analysis and surface morphology of the samples. The principal of the electrical measurement and the experimental set up are discussed in Section 3.4.

3.2 Sample preparation

3.2.1 BNT sol gel

Sodium bismuth titanate, BNT was synthesized by using a sol gel technique. Anhydrous sodium acetate (CH₃COONa, 99.95 %, Sigma-Aldrich), bismuth (III) acetate ((CH₃COO)₃Bi, 99.99+ %, Sigma-Aldrich) and titanium (IV) butoxide (Ti[O(CH₂)CH₃]₄, 97 %, Sigma-Aldrich) were used as raw materials. 2-methoxyethanol and glacial acetic acid were selected as the solvent and the chelating agent, respectively.

The equimolar of 0.00875 mol of each starting material was used in this synthesis. First, 0.7000 g of sodium acetate was diluted in 5 ml of 2-methoxyethanol, while 3.4000 g of bismuth (III) acetate was diluted in 8 ml of glacial acetic acid and 2 ml of deionized water in a separate beaker. Then, both solutions were mixed together and stirred for 15 minutes, and subsequently 5.5 ml of titanium (IV) butoxide was added slowly. Finally, 2.8 ml of acetyl acetone as a stabilizing agent was added into the mixture and stirred at 70 °C for another 15 minutes to produce homogeneous and clear yellowish solution (see Figure 3.1(a)). The BNT sol was

dried in an oven at 100 °C for 24 hours to form BNT gel (see Figure 3.1(b)). The gel was calcined at 700 °C for 2 hours in order to evaporate the organic solvents and form dried BNT powder (see Figure 3.1(c)). Dried BNT was ground in a mortar to get fine BNT powder and pressed into a disk at 12 tones for 10 min to obtain a 13 mm diameter and ~0.7 mm thick pellet. The pellets were then sintered at various sintering temperature at either 900 °C, 1000 °C, 1100 °C or 1200 °C for 6 hours in air. Figure 3.2 shows the flowchart of the synthesis process of BNT nanoceramic using sol gel method.



Figure 3.1: The BNT ceramics (a) solution, (b) gel and (c) dried.

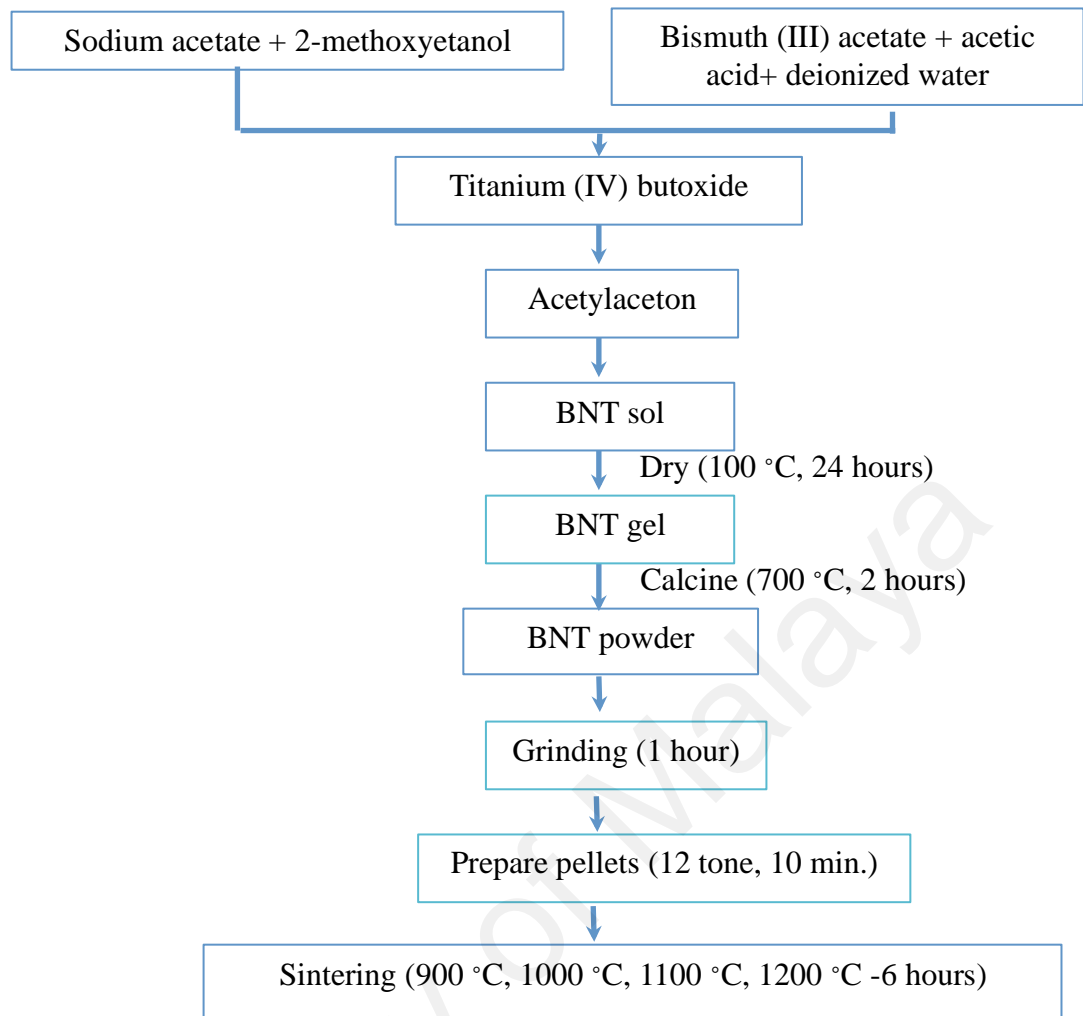


Figure 3.2: Flowcharts of BNT nanoceramics synthesis by sol gel method.

3.2.2 CeO₂ doped BNT

The calcined BNT powder were doped with cerium (IV) oxide (Ce(IV)O₂, <0.25 nm size powder, 99 %, Sigma-Aldrich) nanopowder with eight different weight percentages 0.0, 0.2, 0.4, 0.6, 0.8, 1.0, 3.0 and 5.0 wt.% by using solid state method. The mixtures were ground in mortar for 30 minutes for each percentage. Finally, CeO₂ doped BNT powder was pressed into disk at 12 tones for 10 min to obtain a 13 mm diameter and ~0.7 mm thick pellet. These pellets were sintered at 1100 °C for 6 hours in air. Silver paste used as the electrodes was fired on both surface of the disk at 100 °C for 30 minutes as an electrode. The electrode area of the ceramic samples is measured of $\sim 7.0 \times 10^{-6} \text{ m}^2$ (refer to Figure 3.3).



Figure 3.3: The BNT ceramic pellet with silver electrodes on the surface.

3.2.3 P(VDF-TrFE) / BNT - 0.6 CeO₂ nanocomposite thin films

P(VDF-TrFE) 75/25 was supplied by Koreha Corporation, Japan. Diethyl Carbonate (DEC, 99 %, Sigma-Aldrich) was used as the polar solvent for the polymer. The P(VDF-TrFE) and BNT-0.6CeO₂ powders were dispersed at different volume fractions, ϕ from 0.05 to 0.25 with 10 wt.% of DEC. Figure 3.4 shows the fabrication flowchart of the P(VDF-TrFE) /BNT-0.6 CeO₂ nanocomposite thin films.

The P(VDF-TrFE) powders were dissolved in DEC and stirred at 800 rpm and 100 °C for 15 minutes. Then, the sintered BNT-0.6 CeO₂ powders were added into the solution and stirred at 120 °C for 2 hours followed by the immersing it in the ultrasonic bath at 60 °C for 30 minutes to ensure a complete mixing and dispersion of the nanopowder in the solution. The solutions were kept at 60 °C before being transfer to an aluminum-coated glass substrate by spin coating technique. The spin-coated films were dried in the oven overnight at 60 °C to remove the residue solvent. Then, the thin film samples were annealed at 100 °C for 1 hour to increase the crystallinity of the film. Finally, (1 × 1) mm² area aluminum electrodes were then coated onto the films by thermal evaporation method to produce a metal-insulator-metal (MIM) thin film device (see Figure 3.5). The thickness of the thin film was measured using KLA Tencor P-6 mechanical profiler. The thickness of the films was in the range of 700 to 900 nm.

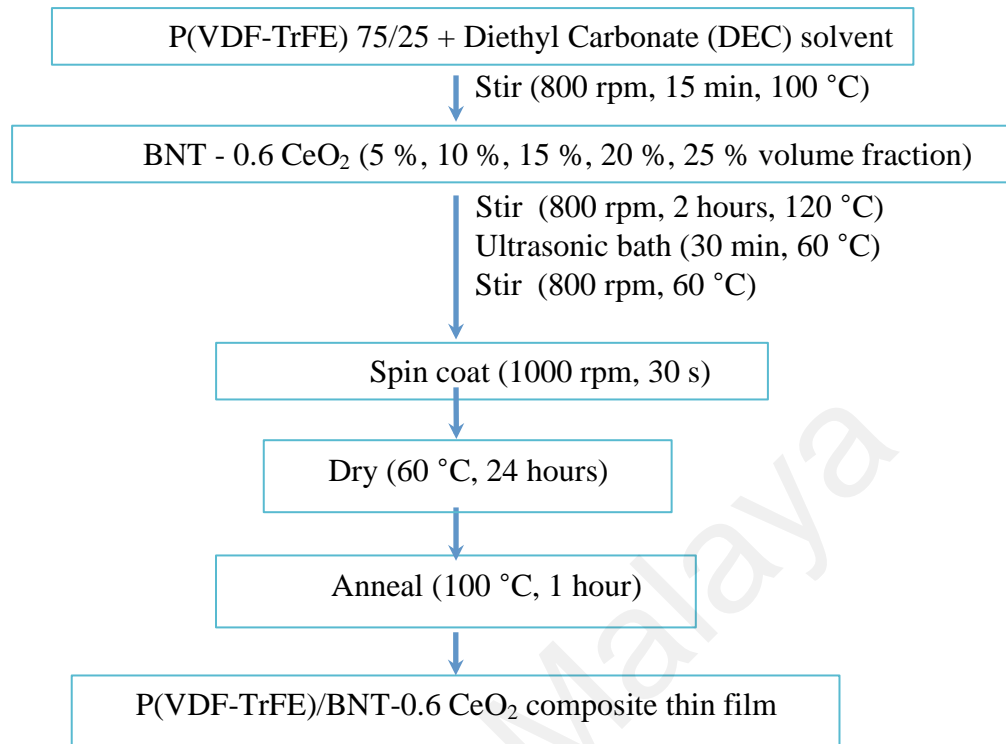


Figure 3.4: Fabrication flowchart of the polymer/ceramic composite thin films.

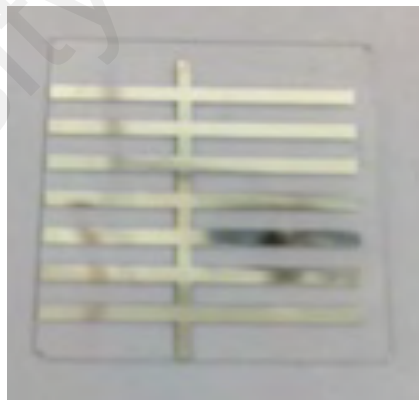


Figure 3.5: MIM structure of P(VDF-TrFE) /BNT-0.6 CeO₂ thin films.

3.2.4 Preparation of 0.2(P(VDF-TrFE) / BNT - 0.6 CeO₂) nanocomposite thick films

The piezoelectric properties of thin films normally measured using piezoresponse free microscopy (PFM). However, PFM is not available here, thus a free standing film was prepared to measure the piezoelectric properties of the nanocomposites. The free standing films of 0.20 volume fraction of the P(VDF-TrFE) /BNT-0.6 CeO₂ nanocomposite was prepared. P(VDF-TrFE) powders were dissolved in 10 wt.% DEC solvents and stirred at 800 rpm, 100 °C for 15 minutes. Then, 0.2 volume fractions of BNT-0.6 CeO₂ powders were added into P(VDF-TrFE) solvent and stirred at 120 °C for 2 hours. Subsequently, the solution was immersed in the ultrasonic bath at 60 °C for 30 minutes, and then stirred again for another one hour to ensure complete mixing and dissolution of the solutions. The resulting composite solution was poured into an open glass container and dried in the oven for one day at 50 °C. The bulk composite was annealed at 100 °C for one hour to improve the crystallinity of the polymer. The thickness of the bulk composite is about ~30 µm. Finally, (1 × 1) mm² area aluminum electrodes were then deposited on both side of the free standing 0.2 (P(VDF-TrFE) /BNT-0.6 CeO₂) thick nanocomposite film via a thermal evaporation method. Figure 3.6 shows the 0.2 (P(VDF-TrFE) /BNT-0.6 CeO₂) thick nanocomposite film with aluminium electrode deposited on both side of the sample.

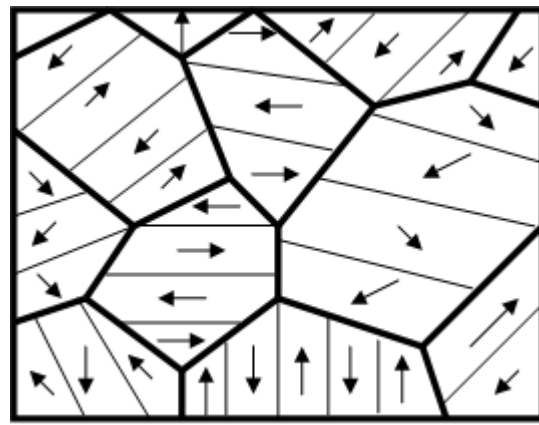


Figure 3.6: The 0.2 (P(VDF-TrFE) /BNT-0.6 CeO₂) nanocomposite thick film.

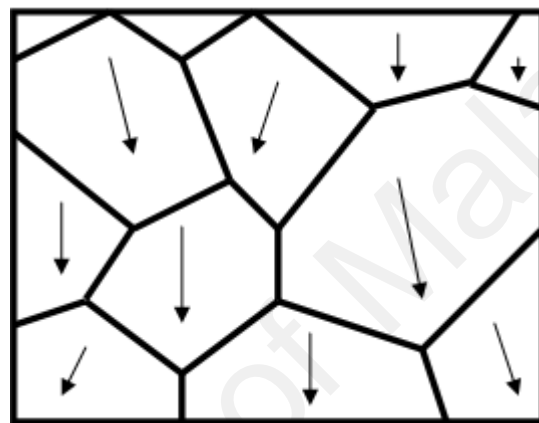
3.2.5 Poling process

In order to enhance piezo- and pyroelectricity, the ferroelectric materials are poled. The dipoles in the ferroelectric materials can be switched by applying a high electric field and this process is called as poling process. During poling dc electric field higher than the coercive field, E_c is applied to a multi domain ferroelectric to acquire a net remnant polarization, P_r , which gives an orientational spontaneous polarization in the materials. The E_c is in general minimum near the Curie temperature, T_c or depolarization temperature, T_d . Before poling, the net spontaneous polarization is zero because of the direction of the dipoles in domains is randomly distributed and cancels off each other (see Figure 3.7(a)). Poling process will realign the polar axes of the dipoles in the direction of the applied electric field as shown in Figure 3.7(b).

In this study, ‘hysteretic’ and field-cooled poling methods are applied to pole the thin films and the bulk films respectively. The hysteresis poling process uses alternating current (a.c) while field cooled poling method uses direct current (d.c). The d.c field-cooled poling method is shown in Figure 3.8. The hysteretic poling was applied during the ferroelectric measurement by using hysteresis measurement apparatus at room temperature. For the field-cooled poling, an electric field was applied on the samples at near to the depolarization temperature, T_d in order to induce its piezoelectricity and pyroelectricity.



(a) Before poling



(b) After poling

Figure 3.7: A schematic drawing of a polycrystalline ferroelectric with random orientation of grain (a) before and (b) after poling (Gan, 2015).

The ceramic and bulk polymer composite samples were poled by field-cooled method. The ceramic samples were poled at temperature of 180 °C with an applied dc electric field varying between 4 MV/m to 5.5 MV/m for 30 minutes. The samples were then cooled to room temperature for one hour without removing the electric field. Since the piezoelectric constants of ceramic and copolymer have opposite sign, the bulk composite film was poled in the opposite direction by stepwise process. First, 166 MV/m electric field was applied through the bulk film sample at 60 °C for one hour, then field-cooled to room temperature for one hour. In order to produce polarization of the ceramic phase in a direction opposite to the copolymer, the sample was reheated to 50 °C and a poling field of 16 MV/m was then applied in the

reverse direction for one hour. Then, the sample was cooled to room temperature with the application of the reverse poling. The electric field was then switched off after the sample was cooled to room temperature. Since the applied field of the composite is much lower than the coercive field of the copolymer, the polarization in the copolymer phase is not affected while the polarization in the ceramic phase is reversed.

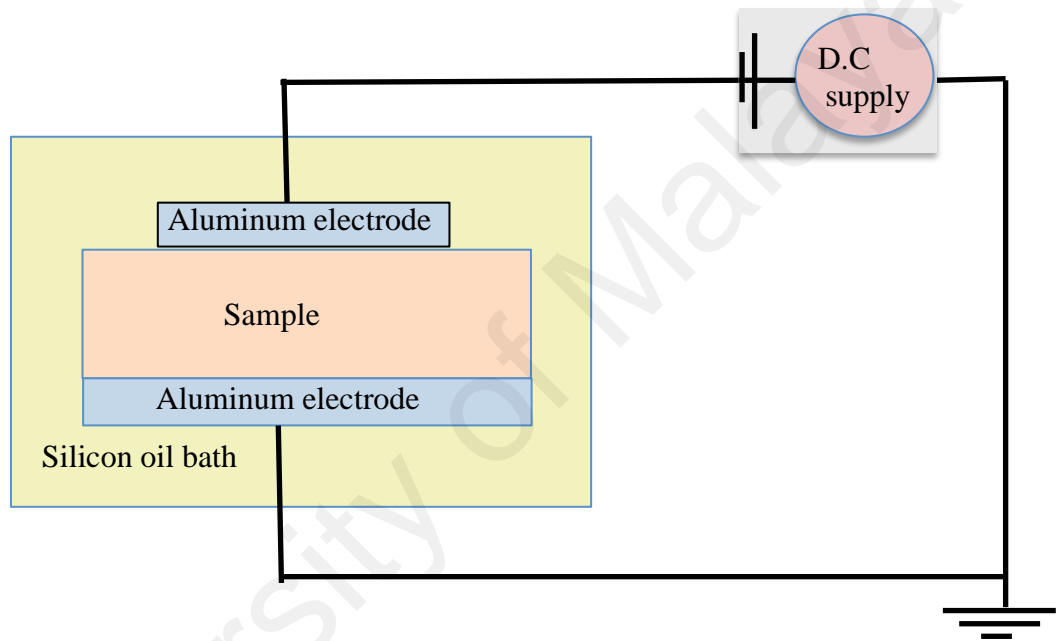


Figure 3.8: Schematic drawing of d.c poling system.

3.2.5.1 Experimental considerations

The samples treated under high electric field during the poling process leads to dielectric breakdown. In order to prevent arcing or dielectric breakdown that will permanently damage the samples, the samples were immersed in a silicone oil bath. Moreover, application of high voltages for prolonged period during the polling process must be avoided because a large amount of space charges will be injected into the samples during the poling process. Another important fact to take note is that the electrodes must be evaporated on the samples and using a pressed-on electrode

with copper or aluminum tape should be avoided. The poor contact between electrode and samples by pressed electrode caused distribution of inhomogeneous poling field and may lead to space charges trapped between surface and interface of the sample. Lastly, the samples are discharged by short circuit right after the poling process to remove the excessive charges.

3.3 Structural analysis

3.3.1 Thermo gravimetric / differential thermal analysis

Thermo Gravimetric (TG) or Differential Thermal Analysis (DTA) is used to determine the thermal behavior of the samples. The change in mass in relation to the change in temperature during the heating process is evaluated using this method. The change in mass occurs due to decomposition, oxidation or loss of volatile solvents (such as moisture) in the sample. TG/DTA is commonly employed in materials such as ceramics and polymers to identify the thermal stability and degradation temperature. In this work, TG/DTA Analysis (Q500 V20) was used to investigate the mass decomposition of organic elements in the BNT gel and to identify the suitable calcination temperature in forming the BNT nanoparticles.

3.3.2 X-ray diffraction

X-ray diffraction (XRD, Siemens D500) measurement was carried out to examine the phase and crystalline structure of BNT ceramic and its polymer composite. XRD measurement was carried out using a Siemens D500 diffractometer with CuK α radiation ($\lambda = 1.54060 \text{ \AA}$) over a wide range of 2θ (5° to 70°) with a step size of 0.02° . The crystallite size of the BNT nanopowder was determined by means of X-ray line broadening method using Scherrer equation: $d = k\lambda / \beta_{hkl} \cos\theta$, where, d is the crystallite size in nanometers, λ is the wavelength of the radiation (1.54060 \AA

for CuK α radiation), k is the shape factor ($k = 0.89$), β_{hkl} is the broadening of the hkl diffraction peak at half-maximum intensity (in radians) and θ is the Bragg diffraction angle. The crystallite size is also compared with the value obtained from the TEM image.

3.3.3 Fourier transform infrared spectroscopy

Fourier transform infrared (FTIR) spectroscopy is a characterization technique that identifies the chemical bonding of the organic and inorganic materials. IR radiation constitutes a broad electromagnetic spectrum ranging from visible to microwave regions, covering wavenumber from 4000 to 400 cm^{-1} . The chemical bonding can be detected from the wavelength of the infrared absorption spectrum. The chemical bonds of the molecules possess a characteristic of absorption frequency and the resulting spectrum can be used as a “fingerprint” for the chemical bonds existing in the materials. In this study, Perkin Elmer 2000 FT-IR spectroscopy system was used to measure the chemical bonding of the P(VDF-TrFE) thin films in the transmission mode.

3.3.4 Surface morphology

The particle size and morphology were investigated by high-resolution transmission electron microscopy, HRTEM (JEOL-JSM-7600F) and field electron scanning electron microscopy, FESEM (JEOL-JSM-7600F).

HRTEM is a powerful tool where a high energy beam of electrons is shone through ultrathin specimen and the interaction between the electron and atoms of the specimen can be analyzed and interpreted. It is used to observe features such as crystal structure and features in the structure like dislocation and grain boundaries. In this work, HRTEM was used to observe the morphology and lattice fringes of the

polycrystalline nanoparticles of BNT. In order to prepare the sample for HRTEM measurement, a small amount of BNT powders were dispersed into ethanol. One or two drops of the solution were dropped on the top surface of cooper grid and then, dried in the oven for two days prior to the measurement.

Field electron scanning electron microscopy, FESEM provides topographical and elemental information at the magnifications of 10x to 300,000x with virtually unlimited depth of field. FESEM produces clearer, less electrostatically distorted images with spatial resolution down to 1.5 nanometers. A field-emission cathode in the electron gun, generate electrons which are supplied to the surface of the sample in the FESEM. The surface of the sample generates the lower energy secondary electrons. An image of the sample surface is constructed by measuring the intensity of the secondary electron as a function of the position of the scanning primary electron beam. The surface morphology image of the samples is used to measure the average size of the particles by using the Image J software. Moreover, FESEM measurement is also performed on the polymer and polymer/ceramic composite films to observe and compare the distribution of ceramic in the polymer matrix at various ceramic compositions.

3.4 Electrical measurements

3.4.1 Dielectric measurements

The impedance analyzer measures the real and imaginary part of an impedance vector and then convert them into the desired parameters such as capacitance (C), inductance (L), impedance (Z) and etc. In this work, dielectric properties and piezoelectric properties of the ceramic and the polymer/ceramic composite were measured using Impedance Analyzer (Agilent 4294A) at the frequency range of 40

Hz to 110 MHz. The measurement results were expressed in terms of either the complex permittivity:

$$\varepsilon^* = \varepsilon' - i \varepsilon'' \quad (3.1)$$

or the complex conductivity:

$$\sigma^* = \sigma' + i \sigma'' \quad (3.2)$$

The complex conductivity is converted from the permittivity using the following equations:

$$\sigma' = \omega \varepsilon'' \quad \text{and} \quad \sigma'' = \omega \varepsilon' \quad (3.3)$$

where, ω is the angular frequency, $\omega = 2\pi f$ (where f is the frequency).

The free relative dielectric permittivity, ε' is defined as the ratio of the material permittivity to the permittivity of free space. It is calculated from the equation below:

$$\varepsilon' = \frac{Ct}{\varepsilon_0 A} \quad (3.4)$$

where C is the capacitance in Farads, t is the thickness of the film, ε_0 is the permittivity of free space (8.85×10^{-12} F/m) and A is the area of an electrode. The imaginary permittivity, ε'' is obtained from the equation below:

$$\varepsilon'' = \varepsilon' \tan \delta \quad (3.5)$$

where $\tan \delta$ is the dissipation factor.

3.4.2 Piezoelectric measurements

There are two methods used for the piezoelectric measurements in this study. The piezoelectric properties of the ceramic samples were measured using resonance method from the dielectric spectra. The ceramic pellets were poled prior to the measurement to observe a prominent piezoelectric resonance.

The piezoelectric properties of bulk free standing composite film were measured using d_{33} meter (model YE2730A). The d_{33} meter is shown in Figure 3.9. The composite film was clamped and a low frequency forced was applied. A direct reading of piezoelectric coefficient, d_{33} is obtained from the d_{33} meter. The piezoelectric coefficient, d_{33} represents charges per unit force in the direction of polarization.



Figure 3.9: The d_{33} meter (model YE2730A).

3.4.3 Ferroelectric measurements

The ferroelectric hysteresis loop was measured using Radiant Technology Precision LC Analyzer at room temperature. The P - E hysteresis loop can be observed by a Sawyer-Tower circuit (see Figure 3.10). An alternating voltage, V applied through a pair of electrodes on the surfaces of a ferroelectric crystal, C_x , which is placed on the horizontal plates of an oscilloscope. Thus, the quantity plotted on the horizontal axis is proportional to the field across the ferroelectric sample, C_x .

A linear capacitor, C_o is connected in series with the ferroelectric sample, C_x . The voltage applied across C_o is therefore proportional to the polarization of the ferroelectric sample. An oscilloscope is used to monitor the voltage.

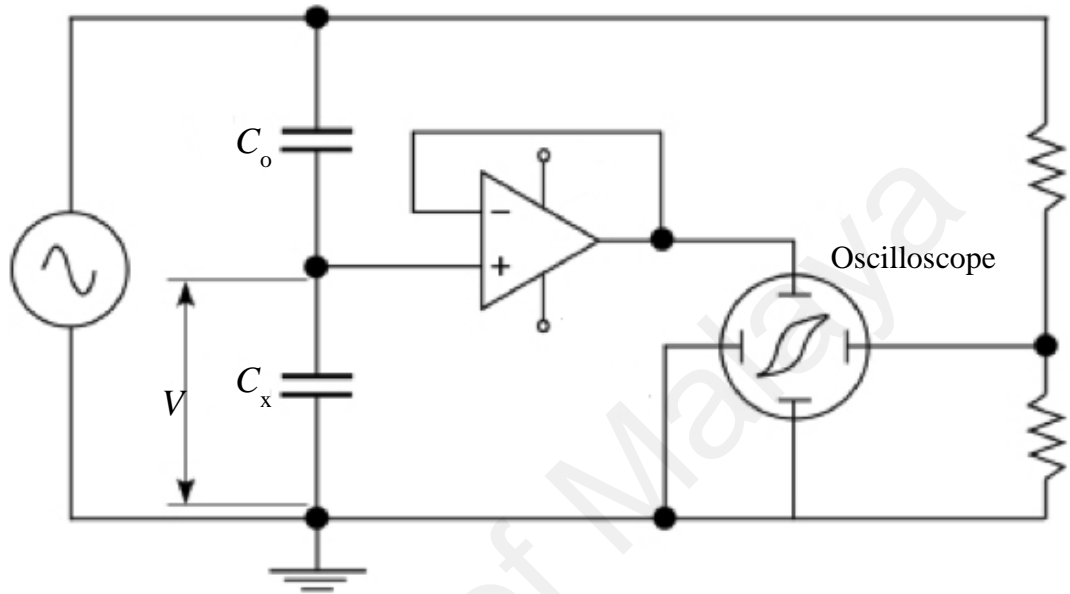


Figure 3.10: Schematic circuit of a Sawyer-Tower bridge for ferroelectric characteristic.

The P - E hysteresis measurements were performed by applying ac electric field on the sample. A sinusoidal waveform electric field was applied to the samples at frequency of 100 Hz at room temperature. The voltage step size was increased for every 10 V. A high voltage is applied through the electrode to produce an electric field across the sample area. The thicker the sample (i.e. ceramic pellets) the higher the voltage is required compared to the thinner samples (i.e. polymer/ceramic composite films). The samples were immersed in a silicon oil bath during the measurement to prevent dielectric breakdown.

3.4.4 Pyroelectric measurements

The pyroelectric coefficient of the poled ceramic and thin film samples was measured using quasi-static method. Triangular temperature waveforms with five different heating rates (0.6 °C/s, 0.9 °C/s, 1.2 °C/s, 1.5 °C/s and 1.8 °C/s) at the temperature ranging from 25 °C to 30 °C were applied to the samples and the resultant short-circuited pyroelectric current was measured. The triangular waveform range was generated using LakeShore temperature controller and the pyroelectric current, I_p was measured using a Keithly 617 electrometer. The pyroelectric coefficient, p is then evaluated using the equation below:

$$p = \frac{\Delta P}{\Delta T} \quad (3.6)$$

where ΔP is the change in spontaneous polarization of the samples and ΔT is the change of temperature.

3.4.4.1 Experimental considerations

In the quasi-static pyroelectric measurement, it is important to note that the non-uniform heating and injected space charges requires serious attention during the measurement. Non-uniform heating on the sample will results tertiary pyroelectric effect. Note that the temperature change applied in this experiment is 5 °C (25 °C to 30 °C) and it was increased and subsequently decreased at a constant rate by a non-radiative heat source. If the magnitude of the temperature change of the sample was set higher than 5 °C and the temperature change during heating and cooling are not constant during the experiment, the temperature supplied to the sample will not be able to follow the set-point temperature. As a result, the sample's temperature may be

significantly out of phase from the set-point temperature and exhibits lower magnitude of pyroelectric current compared to that of the expected result.

3.5 Summary

In this chapter, synthesis methodology of pure BNT nanoceramic and polymer/ceramic composite were discussed and the characterization techniques used in this research were illustrated. The optimized sintering temperature of BNT is subsequently used to sinter the CeO₂ doped BNT ceramic samples. The pure BNT samples were doped with various weight percentage of CeO₂ by using solid state reaction method. The optimized weight percentage of CeO₂ doped BNT ceramics was selected to be mixed with P(VDF-TrFE) polymer in order to form polymer/ceramic nanocomposite thin films. The structural and electrical characterizations were performed on the ceramic, polymer thin film and polymer/ceramic nanocomposite thin film. The bulk polymer/ceramic nanocomposite film with the optimized volume fraction was prepared in order to measure the piezoelectric coefficient.

CHAPTER 4: BNT CERAMICS PREPARED BY SOL-GEL METHOD

4.1 Introduction

Generally, BNT ceramics are synthesized by conventional solid state reaction method. However, samples prepared using this technique usually results in larger particles sized which are in micron (Jumali et al., 2012). Moreover, formation of secondary $\text{Bi}_2\text{Ti}_2\text{O}_7$ is difficult to control (Jumali et al., 2010). This synthesis method is also proven to be difficult in maintaining chemical homogeneity of the obtained powders since the reaction among the solid powders of starting materials is heterogeneous (Kim et al., 2007). Many researchers have developed alternative methods to replace the conventional solid state method in order to form nano size particles. Among the alternative methods are emulsion, pyrosol and sol gel using either citrate and steric acid as a solvent (Cernea et al., 2010; Ghitulica et al., 2013; Hao et al., 2005; Kim et al., 2007; Smolenskii et al., 1961). Piezoelectricity of ceramic can be enhanced by decreasing the domain size of the ceramic (Hoshina et al., 2008; Wada et al., 2008). This can be done by reducing the grain size of the ceramic (Cao & Randall, 1996; Zheng et al., 2012). BNT ceramic made by sol-gel method has been reported to produce nanoscale particle and thus a low electric field required to pole the ceramic: The ceramic synthesized by sol-gel method is also reported to exhibit high piezoelectric properties (Hao et al., 2005; Remondiere et al., 2008; Zhao et al., 2003). In this chapter, the structure and the electrical properties which includes dielectric, pyroelectric, piezoelectric and ferroelectric properties of BNT ceramic synthesized by the sol-gel method were thoroughly examined and reported.

4.2 BNT samples at different sintering temperatures

The BNT samples were sintered at various temperatures as mentioned in Chapter 3. The samples changed in color as the sintering temperature was increased from 900 °C to 1200 °C. The image of the sintered samples is shown in Figure 4.1. The 900 °C sintered pellet was light yellow in color and turned to darker yellow as the sintering temperature increased. The change in color is due to the volatilization of A-site element from the BNT ceramic (Chen et al., 2008)

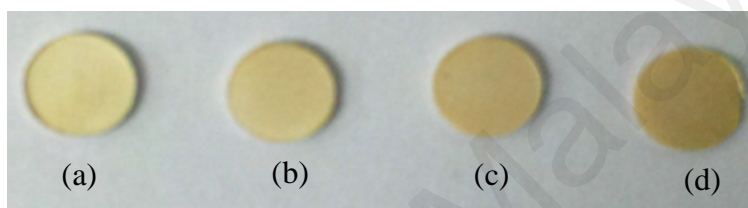


Figure 4.1: BNT pellets at the different sintering temperatures (a) 900 °C, (b) 1000 °C, (c) 1100 °C and (d) 1200 °C.

4.3 Thermogravimetric analysis

The TG and DTA curves of the dried gel of BNT are shown in Figure 4.2. There are three stages of the decomposition pathway of the gel. The first stage of the weight loss occurs at temperature ranging from 25 °C to 110 °C. It corresponds to the removal of adsorbed water on the surface of the BNT gel. The second stage of the decomposition occurs between 110 °C to ~250 °C, showing a high exothermic peak with a weight loss of 74 %. In this range, the evaporation of solvent caused some water, carbon dioxide and acetone decomposed. The last stage is in the temperature range of 250 °C to 800 °C, where carbon dioxide was decomposed (Remondiere et al., 2008). The exothermic peak shows melting temperature at 278 °C and the weight loss ended at around 500 °C. The residue of the BNT gel is 46 %. No further weight loss or peak is observed above 600 °C in the TG or DTA curves,

indicating a complete decomposition of the BNT gel. From the TG/DTA results, the suitable calcination temperature was determined which is 700 °C and was selected in forming the BNT nanoparticles.

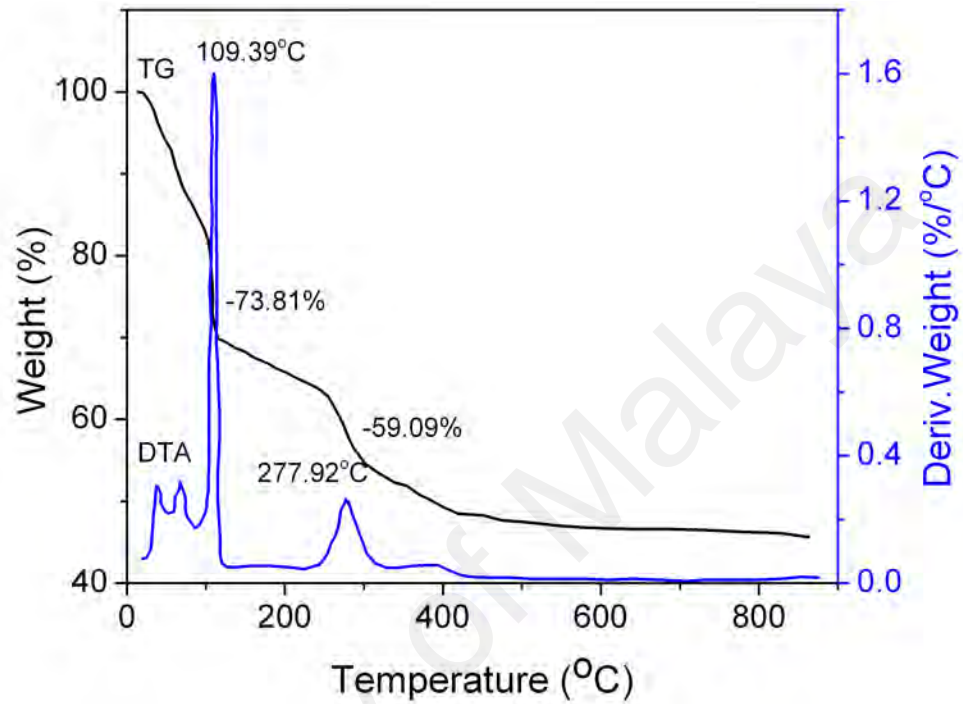


Figure 4.2: TG/DTA curves of BNT dried xerogel.

4.4 XRD analysis

Figure 4.3(a) shows the XRD patterns of BNT powder calcined at 700 °C for two hours. The diffraction peaks of the main phase from the ceramic sample indicate that the calcination temperature of 700 °C produced $\text{Na}_{0.5}\text{Bi}_{0.5}\text{TiO}_3$ rhombohedral perovskites crystal structure (Cernea et al., 2012). The intensity of the XRD peaks increased as the sintering temperature increased indicating that the crystallinity of the samples increases with sintering temperature up to 1100 °C. However, further increase of temperature 1200 °C, the crystallinity decreased (refer to Figure 4.3(b)). Moreover, at 1200 °C, peaks of a secondary phase are observed (see Figure 4(a)). The volatilization of A-site element from BNT is reported to occur at high sintering

temperature causing the oxygen vacancies. The oxygen vacancies induce the secondary phase. The secondary phase was deterred by using an excess of volatile Na and Bi precursors (Alonso et al., 2009) or by using an oxygen atmosphere in combustion (Yu et al., 2007).

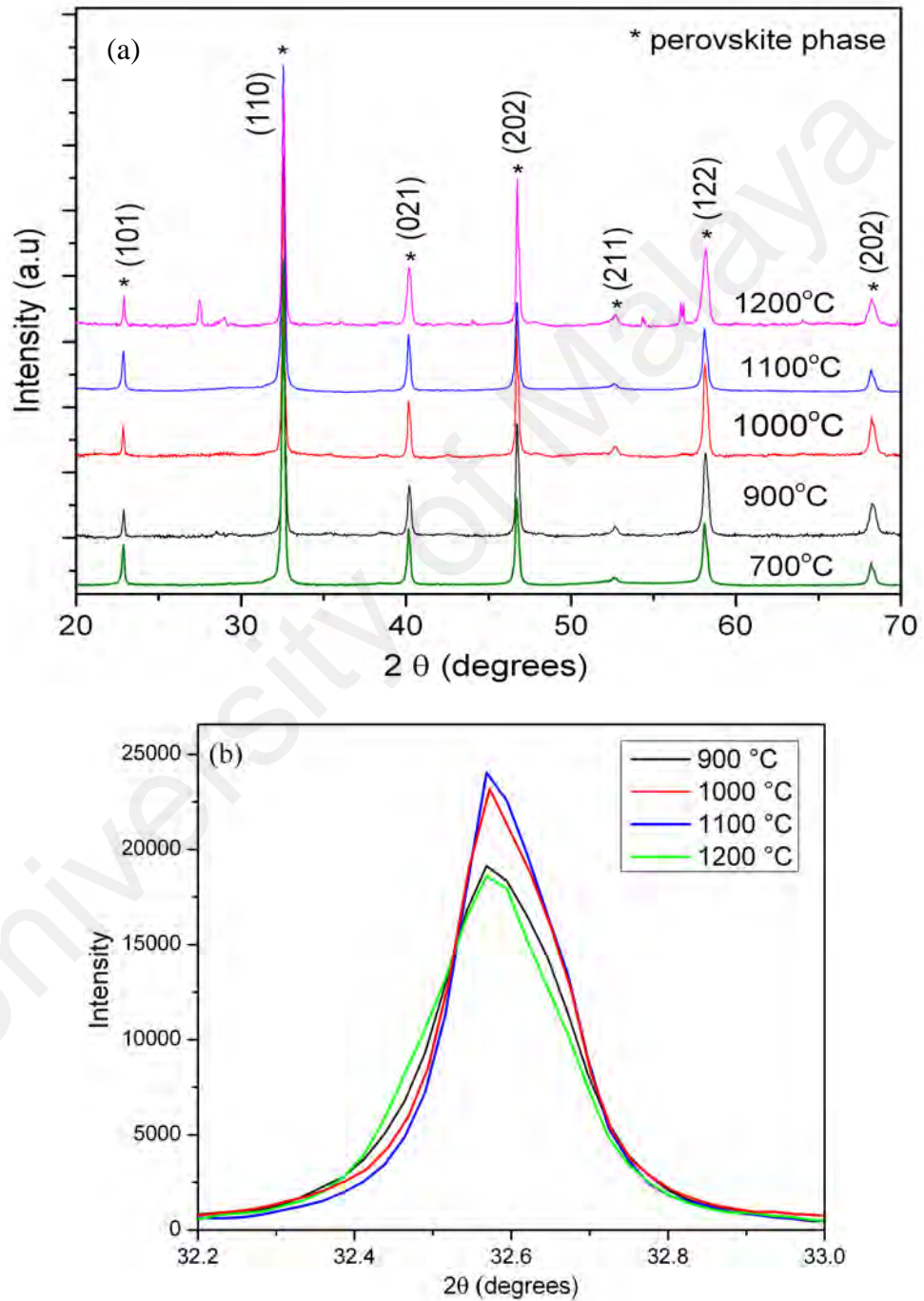


Figure 4.3: XRD patterns; (a) BNT powder calcined at 700 °C and sintered pellets at 900 °C, 1000 °C, 1100 °C and 1200 °C. (b) 2θ between 32° - 33°.

4.4.1 Determination of crystallite size by Scherrer analysis

The XRD result is used to calculate the peak broadening, the crystallite size and the lattice strain. The breadth of the Bragg peak is a combination effect of both instrument and the sample. The instrumental corrected broadening β_{hkl} corresponding to the diffraction peak of BNT can be estimated using the relation:

$$\beta_{hkl} = [(\beta_{hkl})^2_{\text{measured}} - (\beta)^2_{\text{instrumental}}] \quad (4.1)$$

The crystallite size, d of the BNT nanoparticles was determined by X-ray line broadening method using Scherrer equation as below (Panigrahi, 2010):

$$d = \frac{k\lambda}{\beta_{hkl} \cos \theta_{hkl}} \quad (4.2)$$

where, d is the crystallite size in nanometers, λ is the wavelength of the radiation (1.54060 Å for CuK α radiation), k is the shape factor or the Scherrer constant ($k = 0.89$), β_{hkl} is the broadening of the hkl diffraction peak at half-maximum intensity in radians unit and θ_{hkl} is the Bragg diffraction angle. The crystallite size of the BNT samples was determined using the Scherrer equation which is 36 ± 2 nm. The crystallite size is compared with the value obtained from the TEM image (see later in Section 4.5).

4.5 HRTEM analysis of the nanocrystalline structure

The HRTEM micrographs of the BNT precursor gel at the calcination temperature of 700 °C are shown in the Figure 4.4 (a) and (b), respectively. The lattice fringes of the polycrystalline nanoparticles can be seen clearly in the TEM image (see Figure 4.4 (a)) with the distances between adjacent crystal planes (hkl), d of 2.74 Å and 1.94 Å, corresponding to the (110) and (202) crystallographic planes

of the rhombohedral phase of $\text{Na}_{0.5}\text{Bi}_{0.5}\text{TiO}_3$. The HRTEM micrograph indicated a rhombohedral $\text{Na}_{0.5}\text{Bi}_{0.5}\text{TiO}_3$ crystallographic phase shows a good agreement with the XRD analysis (see Figure 4.3(a)).

Figure 4.4(b) shows the calcined BNT particles of the particles. Most of the particles are agglomerated. The nanopowder has the tendency to form hard agglomeration when partially sintered (Cernea et al., 2012). The particle size histogram of BNT powders is shown in Figure 4.4(c). From the histogram, it can be observed that the individual particles size is quite uniform with average particle size of BNT powder which is 43 ± 13 nm. This value agrees to some value with that calculated from XRD pattern using the Scherrer equation which is 36 ± 2 nm.

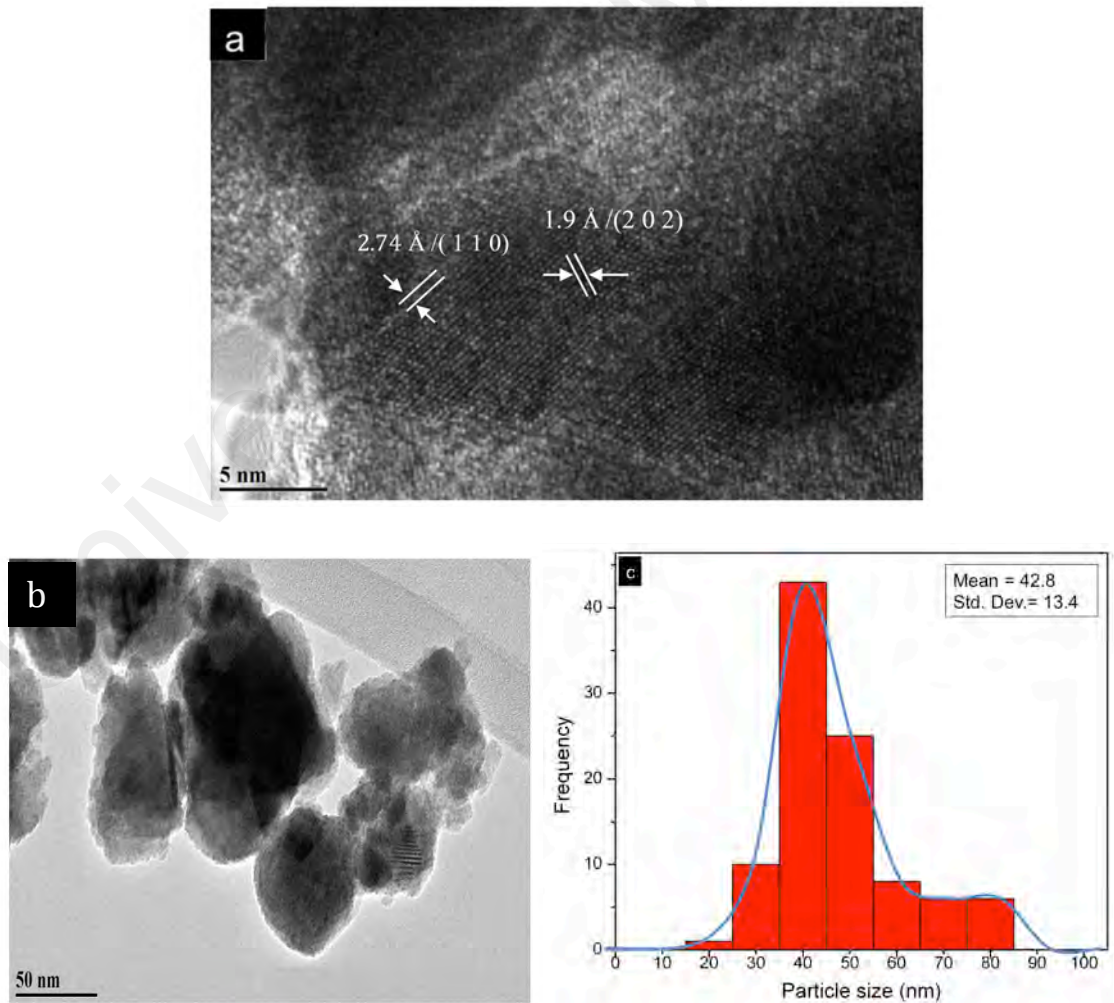


Figure 4.4: (a) and (b) are the HRTEM images of BNT powder and (c) is the histogram of particle size.

4.6 FESEM analysis

The FESEM micrographs and the grain size histogram of BNT pellet sintered at 1100 °C for 6 hours is shown in Figure 4.5 (a) and Figure 4.5 (b), respectively. The microstructure of BNT ceramic shows a dense structure with square and rectangular shapes. From the HRTEM result, the particle size obtained for non-sintered sample is ~40 nm. The grain growth during sintering process is about ten times larger than the initial BNT particles. The grains are relatively uniform and have an average size of ~0.5 μm . A very compact disk with low porosity (high density) and low grain size of the sintered ceramics offer higher mechanical strength and improved dielectric permittivity (Chu et al., 2002).

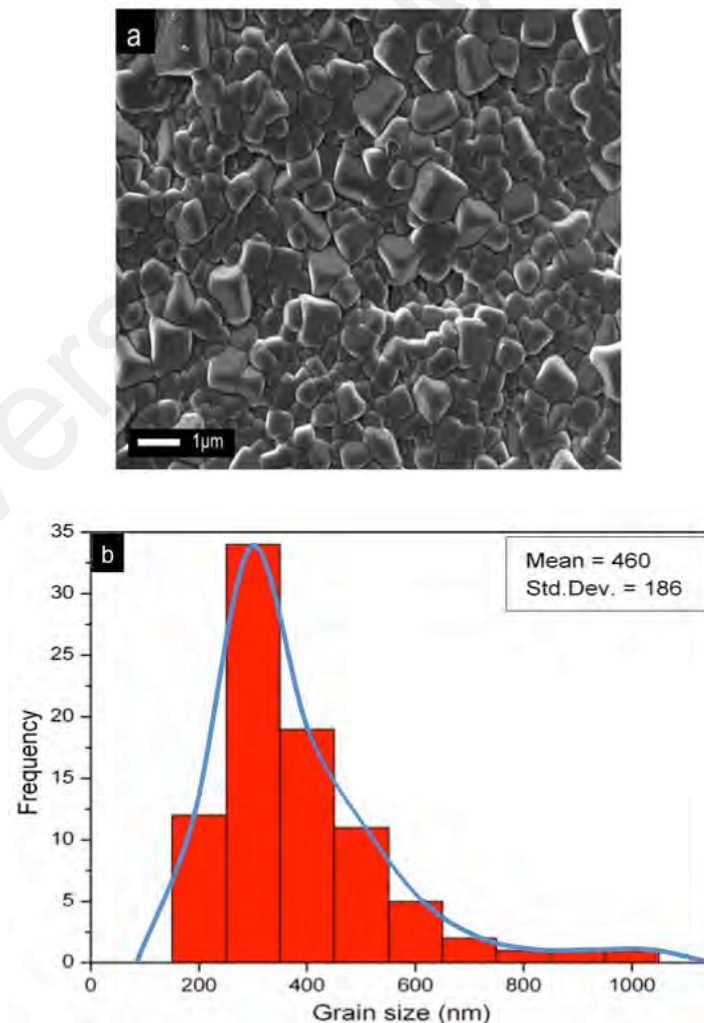


Figure 4.5: FESEM micrograph of (a) BNT pellet sintered at 1100 °C and (b) is a grain size histogram of BNT pellet.

4.7 Dielectric properties

Figure 4.6 shows the dielectric constant, ϵ' and dissipation factor, $\tan \delta$ as a function of temperature for poled and non-poled samples in the frequency range of 10 kHz to 1 MHz. A few phase transitions were observed between the ferroelectric, anti-ferroelectric and paraelectric phases in the different temperature ranges (Suchanicz & Ptak, 1990; Tadashi et al., 1991). The depolarization temperature, T_d refers to the transition temperature between ferroelectric phase and anti-ferroelectric phase. Meanwhile, the maximum temperature, T_m is the temperature at which the dielectric constant, ϵ' reaches the maximum value. In this case, $T_m = T_c$, where T_c is the Curie temperature which refers to the transition temperature between anti-ferroelectric and paraelectric phase.

The ϵ' and $\tan \delta$ were increased after the poling process. T_d and T_c were shifted to higher temperature from 215 °C to 230 °C and from 370 °C to 380 °C, respectively. The poling process causes dislocation of titanium ion from B-site element of BNT. It is well established that the spontaneous polarization of the perovskite structure of ferroelectrics mainly originates from the displacement of B site cations (Xu et al., 2005; Li et al., 2007). This charged defect of dislocation can also interact strongly with domain walls, and therefore affect the ferroelectric behavior (Kontsos & Landis, 2009). At lower frequency both poled and non-poled samples were showing higher dielectric constant. However, the dielectric constant decreases with increasing frequency. The strong dispersion at lower frequency seems to be a common feature in the ferroelectric materials due to the ionic conductivity (Yordanov et al., 1998). When the frequency increases, the relative effect of ionic conductivity reduces, thus the ϵ' reduces (refer to Figure 4.6). In contrast, $\tan \delta$ increases with frequency. With an increase in frequency, retardation in polarization

caused from ionic conductivity is enhanced which is leading to increase in $\tan \delta$ (Wang et al., 2005).

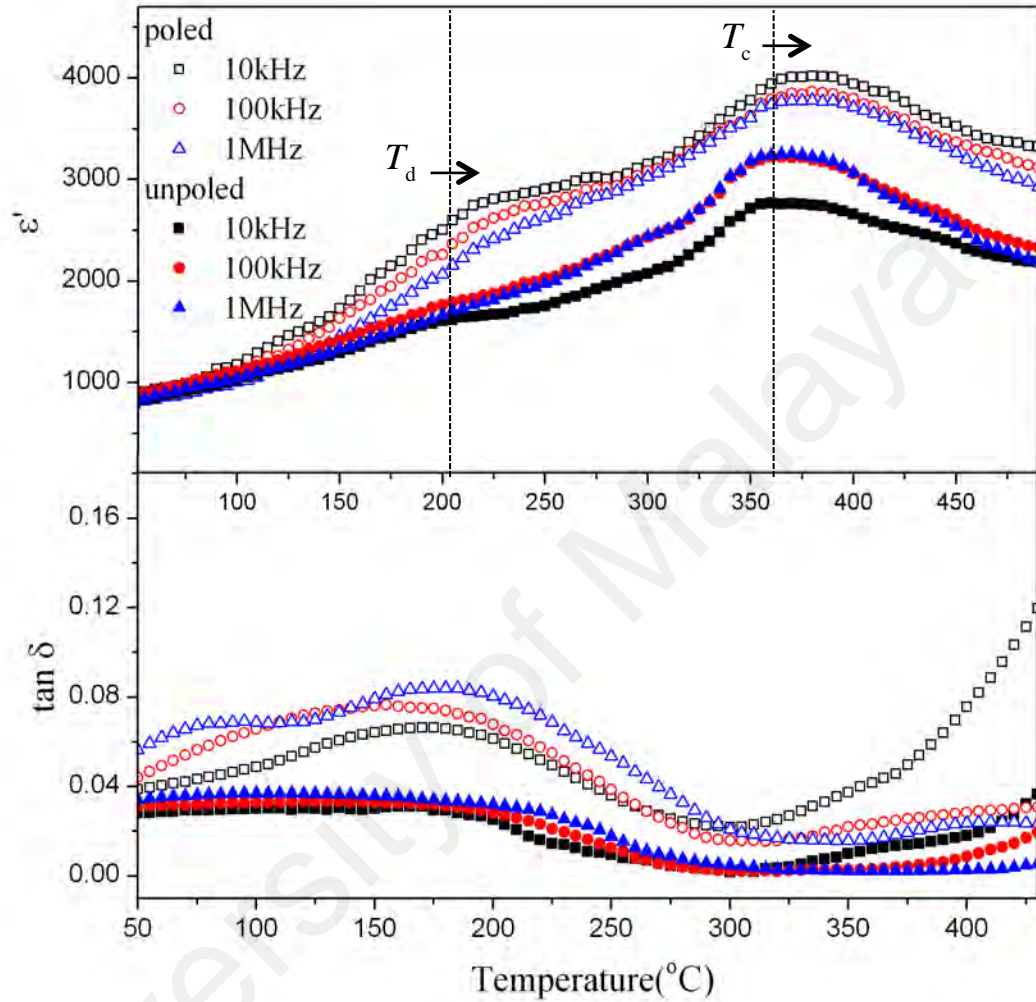


Figure 4.6: Frequency and temperature dependence of dielectric constant, ϵ' and dissipation factor, $\tan \delta$ for unpoled and poled BNT ceramic at 10 kHz - 1 MHz.

4.8 Piezoelectric properties

The electromechanical coupling coefficient, k of piezoelectric materials is an important parameter for modeling and designing piezoelectric devices. It is an indicator of the conversion efficiency between electrical and acoustic energy in a piezoelectric material. The most commonly used mode of vibration is the resonance along the poling direction. The electromechanical coupling coefficient depends on

the aspect ratio of resonator. Here, the aspect ratio is defined as the dimension of poling direction over lateral dimension. The aspect ratio represent a bar poled along the long axis in the thickness mode which yields electromechanical coupling coefficient, k_{33} . The k_{33} is defined as:

$$1 - k_{33}^2 = \frac{\epsilon_{33}^S}{\epsilon_{33}^T} \quad (4.3)$$

where ϵ_{33}^T is the dielectric constant tensor under constant stress and ϵ_{33}^S is the dielectric constant tensor under constant strain. The stiffness compliance constant (Young modulus), c_{33} is an indicator of the stiffness or elasticity of a ceramic material. The Young modulus can be obtained from:

$$f_t = \frac{1}{2t} \sqrt{\frac{c_{33}}{\rho}} \quad (4.4)$$

where t is the thickness of the ceramic, f_t is the resonance frequency and ρ is the density of the BNT ceramic. The piezoelectric constant, d_{33} can be calculated from the equation below:

$$d_{33} = k_{33} \sqrt{\epsilon_0 \epsilon_{33}^S s_{33}} \quad (4.5)$$

where s_{33} is the elastic constant, which is the reciprocal of the Young modulus and ϵ_0 is the permittivity of free space (8.85×10^{-12} F/m).

Figure 4.7(a) shows the dielectric spectra of non-poled BNT at room temperature, RT and poled BNT at temperature varied from 25 °C to 400 °C. The dielectric spectra of non-poled BNT sample did not show any thickness extensional (TE) resonance mode at RT while the poled BNT samples exhibits TE resonance mode at around 3 MHz. The TE resonance mode is also dependent on the

temperature. Prominent resonant peaks were observed from RT to T_c , while above the T_d it disappeared.

The TE resonance peak at RT for real and imaginary permittivity are displayed in Figure 4.7(b). An IGOR Pro 7 software was used to evaluate the data and fitting the resonance peaks. Using Equation 4.3 to 4.5 and by fitting the resonance peak, the electromechanical coupling coefficient, $k_{33} = 0.39$, the effective elastic coefficient (Young modulus), $c_{33} = 170$ GPa and the piezoelectric constant, $d_{33} = 74$ pC/N at room temperature were calculated, respectively.

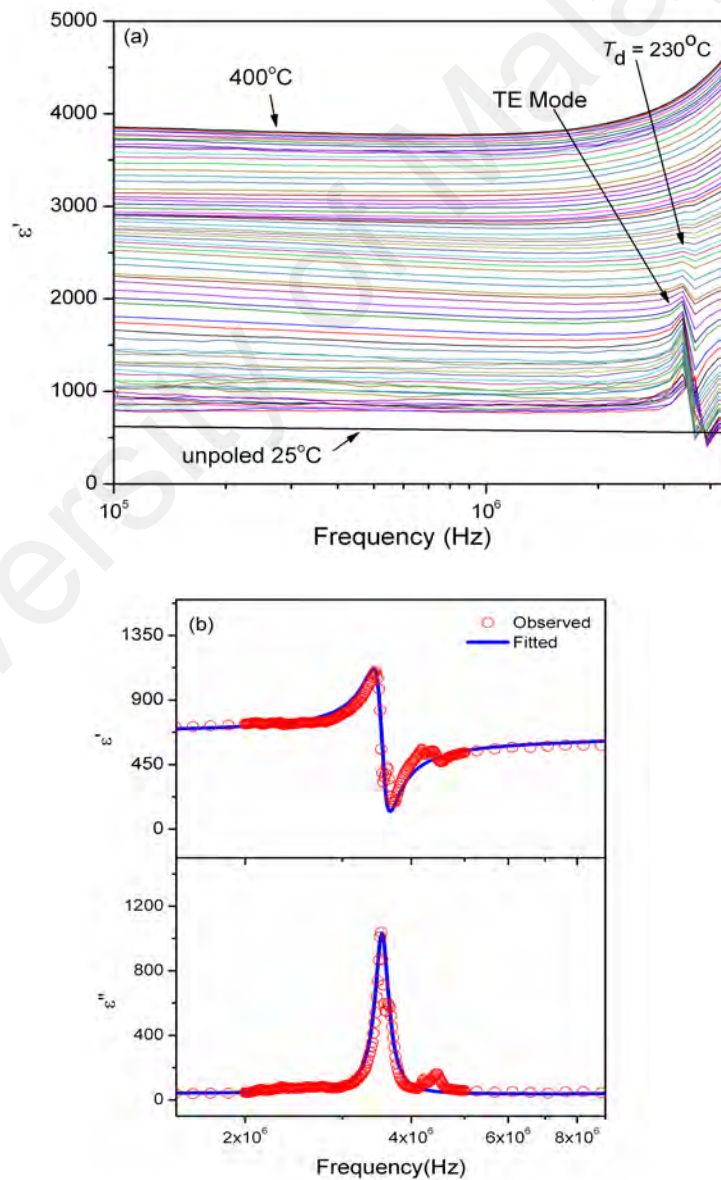


Figure 4.7: Piezoelectric resonance spectra of BNT ceramic at (a) various temperatures and (b) observed and fitted dielectric spectra.

4.9 Ferroelectric properties

Figure 4.8 shows the polarization (P) versus electric field (E), P - E hysteresis loop of the BNT ceramic at room temperature by increasing the electric field. For the applied electric field, E lower than 40 kV/cm, the P - E relation shows almost linear curve. As the E was increased, hysteresis started to emerge rapidly where the dipoles in the BNT begin to align gradually with the direction of the field and saturation polarization is reached. However, P - E measurement unable to obtain a fully saturated square hysteresis loops. This is probably due to the oxygen vacancies in the BNT crystals which may have contributed to the leakage current under the influence of high electric field (Panigrahi et al., 2010). Similar to the case of PZT ferroelectric ceramic, oxygen vacancies can restrain the movement of ferroelectric domain due to the pinning effect which can caused an enhancement of coercive field (Xu et al., 2005). The P - E hysteresis loop shows a remnant polarization, P_r of $47 \mu\text{C}/\text{cm}^2$ and a coercive field E_c of 55 kV/cm for the BNT ceramic. Table 4.1 shows the comparison of physical and electrical properties of BNT's samples synthesized in different methods (extracted from literatures). The BNT ceramic synthesized using sol-gel method (in this research) has relatively higher values compared to BNT synthesized from conventional or other methods (see Table 4.1). Further elaboration is given in Section 4.11.

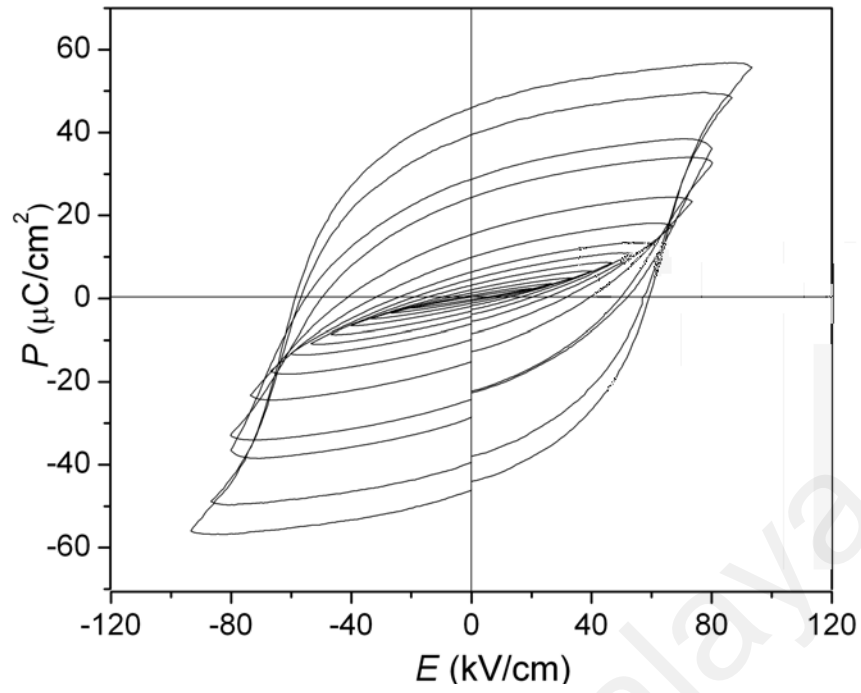


Figure 4.8: Room temperature P - E hysteresis loops of BNT ceramic measured at 5 Hz with various electric field.

The leakage current density versus electric field (J - E) of BNT ceramic sintered at 1100 °C is shown in Figure 4.9. The leakage current density increased with the increase of applied field and saturated above ~5 MV/m. The leakage currents obtained are in the order of 10^{-5} - 10^{-8} A/cm² over the electric field range of 0 to ± 10 MV/m. Moreover, the BNT samples produced by sol-gel method is dense with low porosity and have smaller grains thus leakage current is deterred in such condition.

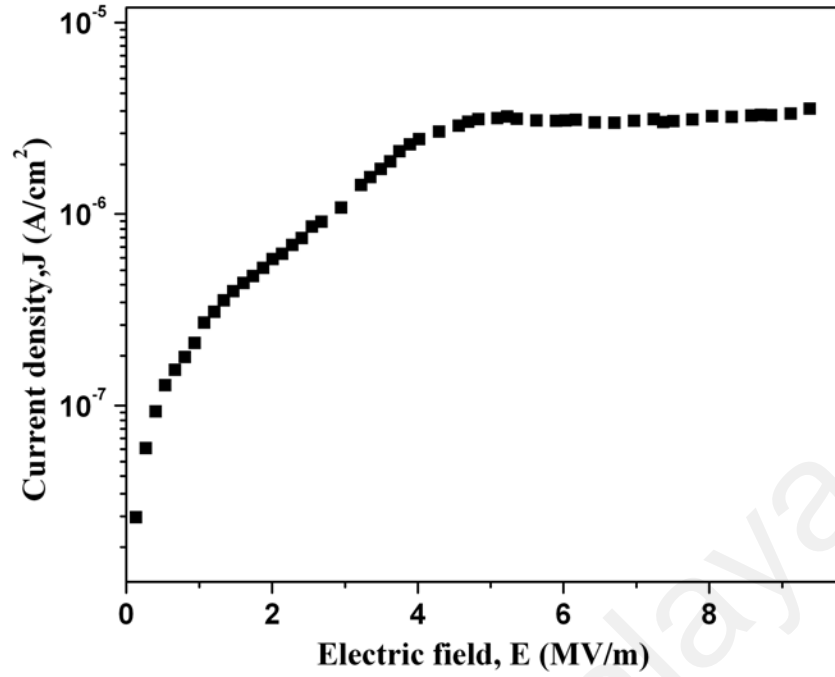


Figure 4.9: Leakage current density of BNT ceramic.

4.10 Pyroelectric properties

The short-circuited pyroelectric current of the BNT ceramic, I_p is represented by the rate change of polarization:

$$I_p = p A \frac{dT}{dt} \quad (4.7)$$

where p is the pyroelectric coefficient, A is the electrode area and dT/dt is the heating rate. Figure 4.10(a) shows a square waveform of pyroelectric current observed when a triangular waveform temperature was applied to the BNT ceramic. The pyroelectric coefficient of the effective electrode area is obtained from the gradient of the graph I_p versus dT/dt as shown in Figure 4.10(b). The pyroelectric coefficient, p of BNT was poled at room temperature by using ‘hysteretic poling’ and the p is $141 \mu\text{C}/\text{m}^2\text{K}$. However, when the same sample poled using field-cooled polling method at 4 kV and 200°C for 30 minutes exhibit higher p which is 625

$\mu\text{C}/\text{m}^2\text{K}$. Poling BNT samples near T_d yield higher pyroelectric coefficient, this effective poling technique is essential to optimize the pyroelectric properties of BNT.

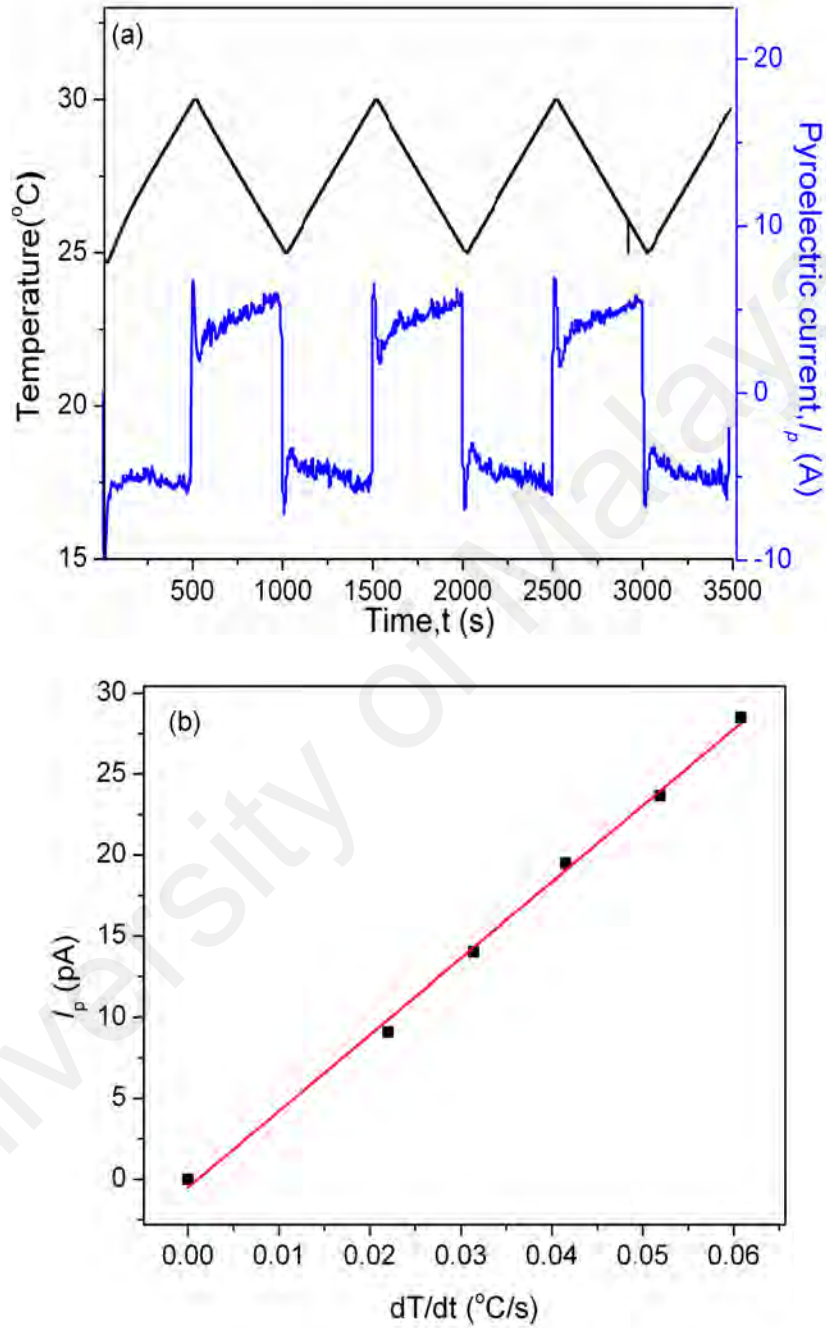


Figure 4.10: (a) The pyroelectric current of poled BNT ceramic at the heating rate $0.6\text{ }^{\circ}\text{C}/\text{min}$ and (b) plot of I_p versus dT/dt for poled BNT ceramic.

4.11 Discussion

BNT prepared from sol-gel method in this research was compared with BNT prepared with other methods such as conventional solid state method and wet chemical citrate method (refer to Table 4.1). The dielectric constant, ϵ' , piezoelectric constant, d_{33} , remnant polarization, P_r and pyroelectric coefficient, p of the BNT prepared by sol-gel method shows excellent improvement compared to the other methods. Moreover, the coercive field, E_c , has reduced to 30 % and thus managed to effectively pole the BNT sample. Therefore, the samples produced using sol-gel method show enhanced in pyroelectric and piezoelectric properties. This phenomenon can be qualitatively explained as follows. BNT prepared from solid state method produced larger particle grains which are difficult to disperse and affect the sintering properties, while the BNT samples produce using sol-gel method are homogeneous with minimal porosity compared to the solid state or citrate method.

Moreover, sintering temperature is also crucial for these samples. For example, the samples sintered at 1100 °C crystalize into rhombohedral perovskite structure and displays higher crystallinity without any form of impurities. The homogenous grain growth distribution in nanosize contributed to high interphase grain boundary and as a result exhibit better electrical properties. Besides as suggested above, effective poling neutralizes the trap charges at grain boundaries, domain pinning and reduces the E_c so that it expedites sufficient reorientation of the ferroelectric domains benefiting the achievement of desired piezoelectric and pyroelectric properties (Wu et al., 2014).

Table 4.1: The BNT ceramics in different synthesis method

Preparation method	Sol-gel method	Solid state method	Citrate method
Dielectric constant, ϵ'	885	290-524	446
Dissipation factor, $\tan \delta$	0.03	0.03-0.04	-
Remnant Polarization, P_r ($\mu\text{C}/\text{cm}^2$)	47	38	33
Coercive field, E_c (kV/cm)	55	75	80.0
Pyroelectric coefficient, p ($\mu\text{C}/\text{m}^2\text{K}$)	141-625	130-700	-
Electromechanical coupling coefficient, k_{33} (%)	39.0	41.0	18.6
Effective elastic coefficient, c_{33} (GPa)	170	-	-
Piezoelectric constant, d_{33} (pC/N)	74	57-91	60-92
References	This work	Hagiyev et al., 1984; Nagata & Takenaka, 2001; Smolenskii et al., 1961; Takenaka & Sakata, 1989	Hao et al., 2005; Xu et al., 2005

4.12 Conclusion

A high purity $\text{Na}_{0.5}\text{Bi}_{0.5}\text{TiO}_3$ powder was synthesized from a sol-gel process at 1100 °C sintering temperature with average crystallite size of 40 nm. The prepared powder was compacted into disc and sintered. The sintered BNT ceramic was dense with low porosity and exhibits homogenous grain growth. These $\text{Na}_{0.5}\text{Bi}_{0.5}\text{TiO}_3$ ceramics show relatively higher dielectric constant, piezoelectric, pyroelectric and ferroelectric properties compared to BNT prepared from conventional solid state method and sol-gel method using citrate acid. Since the lead free BNT prepared from sol-gel method exhibit excellent functional properties, it can be ideal for applications such as piezoelectric or pyroelectric sensor, actuator, and ferroelectric random access

memories (FeRAMs). Thus, the BNT sample synthesized from sol-gel method can be an alternative or better replacement for PZT which is toxic due to lead content.

University of Malaya

CHAPTER 5: CeO₂ DOPED Na_{0.5}Bi_{0.5}TiO₃ CERAMICS

5.1 Introduction

Morphotropic phase boundary of a BNT ceramic can be modified with additives such as metal oxides and rare earth oxides. Additives are reported to enhance the electrical properties of the BNT ceramics. Adding rare earth oxide materials such as La₂O₃, CeO₂, Y₂O₃ and Nd₂O₃ onto BNT are beneficial to the electrical properties depending on the nature of oxide additive (Fu et al., 2010a, 2010b; Shi & Yang, 2009; Wang et al., 2003; Zhou et al., 2009). Many researchers report that ferroelectric ceramics near the morphotropic phase boundary (MPB) between a rhombohedral and tetragonal phases exhibit a substantial improvement in poling and consequently increase their piezoelectric properties (Chu et al., 2002; Li et al., 2004) compare to that of the single phase structure.

CeO₂ has been used as a dopant for lead ceramic such as PZT to improve the density and the piezoelectric properties, while reduces the conductivity and dielectric loss of the samples (Garg & Agrawal, 1999; Shan et al., 2007; Zhang et al., 2009). In this study, we have use CeO₂ as a dopant in the BNT and studied the effects of the dopant on the electrical properties such as ferro-, pyro-, piezo- and dielectric properties.

5.2 BNT samples at various weight percentages of CeO₂.

BNT ceramics were doped with various weight percentages (0 - 5.0 wt.%) of CeO₂. The CeO₂ doped BNT samples change in color during the sintering process (refer to Figure 5.1). The color of sintered ceramics has changed from light yellow to dark brown depending on the wt.% of the dopant. The doped BNT become darker gradually as the weight percentage of CeO₂ is increased. The change of color indicates that Ce ion is incorporated into the BNT lattice and the volatilization of A-

site element from BNT has caused oxidation during the sintering process (Chen et al., 2008).

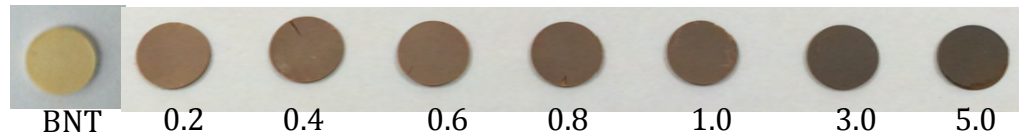


Figure 5.1: BNT- x wt.% CeO_2 pellets, ($x = 0.0 - 5.0$).

5.3 XRD analysis

Figure 5.2(a) shows the XRD pattern of CeO_2 doped BNT ceramics with different weight percentages (0 - 5.0 wt.%). A single perovskites structure can be observed when the weight percentage of CeO_2 is less than 1.0%. However, further increase of CeO_2 shows the characteristic peaks of the CeO_2 . The CeO_2 was diffused into the BNT lattice during the sintering process. However, when the amount of CeO_2 is above 1.0 wt.%, CeO_2 tends to ‘squeeze’ out of the grain and accumulate at the grain boundaries in the ceramics causes the conductive characteristic of the samples. Therefore, 1.0 wt.% is identified as the limit of CeO_2 as a dopant in the BNT ceramics.

Figure 5.2(b) shows the enlarged image of the XRD patterns in the range of $38^\circ - 48^\circ$. A splitting of peaks observed for the samples after the doping process. The pure BNT shows single rhombohedral perovskite structure. Doped samples exhibit tetragonal peaks observed from the separated split (003/021) and (202/220). The tetragonality of the ceramic lattice increased when the BNT ceramic was doped with higher percentage of CeO_2 (Liao et al., 2006). The splitted peaks indicate the existence of rhombohedral-tetragonal morphotropic phase boundary in BNT when doped with CeO_2 ceramic.

5.3.1 Determination of crystallite size

The crystallite sizes of the CeO₂ doped BNT nanoparticles were determined by means of an X-ray line-broadening method using the Scherrer equation (refer to Equation 4.2 in Chapter 4). Two planes at 32.6° and 46.7°, which have the highest intensity, were chosen to calculate the crystallite size. Table 5.1 shows the average of crystallite size of CeO₂ doped BNT samples calcined at 700 °C. The crystallite size of the BNT sample doped with 0.2 wt.% CeO₂ remains unchanged compare to the pure BNT which is around ~44 nm. However, the crystallite size was reduced from 44 ± 2 nm to 32 ± 2 nm as the weight percentage of CeO₂ increases to 0.6 wt.%. Further increase in the weight percentage of CeO₂ (above 0.8 wt.%) caused the crystallite size to increase to ~50 nm.

Table 5.1: The crystallite size of BNT- x wt.% CeO₂

x wt.% CeO₂	2θ(°) ±0.1	FWHM ±0.0001	Average Crystallite Size (nm) ± 2	
0.0	32.6	0.2263	43.8	44
	46.7	0.2863	44.5	
0.2	32.6	0.1661	43.3	43
	46.7	0.1158	43.0	
0.4	32.6	0.1685	35.3	35
	46.7	0.1067	35.0	
0.6	32.6	0.1675	31.5	32
	46.7	0.2063	31.8	
0.8	32.6	0.1624	49.0	48
	46.7	0.1037	48.6	
1.0	32.6	0.1570	50.7	50
	46.7	0.0983	50.3	
3.0	32.6	0.1559	51.0	51
	46.7	0.1048	50.7	
5.0	32.6	0.1601	49.7	50
	46.7	0.2115	50.2	

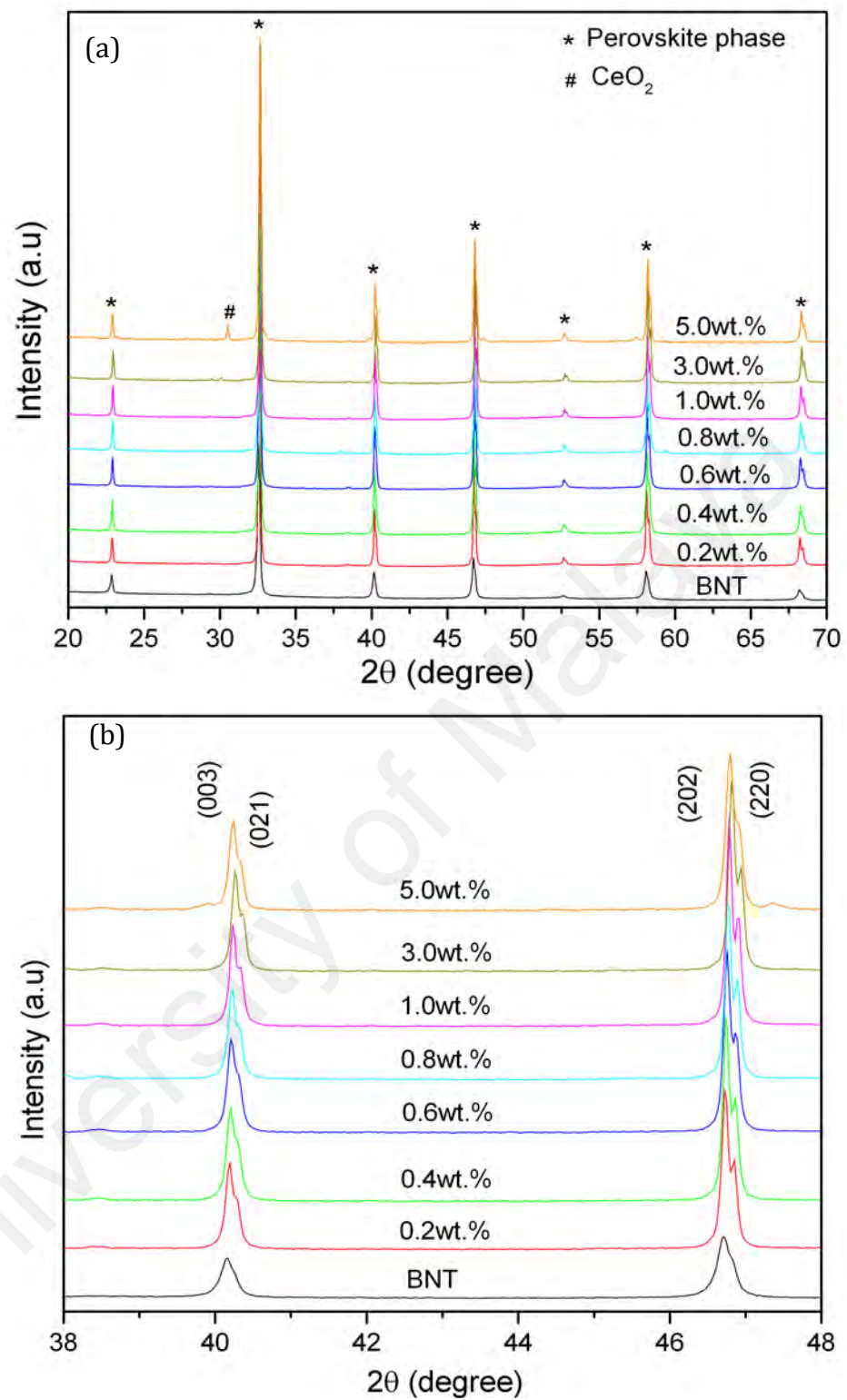


Figure 5.2: X-ray diffraction patterns of CeO_2 doped BNT (a) different amount of CeO_2 and (b) 2θ between 38° - 48° .

5.4 FESEM analysis

The micrographs of BNT- x wt.% CeO_2 ceramics sintered at 1100 °C for 6 hours are shown in Figure 5.3. From this figure, it can clearly be seen that CeO_2 in BNT causes changes in the grain size and the microstructure. Compared to that of pure BNT ceramics, the average grain size decreases from $\sim 0.5 \mu\text{m}$ (pure BNT) to $\sim 0.3 \mu\text{m}$ (0.6 wt.%). The morphologies of BNT doped with CeO_2 exhibits square and rectangular in shapes. The reason for the distinct changes is because the Ce ion can restrain the grain growth during the sintering process.

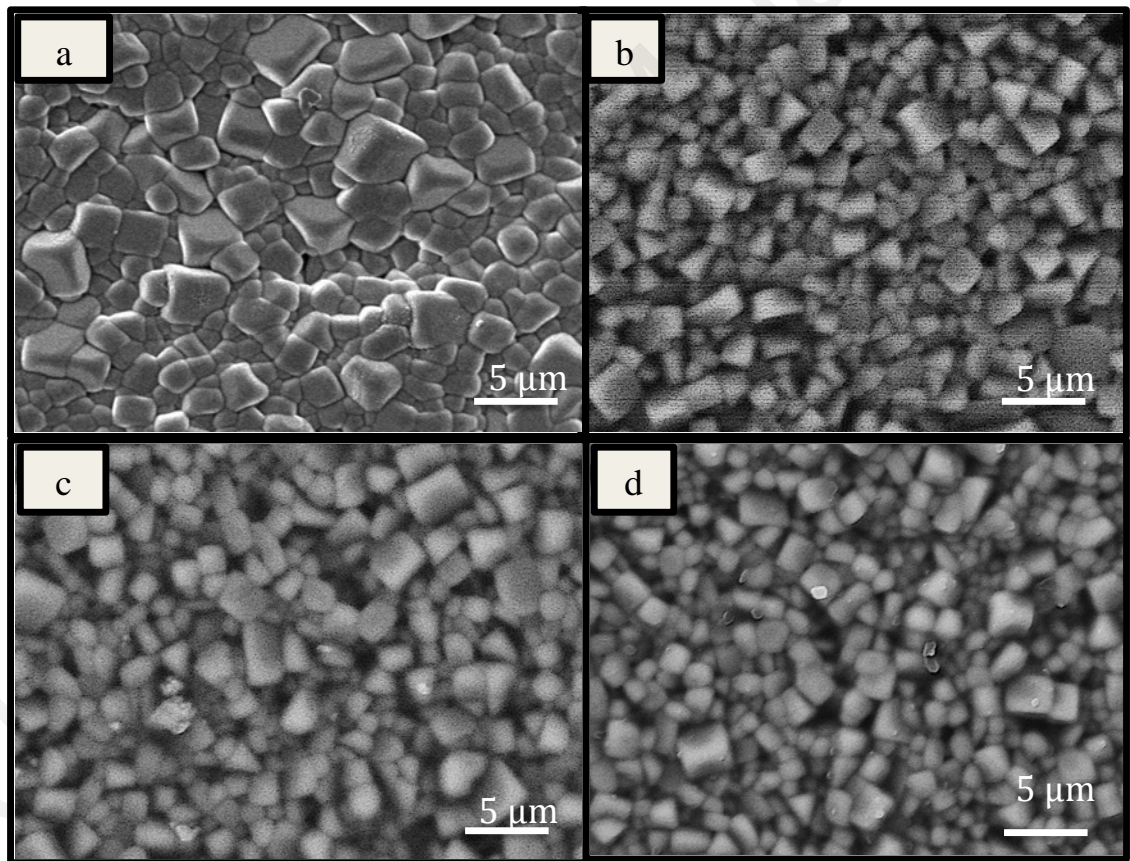


Figure 5.3: The FESEM micrograph of BNT ceramics with CeO_2 additives (a) 0.0 wt.%, (b) 0.4 wt.%, (c) 0.8 wt.% and (d) 1.0 wt.%.

5.5 Dielectric properties

The temperature dependence of dielectric constant, ϵ' and dissipation factor, $\tan \delta$ of BNT-wt.% CeO_2 at 10 kHz are shown in Figure 5.4. Two transition temperatures; depolarization temperature, T_d and maximum temperature, T_c were observed from the graph ϵ' versus T . T_d is the temperature at which the phase transition between ferroelectric (rhombohedral) to anti-ferroelectric phase (tetragonal) occurs. T_m represents the temperature at which the dielectric constant, ϵ' reaches the maximum and the phase transition between anti-ferroelectric and paraelectric phase (cubic). T_m is the maximum temperature or can be consider as Curie temperature, T_c . The doping of CeO_2 in BNT ceramics with different weight percentages do not show any significant changes in the transition temperature where the $T_d = 215^\circ\text{C}$ and $T_c = 350^\circ\text{C}$, respectively.

Figure 5.4 presents the ϵ' and $\tan \delta$ versus temperature spectrum. The ϵ' and $\tan \delta$ increase with the increased of the dopant weight percentage up to 0.6 wt.%. Further increase of CeO_2 dopant weight percentage shows a decreasing trend in the ϵ' and $\tan \delta$. It is attributed to the easy switching of the ferroelectric domain which results in the increase of ϵ' and $\tan \delta$. When the weight percentage of CeO_2 was above 0.8 %, the excess CeO_2 stayed in the boundary and formed grain boundary layer that caused reduction in ϵ' (Zhang et al., 2009)

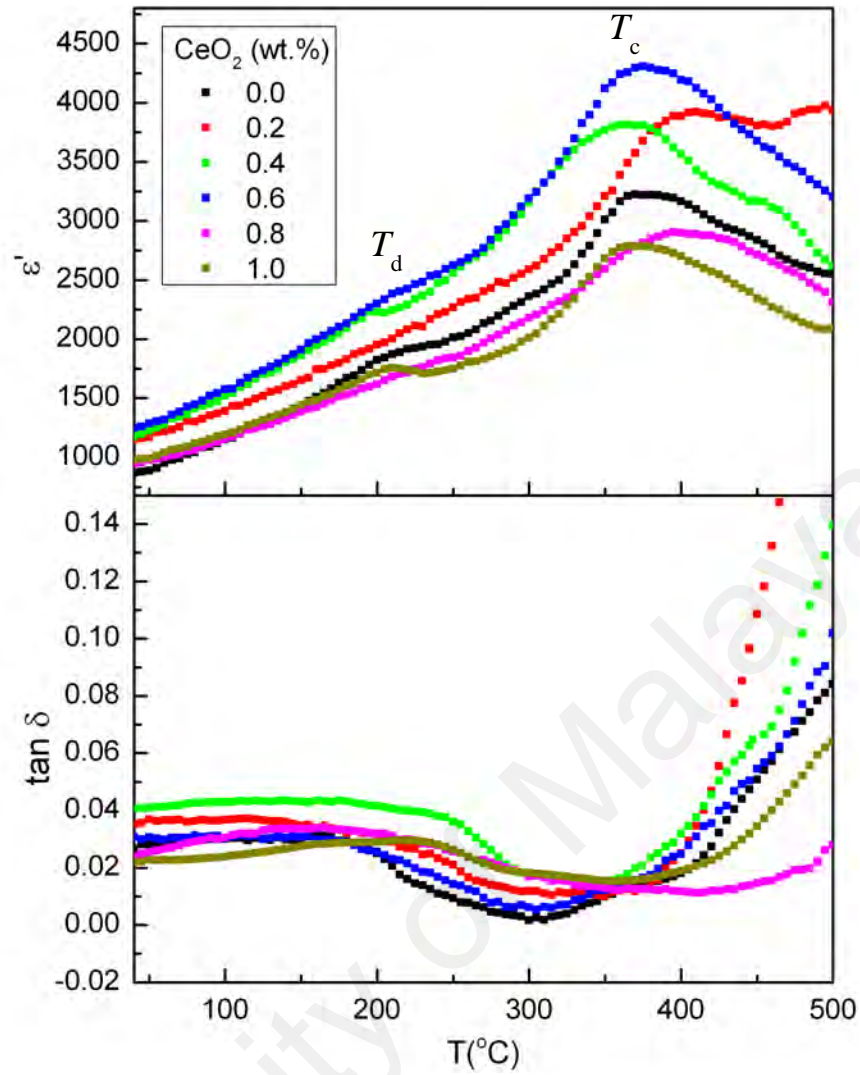


Figure 5.4: Temperature dependence of dielectric constant, ϵ' and dissipation factor, $\tan \delta$ of CeO_2 doped BNT at 10kHz.

5.6 Piezoelectric properties

Figure 5.5 shows the thickness extensional (TE) resonance peak at room temperature for the ϵ' and $\tan \delta$. The intensity of $\tan \delta$ or resonance peak increased by the increase of the CeO_2 dopant up to 0.6 wt.% then reduces after the doping percentage increased to 0.8 wt.%. Meanwhile, the TE resonance frequency, f_r (observed 3 MHz) has slightly shifted to the left and the intensity of the resonance peak decreased with the increase of CeO_2 dopant, respectively.

The mechanical coupling coefficient, k_{33} , piezoelectric constant, d_{33} and the modulus of elasticity (Young Modulus), c are measured by using Equation 4.3 to 4.5

in Chapter 4. The obtained dielectric and piezoelectric properties of CeO₂ doped BNT are shown in Figure 5.6. From the observation, 0.6 wt.% of CeO₂ shows the highest dielectric constant, ($\epsilon' = 1276$), mechanical coupling factor, ($k_{33} = 0.44$) and piezoelectric constant, ($d_{33} = 90$ pC/N). The Young Modulus, c_{33} , however decreases to 138 GPa. Excess doping of CeO₂ decrease the stiffness of the BNT piezoelectric constant. A soft doping ion like Ce ion may soften and increase the properties of piezoelectric ceramics, thus dielectric constant ϵ' and electromechanical coupling factor k_{33} are enhanced, while in the process reduce the coercive field E_c of the ceramic (Xu, 1991).

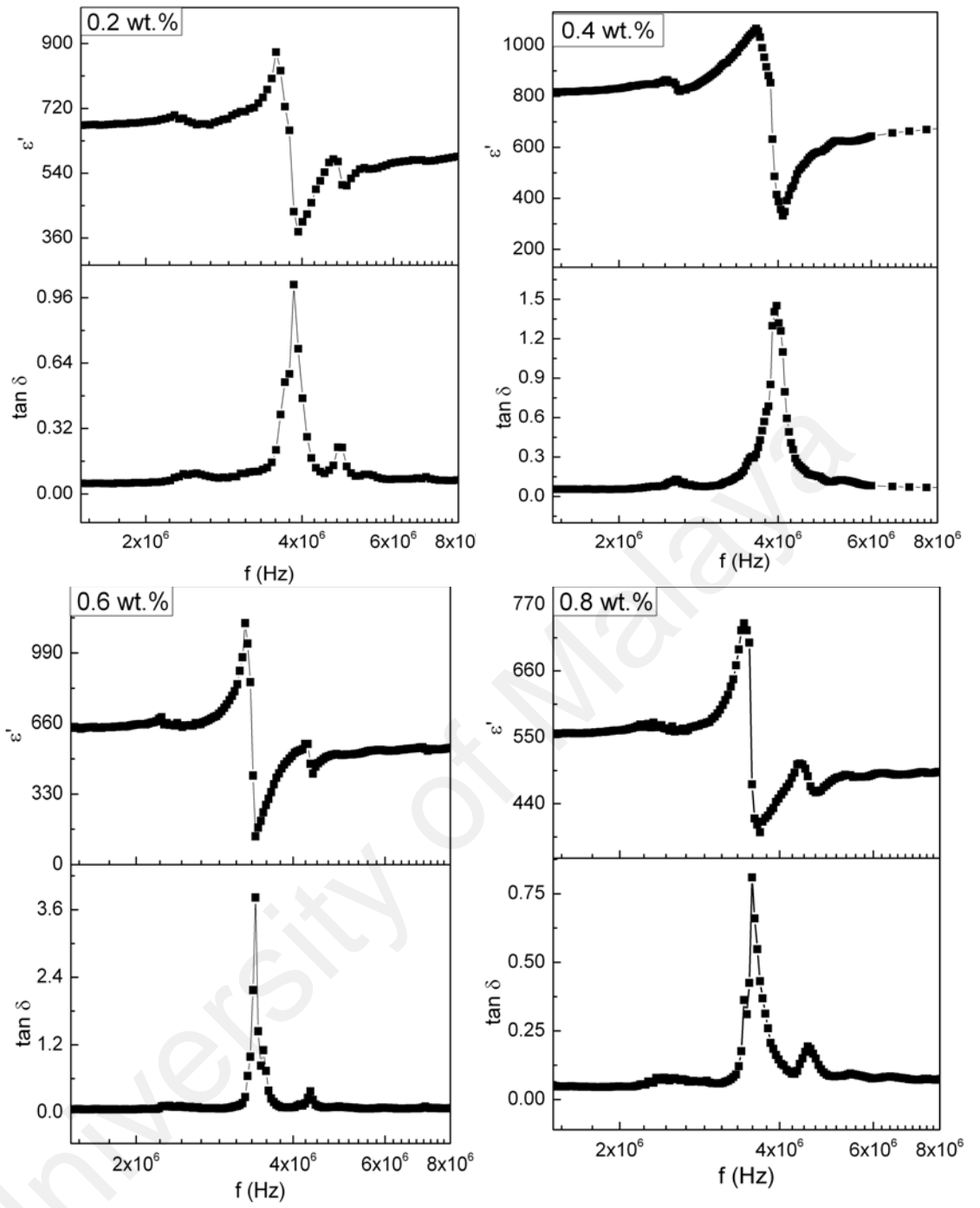


Figure 5.5: Piezoelectric resonances at various weight percentages of CeO_2 .

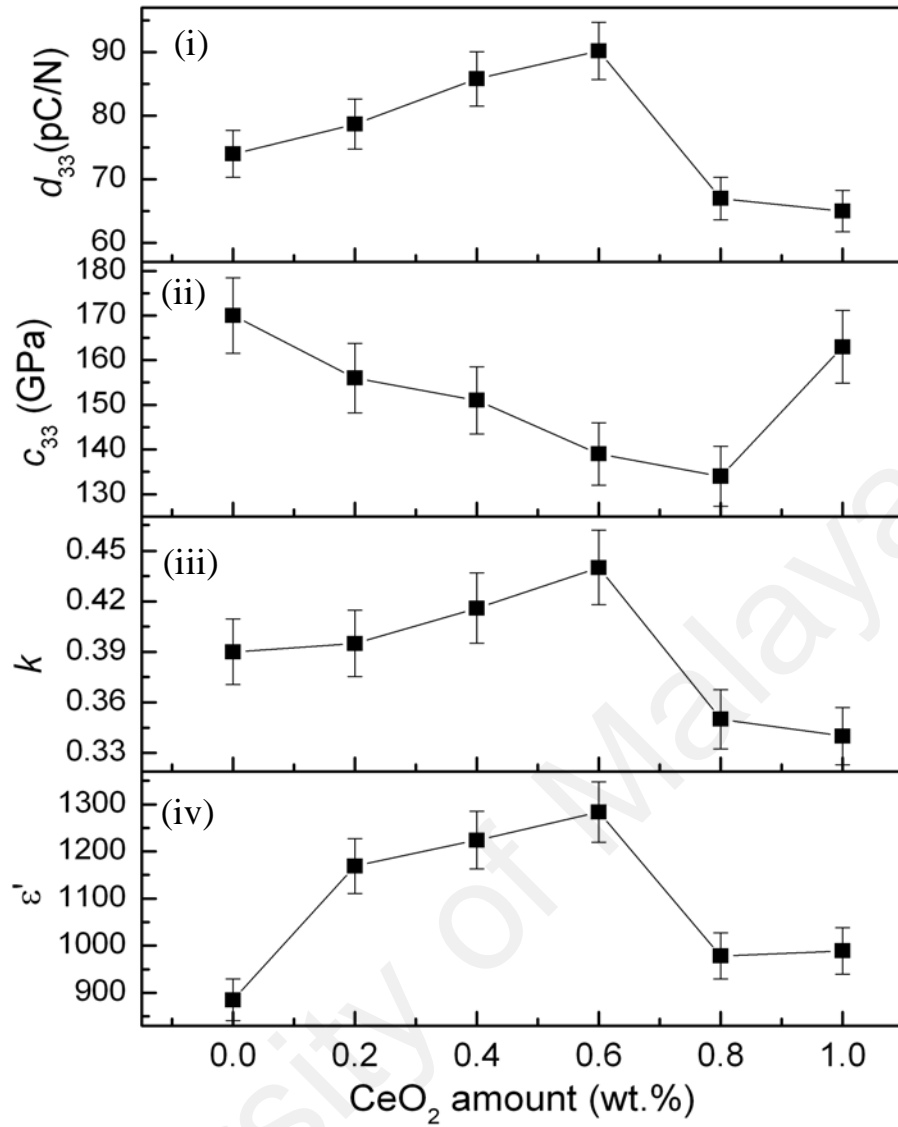


Figure 5.6: Dielectric constant, ϵ' and piezoelectric properties of CeO₂ doped BNT; (i) piezoelectric constant d_{33} , (ii) Young Modulus c_{33} and (iii) mechanical coupling factor k_p .

5.7 Ferroelectric properties

The polarization, P versus Electric field, E (P - E) hysteresis loop of the BNT - x wt. % CeO₂ ceramics at room temperature is shown in Figure 5.7. At low applied electric field, the P - E curve is almost linear. When E was increased, the hysteresis loops are emerged rapidly where the dipoles in the BNT begin to align gradually with the field, and saturation polarization can be observed. However, a fully saturated hysteresis loops were not obtained for these samples. This is probably due to the existence of oxygen vacancies and leakage in the BNT ceramics.

Figure 5.8 shows the P - E hysteresis loops of the various CeO_2 dopant weight percentages in the BNT samples at a maximum applied electric field. By doping a little amount of Ce ions, the remnant polarization, P_r shows enhancement up to 0.6 wt.%. Then P - E loops become rounded and conductive as the CeO_2 weight percentages increased to 1.0 wt.% due to the presence of excessive CeO_2 . E_c for CeO_2 doped BNT is reduced, thus lower electric field are required to pole the domains compared to that of pure BNT. The 0.6 wt. % CeO_2 doped BNT gives the highest P_r ($56 \mu\text{C}/\text{cm}^2$) and has the lowest coercive field, E_c (53 kV/cm), respectively. The poling process causes a slight change in the B-site element of the perovskite structure. The charges causes charge defect and interact strongly with domain walls, and consequently affects the ferroelectric behavior of the sample (Kontsos & Landis, 2009).

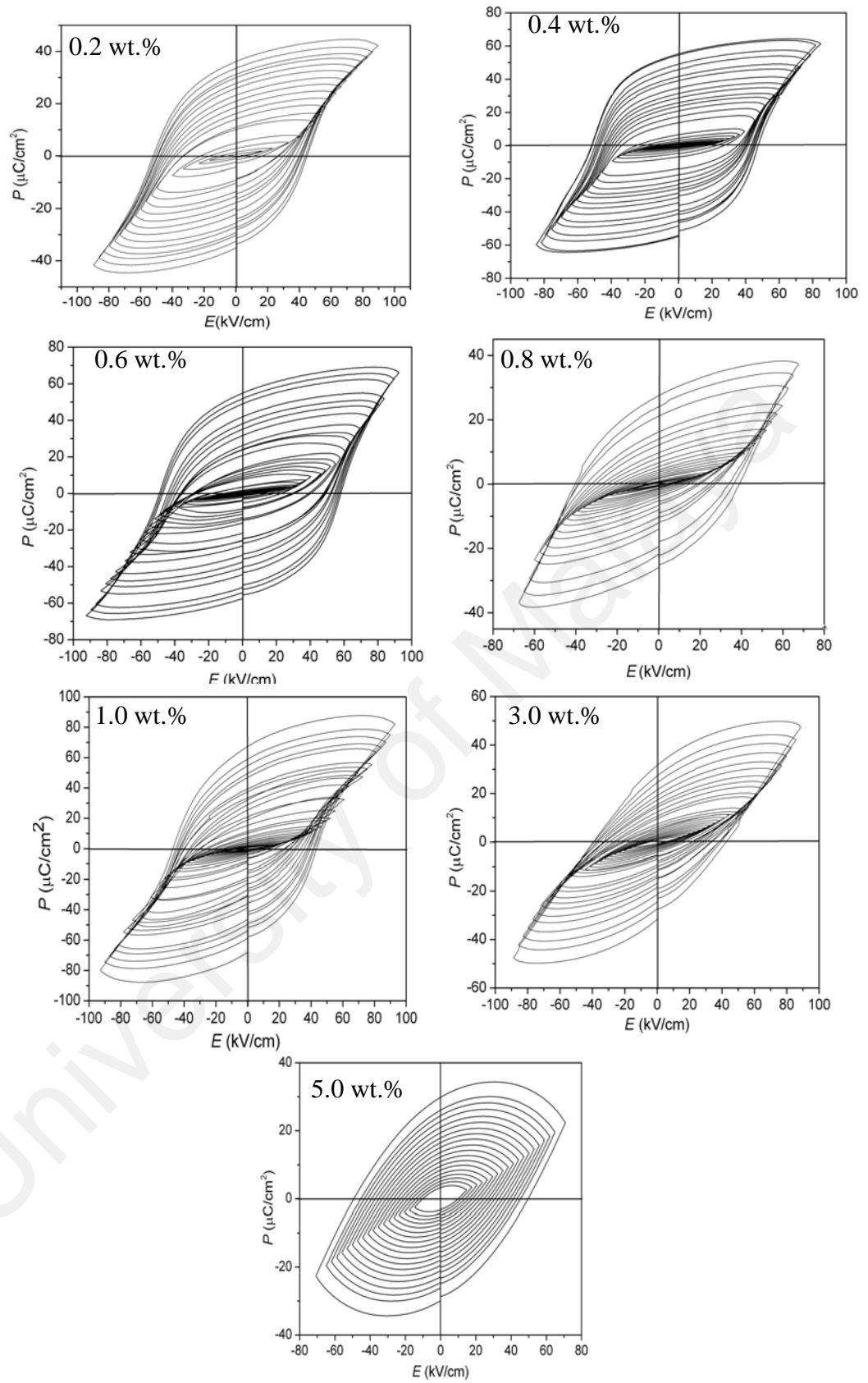


Figure 5.7: P - E hysteresis loops of BNT – x wt.% CeO_2 ceramics measured at 5 Hz with various electric fields.

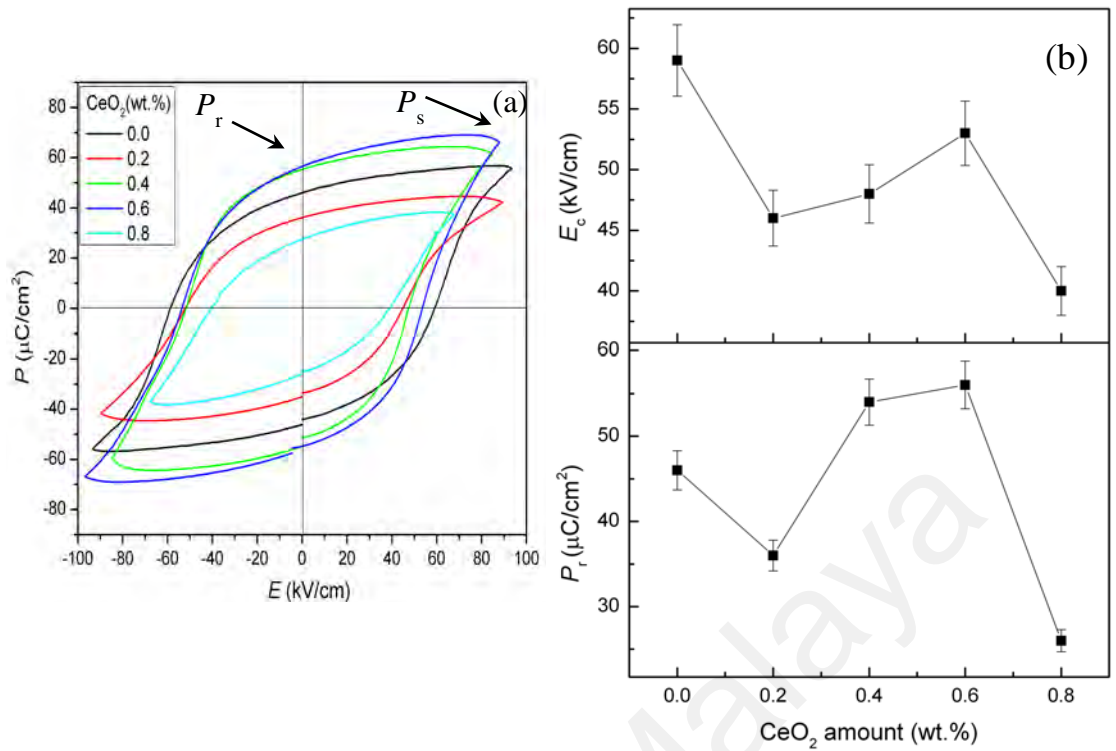


Figure 5.8: (a) P-E hysteresis loops at various weight percentages of CeO₂ and (b) P_r and E_c of the BNT ceramics as a function of CeO₂.

5.8 Pyroelectric properties

Figure 5.9(a) shows the pyroelectric results of the CeO₂ doped BNT samples. A triangular waveform temperature applied to the poled samples and such a small change of temperature produced a square waveform of pyroelectric current. The pyroelectric coefficients of CeO₂ doped BNT samples poled at 4 kV and 200 °C for 30 minutes is shown in Figure 5.9(b). By referring to the temperature dependence of dielectric constant (see Figure 5.4), the depolarization temperature of 0.2 wt.% CeO₂ is above 200 °C compared to the rest of the compositions. However, the poling process of all the compounds were done at 200 °C to be consistent. Therefore, the applied temperature during the poling process for 0.2 wt.% CeO₂ doped BNT is not optimum temperature for the effective poling. Therefore, the remnant polarization, P_r of the particular temperature is lower than the rest of the samples. The BNT-0.6 wt.% CeO₂ shows the highest pyroelectric coefficient ($650 \mu\text{C}/\text{m}^2\text{K}$). We observed the highest P_r for this sample as well (refer to Figure 5.8). In addition, as the weight

percentage of CeO_2 was increased to 1.0 wt.%, the CeO_2 doped BNT ceramics became conductive and distorted the spontaneous polarization and consequently the pyroelectric coefficient has decreased.

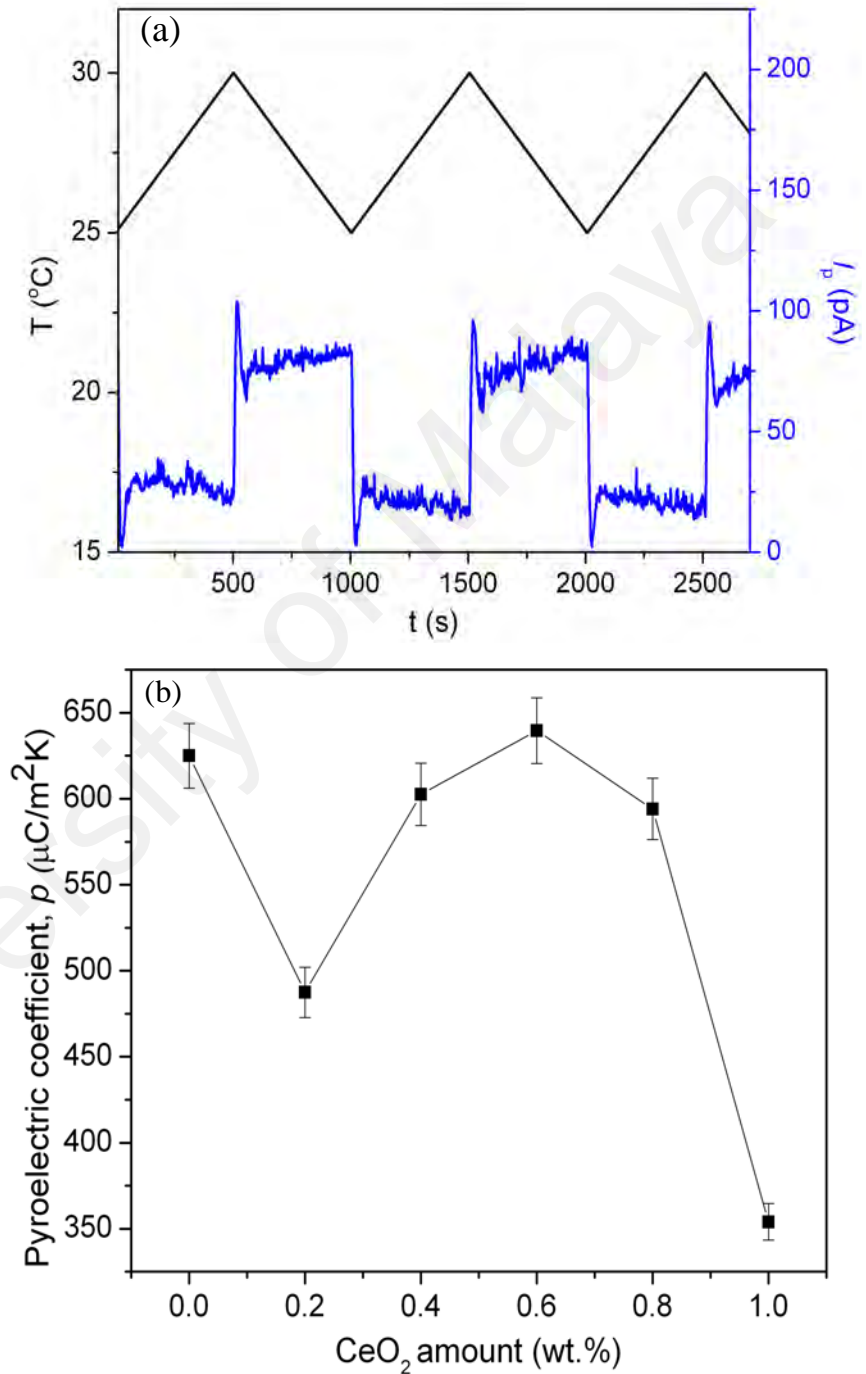


Figure 5.9: (a) The pyroelectric current of poled BNT-0.6 wt.% CeO_2 ceramic at the heating rate of 0.6 °C/min and (b) pyroelectric coefficient of the CeO_2 doped BNT ceramics.

5.9 Leakage current analysis

Figure 5.10 shows the leakage current density, J versus electric field, E (J - E) of CeO_2 doped BNT from 0.0 to 5.0 wt.%. From the observation, it is obvious that a high weight percentage of CeO_2 causes to a high leakage current and thus a higher conductivity. This is expected as CeO_2 is a conductive material. However, a small amount of CeO_2 can significantly improve the electrical properties. The average of leakage current for the sample doped with 0.0 to 1.0 wt.% of CeO_2 is about $10^{-6} - 10^{-9} \text{ A/cm}^2$ over the electric field range of $\pm 4 \text{ MV/m}$. The 0.6 wt.% doped CeO_2 shows the lowest leakage current density (10^{-9} A/cm^2) which is less leaky and thus good to be used as a dielectric material.

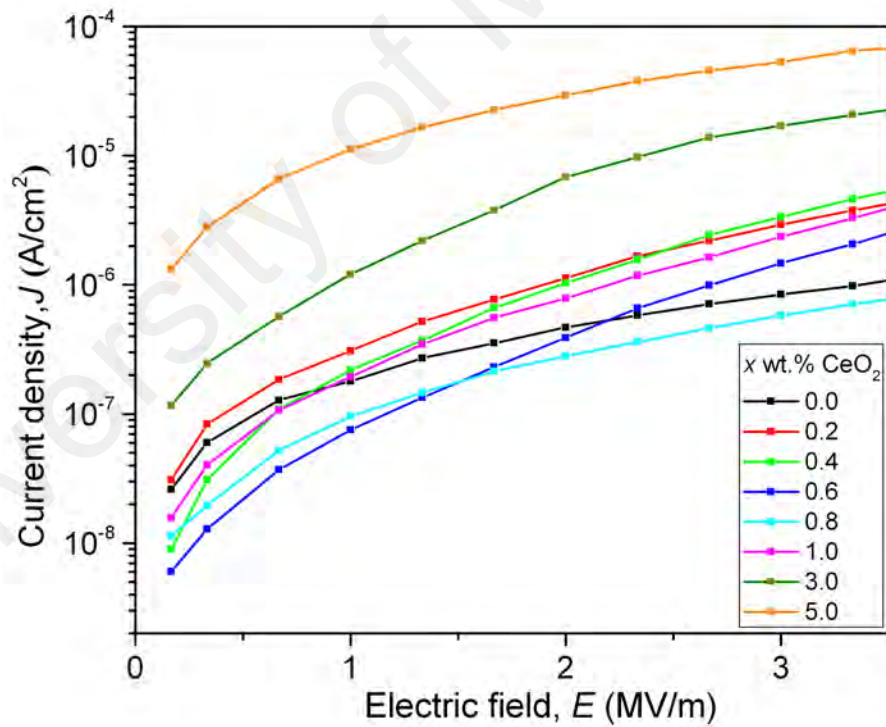


Figure 5.10: Leakage current density of BNT- x wt.% CeO_2 ceramics.

5.10 Discussion

The results in the above sections show that doping CeO_2 in BNT improved the ferro-, pyro-, piezo- and dielectric properties of the ceramic. CeO_2 acts as both donor and acceptor in the BNT ceramic during the sintering process. Ce ion possibly exists in two valence states; Ce^{4+} (ionic radius of 0.92 Å) and Ce^{3+} (ionic radius of 1.03 Å). Since Ce ions are larger, they are unable to reside in B site of BNT perovskite where originally only resided by Ti^{4+} (ionic radius of 0.68 Å). However, Ce ions can occupy the A-site of the ceramic, including A1 site (Na^+ in ionic radius of 0.97 Å) and A2 site (Bi^{3+} in ionic radius of 0.96 Å). Logically, either Ce^{3+} or Ce^{4+} occupies Bi^{3+} site in the BNT. It is known that Bi_2O_3 is volatile at high temperature during sintering, and Bi^{3+} in the BNT may form some vacancies of A-site in the lattice. The replacement of A-site by Ce^{3+} or Ce^{4+} does not cause any deformation in the BNT lattice, as there is no evident that the domain movement has been enhanced. However, Ce^{4+} ion has smaller radius and also has the same charge as that of Ti ion and may occupy the B-site (see Figure 5.11). The doping of Ce^{4+} into Ti^{4+} site in the BNT ceramics increases the space charges (i.e.: both centers of charges and hole-carriers). These space charges cause an internal field inside the grains of BNT and this field may inhibit the domain movement of the domain walls. The dislocation of Ce^{4+} atoms followed the direction of applied electric field cause defect in lattice and thus, result in higher piezoelectric and ferroelectric properties (Li et al., 2007).

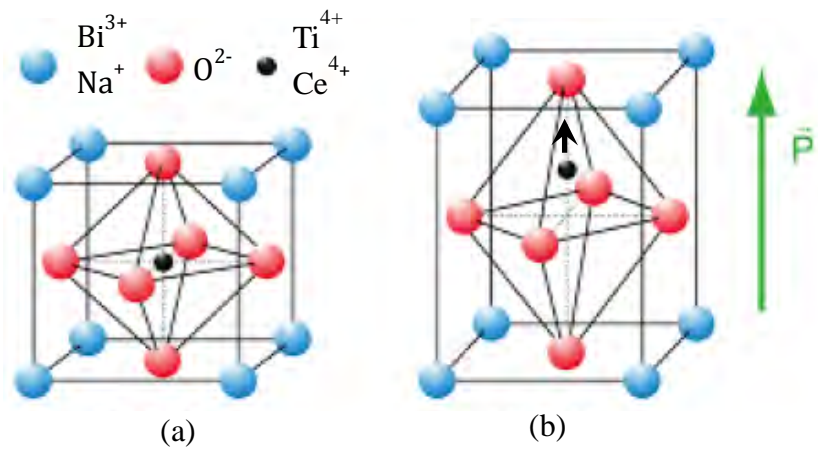


Figure 5.11: (a) The replacement of Ce^{4+} ion in the BNT perovskite structure and (b) the distortion of Ce^{4+} influence of electric field.

When the amount of CeO_2 is over 0.8 wt.%, some Ti^{4+} ions may be substituted by Ce^{4+} in the lattice of the BNT ceramic. Some of Ce ions may accumulate in the grain boundaries. The pinning effect on the domains hinder their motion and reduced the stability of the ferroelectric domains which may cause the deterioration of piezo-, pyro- and ferroelectric properties of the BNT.

The structure with a composition at the morphotropic phase boundary (MPB) is considered as a transitional structure between tetragonal and the rhombohedral phases. The lattice structure may be changed by an external field. The evolution in crystal structure from the rhombohedral phase to morphotropic phase boundary shows positive effect on the electrical properties. At the morphotropic phase boundary, the materials can be both rhombohedral and tetragonal phase. Thus, spontaneous polarization can move along any one of the 14 directions. Consequently, it is easier for the domain to move during the poling process which resulted in high piezoelectric and dielectric properties (Zhao et al., 2005).

5.11 Conclusion

The piezo-, pyro-, ferro- and dielectric properties of CeO₂ doped BNT at various weight percentages have been investigated. The pure BNT exhibits the perovskite structure in rhombohedral phase, while doping of CeO₂ has changed the structure into pure perovskite with morphotropic phase boundary of rhombohedral and tetragonal phase. The grain size of the ceramics slightly decreases after doping process. The 0.6 wt.% of CeO₂ doped BNT ceramic is the optimize dopant concentration where the BNT shows the highest piezoelectric constant d_{33} of 90 pC/N, electromechanical coupling coefficient k_{33} of 0.44, Young modulus, c_{33} of 138 GPa, remanent polarization P_r of 56 $\mu\text{C}/\text{cm}^2$ and pyroelectric coefficient p of 650 $\mu\text{C}/\text{m}^2\text{K}$, respectively.

CHAPTER 6: P(VDF-TrFE) /Na_{0.5}Bi_{0.5}TiO₃-0.6 CeO₂ NANOCOMPOSITES

6.1 Introduction

As discussed in Chapter 5, we found that the BNT-0.6 wt.% CeO₂ ceramic is the optimized compositions among the BNT doped with CeO₂ samples. Thus, in polymer/ ceramic composites, we used BNT-0.6 wt.% CeO₂ as the inclusion for the polymer matrix. In recent years, a large number of polymer ceramic electronic composites have been introduced in microelectronic application such as ultra-fast switching, magnetic field detection, piezoelectric sensor, thermal imaging tools and nonvolatile memory application. These applications required great interest towards functional materials that possess specific functionalities involving piezoelectricity, pyroelectricity and ferroelectricity (Lang, 2005; Scott, 2007).

The unique combination of ferroelectric ceramic properties such as high dielectric permittivity, large spontaneous polarization and high electromechanical coupling factor, high flexibility and low density of polymer component promises the outstanding electro-active properties and the mechanical properties of composite. Many research work has been published on the ceramic-polymer composites where the functional properties of the polymer matrix was enhanced by the ferroelectric ceramic inclusions such as lead titanate (PT), lead titanate-bismuth ferrite (PT-BF), lead zirconate titanate (PZT), lead magnesium niobate (PMN-PT), BaTiO₂, and BNT embedded in the ferroelectric polymer matrix of poly(vinylidene fluoride) (PVDF) and its copolymer P(VDF-TrFE) (Furukawa et al., 1979; Han et al. (1990); Mahdi et al., 2015; Ploss et al., 2001; Ploss et al., 2000a; Ploss et al., 2000b).

BNT-0.6 wt.% CeO₂ embedded in a copolymer P(VDF-TrFE) to form a 0-3 matrix composite. The P(VDF-TrFE) copolymer is used as a polymer matrix because it has high voltage sensitivity and easily form a polar β phase conformation without mechanical stretching or treatment to the sample. Even though, there are substantial

reports on the ferroelectric and non-ferroelectric ceramic as inclusion in the composite. BNT-0.6 CeO₂ as an inclusion with the copolymer was not reported previously. The structure and electrical properties of P(VDF-TrFE) /BNT-0.6 CeO₂ composite were thoroughly investigated and reported in this chapter.

6.2 XRD analysis

Figure 6.1(a) shows the XRD pattern of the P(VDF-TrFE) /BNT-0.6 CeO₂ composite thin film with various volume fraction. The composite films were annealed at 100 °C to form a high crystalline structured film. The annealing temperature was in between the Curie temperature, T_c (90 °C) and melting temperature (130 °C) of the copolymer (Furukawa, 1997). The peak at $2\theta = 19.91^\circ$ is the characteristic peak of the crystalline β -phase or known as Form I of P(VDF-TrFE). The P(VDF-TrFE) peak was observed at (110/200) orientation planes. The unit cell in the β -phase of P(VDF-TrFE) is orthorhombic, with each chain aligned and packed with CF₂ groups parallel to the b-axis and possesses a large spontaneous polarization P_s (Furukawa, 1997; Tashiro, 1995).

The XRD pattern of BNT-0.6 CeO₂ indicates the perovskite structure with CeO₂ peak at $2\theta = 30.33^\circ$ which correspond to the (110) plane. The peaks at the range 38-42° and 45- 48° are corresponding to the (003/021) and (202/220) planes of rhombohedral-tetragonal morphotropic phase boundary of CeO₂ doped BNT. The intensity of the (110/200) plane of P(VDF-TrFE) decreases with the increase in volume fraction (Figure 6.1(b)). In contrast, the intensities of the BNT-0.6 CeO₂ peaks increase with the increase in the volume fraction of the ceramic.

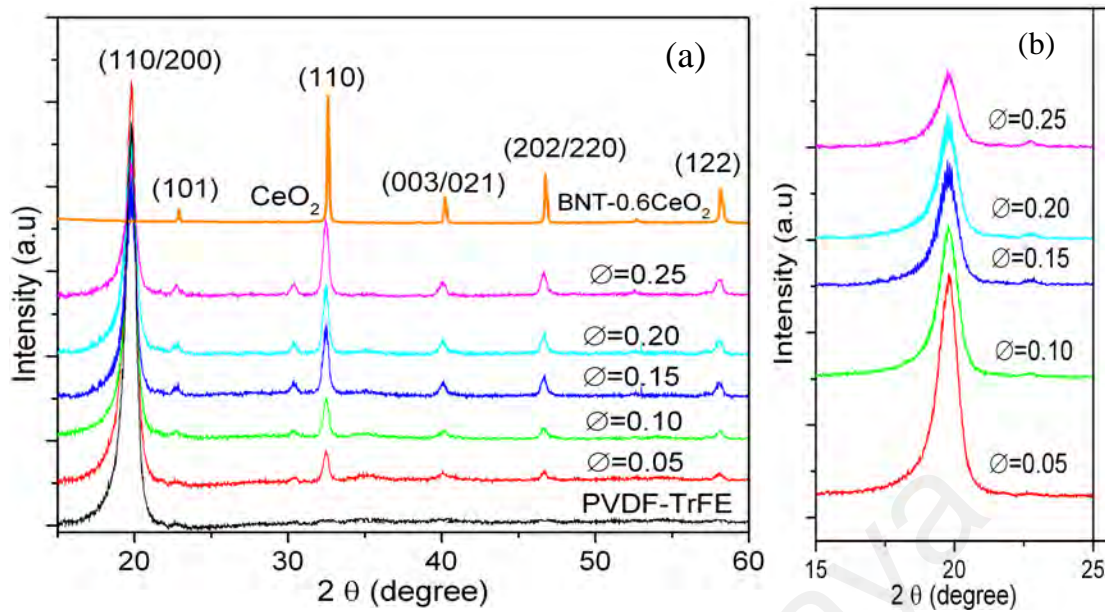


Figure 6.1: XRD pattern of (a) P(VDF-TrFE), BNT-0.6 CeO₂ and P(VDF-TrFE)/BNT-0.6 CeO₂ composite, (b) peak intensity of P(VDF-TrFE).

6.3 FTIR analysis

The crystallinity of P(VDF-TrFE) /BNT-0.6 CeO₂ film can be further confirmed by transmission IR spectra as shown in Figure 6.2. The most infrared-active vibrations for copolymer are concentrated at narrow range of 400-1500 cm⁻¹. This is due to the large mass of the fluorine atoms (Reynolds et al., 1989). The characteristic vibration spectra of β -phase P(VDF-TrFE) was observed at the four intense bands of 510, 850, 1288 and 1400 cm⁻¹. The bands at 510 and 1400 cm⁻¹ are referred to CF₂ bending mode within all trans (*TTTT*) segment along the chain and CH₂ wagging vibration, respectively. The bands at 850, 876 and 1288 cm⁻¹ are assigned to CF₂ stretching mode (Kobayashi et al., 1975; Reynolds et al., 1989), while the band at 1174 cm⁻¹ assigned to the C-C bond (Gregorio & Borges, 2008). The presence of β -phase in the infrared spectra denotes the most important characteristic that is responsible for the piezoelectric and pyroelectric activities in P(VDF-TrFE). The incorporation of BNT-0.6 CeO₂ in P(VDF-TrFE) with different volume fractions do not show any significant changes in the phase transition. However, the intense bands

of P(VDF-TrFE) decreases with the increase in volume fractions of ceramic inclusions.

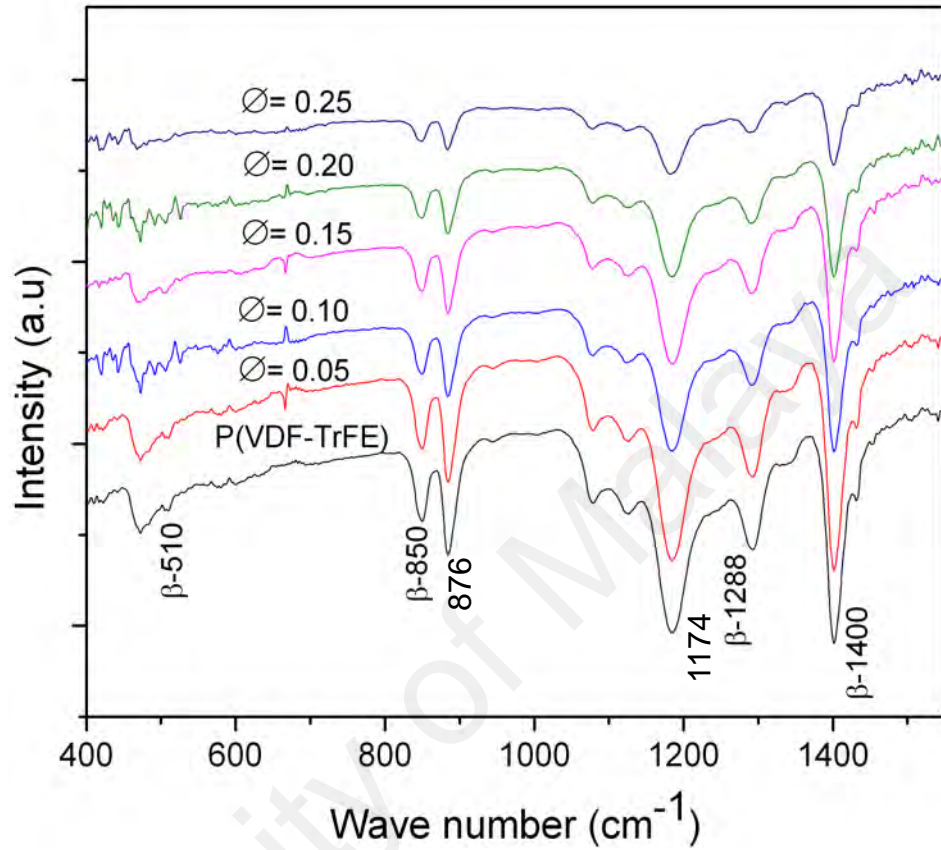


Figure 6.2: FTIR spectra of P(VDF-TrFE) and composite thin films.

6.4 FESEM analysis

Figure 6.3 shows the surface morphology of P(VDF-TrFE) and P(VDF-TrFE)/BNT-0.6 CeO₂ composite thin film at 10 μm . The morphology of P(VDF-TrFE) at higher magnification is shown in Figure 6.3. A lamellar structure with rod-like crystal grain is observed in the P(VDF-TrFE) film with an average crystalline size of 100 nm. The micrograph of the composites with less than 0.20 volume fraction show an uniform dispersed samples without any formation of large agglomerations of ceramic powder. However, when the volume fractions of ceramic increases to 0.25, the inter-particle distance decreases and the agglomeration of ceramic in a form of cluster can be observed (see Figure 6.3($\phi = 0.25$)). The agglomeration of

nanoparticles are unavoidable due to the higher electrostatic force. When the particle size is small, the surface area of the particle is large. The interaction between the nanoparticles is strong, which results in continuous percolation of particles throughout the composite (Dang et al., 2002; McLachlan et al., 1990). When a high viscous of P(VDF-TrFE) with low volume fractions of ceramic were used; the composite tends to be a mixture of 0-3 composite connectivity as shown in Figure 6.4(a). However, when the volume fractions of the ceramic are increased, the particles will be in contact with one another and start to agglomerate to form a mixture of 1-3 composite connectivity (see Figure 6.4(b)). The agglomeration of the particles leads to aggregation along the direction through the thickness, which forms a leakage current path, which can affect the electrical properties of the thin film nanocomposite.

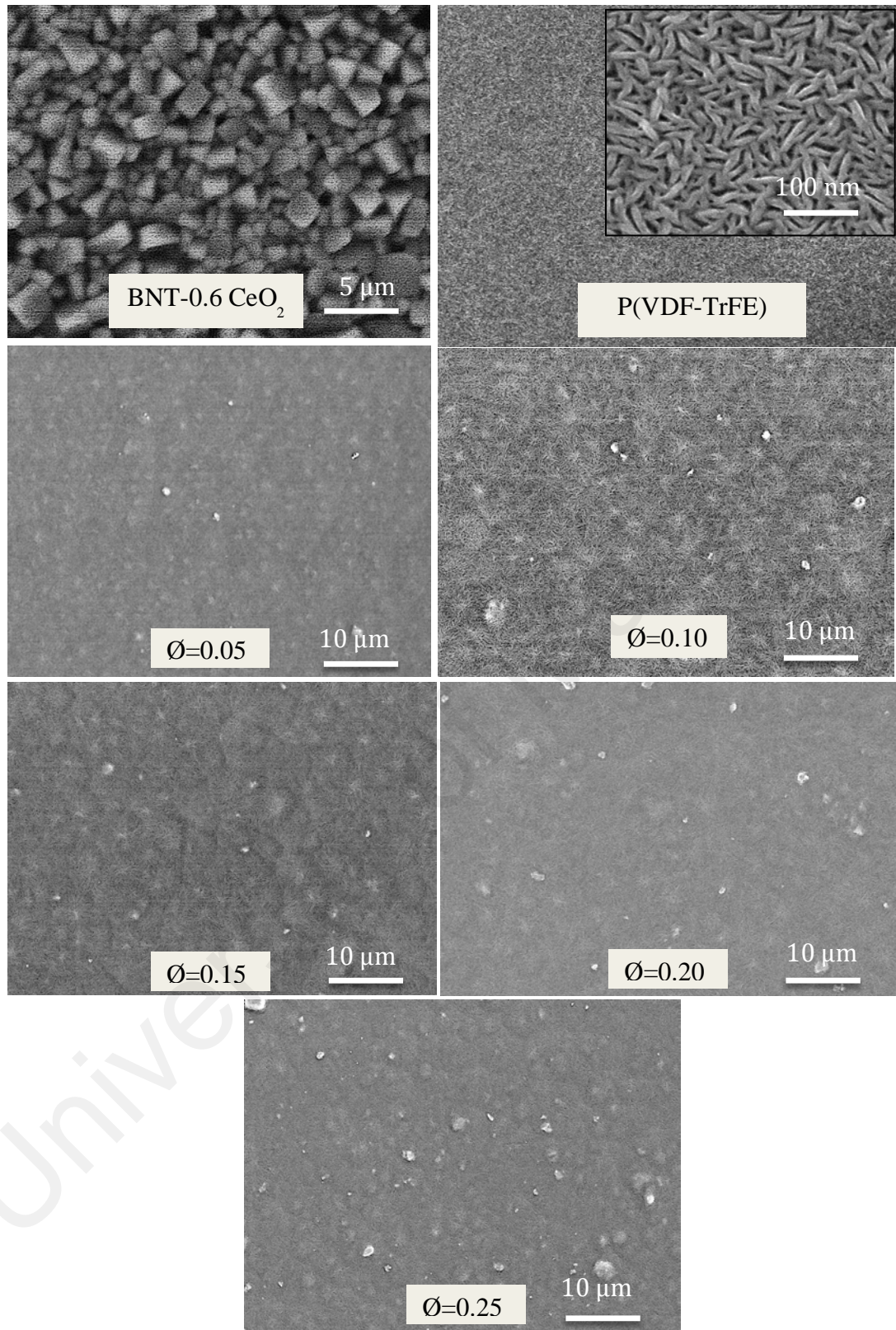


Figure 6.3: FESEM microstructure of BNT-0.6 CeO₂ ceramics, pure P(VDF-TrFE) and P(VDF-TrFE) /BNT-0.6 CeO₂ with various values of volume fractions, Ø.

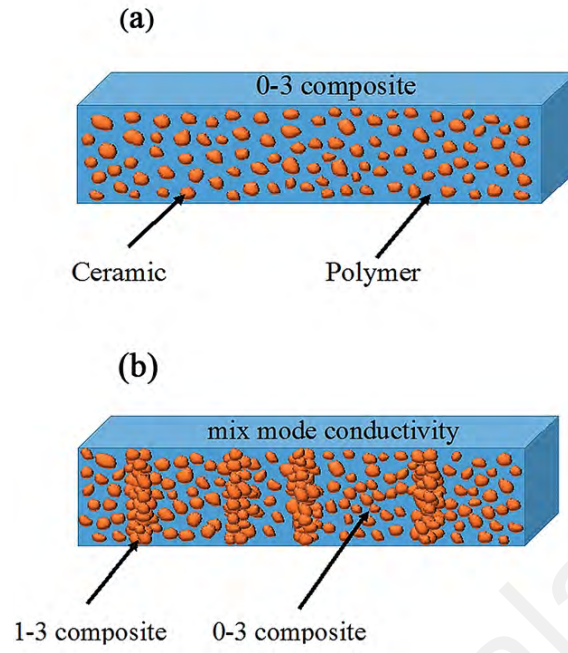


Figure 6.4: A schematic diagram of P(VDF-TrFE) /BNT-0.6 CeO₂ composite of (a) 0-3 and (b) 1-3 connectivity.

6.5 Dielectric properties

The frequency dependence of the complex permittivity of the P(VDF-TrFE) /BNT-0.6 CeO₂ nanocomposite with various volume fractions measured at room temperature are shown in Figure 6.5. At low frequency, both ϵ' and ϵ'' increase with increasing volume fraction of the ceramic due to the space charge effect. The inclusion (BNT-0.6 CeO₂) is generally very conductive and when it mixed with polymer, it increases the conductivity of the film. The relationship between ϵ' and conductivity can be expressed by the following equation, which is adapted from complex dielectric permittivity, $\epsilon^* = \epsilon' - i\epsilon''$ and complex conductivity, $\sigma^* = \sigma' + i\sigma''$:

$$\sigma^* = i \omega \epsilon^* \quad (6.1)$$

$$\epsilon' = \frac{\sigma'}{\omega} \quad (6.2)$$

$$\epsilon'' = \frac{\sigma''}{\omega} \quad (6.3)$$

where, ω is the angular frequency, $\omega = 2\pi f$ (where f is the frequency). The high conductivity of the polymer composite film is caused by the space charges that are trapped in between the interfaces of polymer matrix and inclusions. When the ceramic volume fractions increases, both the dielectric constant and dielectric loss of the nanocomposite thin film increases. The interfacial polarization exists in heterogeneous dielectrics structure, which is induced by the mobile charge carriers. The charge trapped at the interfaces cause large-scale field distortions compared to other types of polarization such as atomic, electronic or dipolar polarization, which are only produced by the displacement or orientation of bound charge carriers. The theory of Debye-type relaxation process has been employed to explain the phenomenon (Tsangaris et al., 1996).

$$\varepsilon^* = \varepsilon'_\infty + \frac{\varepsilon'_s - \varepsilon'_\infty}{1 + i\omega\tau} - i \frac{\sigma}{\omega} \quad (6.4)$$

where ε'_s is the static permittivity and ε'_∞ is the instantaneous permittivity where the values of ε' at $\omega \rightarrow 0$ and $\omega \rightarrow \infty$, respectively. ω is the angular frequency, τ is the relaxation time and σ is the conductivity. The values of ε'_s , ε'_∞ and σ depend on the conductivities and volume fraction of the constituents in the composite. In contrast, as the frequency increases, the ε' decreases and ε'' increases. This is likely due to the lower contributions from dipolar polarization effects and electrical conduction at these high frequencies (Lu et al., 2008) and could also be caused by the β effect in the copolymer that arise from the micro-Brownian motion of non-crystalline chain segment (Mahdi & Majid, 2016).

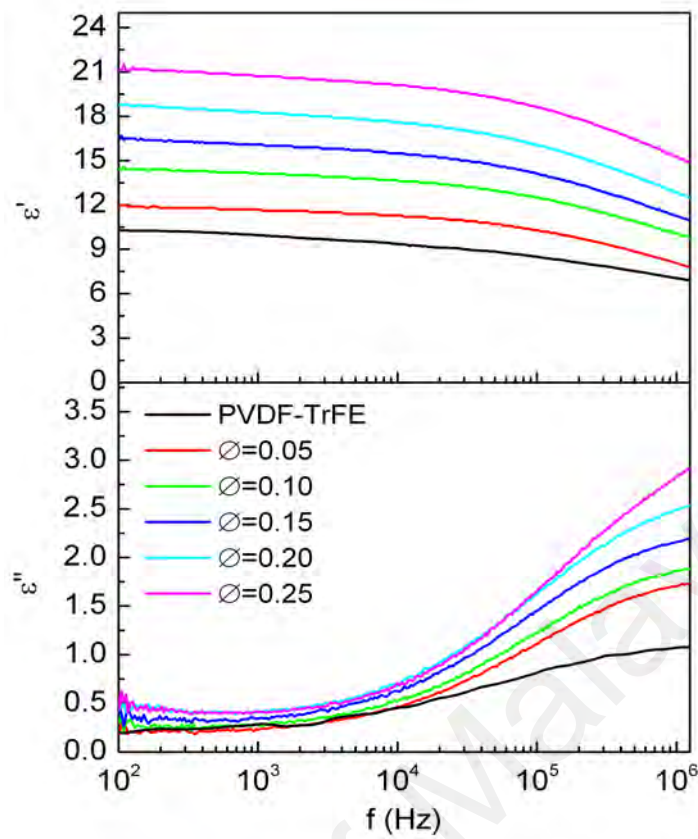


Figure 6.5: Dielectric spectra of P(VDF-TrFE)/BNT-0.6 CeO₂ composite films with various volume fractions as measured at room temperature.

In this work, the composite thin film can be modeled by two-phase dispersion system that consist of polymer matrix (P(VDF-TrFE)) in phase 1 and ceramic fillers (BNT-0.6 CeO₂) in phase 2. The effective dielectric constants in the polymer nanocomposite thin film can be determined and understood from a various theoretical models such as Furukawa, Clausius-Mossotti, Maxwell and the effective medium theory (EMT), which is strongly influenced by the size, shape and volume fraction of the inclusion.

Figure 6.6 shows the observed room temperature dielectric constants of the P(VDF-TrFE) /BNT-0.6 CeO₂ composite with various volume fraction of BNT-0.6 CeO₂ measured at 1 kHz and fitted with various theoretical models. The theoretical model derived by Furukawa (shown in Equation 6.5) years ago was employed to

predict the effective dielectric constant. The Furukawa model states that (Furukawa et al., 1976):

$$\varepsilon = \frac{1+2\phi}{1-\phi} \varepsilon_1 \quad (6.5)$$

where ε_1 and ϕ refer to the dielectric constant of the polymer matrix and volume fraction of the ceramic inclusions, respectively. This model considers simple two phases system of 0-3 composites. The inclusions are assumed to be spherical and there is no interface effect in the composite. The value of ε_2 is assumed to be larger than ε_1 and ϕ is smaller than 1. However, the predicted effective dielectric constant from this model deviates from the experimental data for all the volume fractions, as the condition of ceramic morphology has not been taken into consideration in this model.

Another simple explicit formula for binary 0-3 composite was developed by Clausius-Mossotti (Furukawa, 1997):

$$\varepsilon = \varepsilon_1 \left(1 + 3\phi \frac{\varepsilon_2 - \varepsilon_1}{\varepsilon_2 + 2\varepsilon_1} \right) \quad (6.6)$$

where ε_2 is the dielectric constant of the ceramic inclusion. However, the predicted values from this model also seem to deviate from the observed experimental data when the volume fractions of the inclusions increase. This may be due to the formation of aggregation as the volume fraction of the inclusion increases; as a result the composite is categorized as 1-3 composite.

Another theoretical model used in this study was derived by Maxwell through the following equation (Thomas et al., 2013):

$$\varepsilon = \frac{\varepsilon_1(1-\phi)\left(\frac{2}{3} + \frac{\varepsilon_2}{3\varepsilon_1}\right) + \phi\varepsilon_2}{(1-\phi)\left(\frac{2}{3} + \frac{\varepsilon_2}{3\varepsilon_1}\right) + \phi} \quad (6.7)$$

This model considers the dielectric properties of two phases dielectric mixture comprising spherical inclusions with a high dielectric constant dispersed in a low dielectric constant of polymer matrix. The predicted effective dielectric constant from this model is found to be very close to the experimental data. This is probably because of high dielectric constant of inclusions and low dielectric constant of polymer matrix in the composite samples has been considered in deriving the model.

The effective medium theory (EMT) model considers the morphology of the inclusions. The EMT model states that (Rao et al., 2000):

$$\varepsilon = \left(1 + \frac{\phi(\varepsilon_2 - \varepsilon_1)}{\varepsilon_1 + n(1-\phi)(\varepsilon_2 - \varepsilon_1)}\right) \varepsilon_1 \quad (6.8)$$

where n refer to the shape parameter of the ceramic inclusions. The small value of n indicates the morphology of filler particles is near to spherical shape, while a high value of n indicates largely non-spherical shaped particles. The experimental results were found to be well fitted with the EMT model with $n=5.5$ for the whole range of ceramic volume fractions. This EMT model with a moderate fitting parameter n gives the best fit and it is consistent with the morphology of ceramic inclusions, which show square and rectangular shapes in the FESEM result (see Figure 6.3(a)).

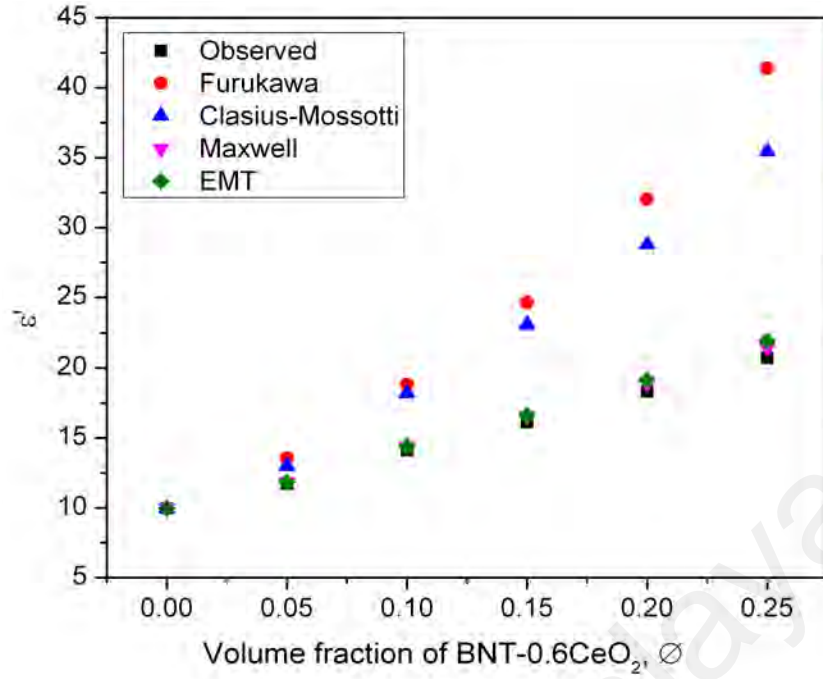


Figure 6.6: Various models of the effective dielectric constant as a function of volume fractions of BNT-0.6 CeO₂, ϕ .

In general, amorphous polymer has two relaxation processes associated with segmental mode (β -relaxation is observed from 10 Hz to 1 MHz at temperature of 25 to 140 °C) and local mode motion (δ -relaxation is observed at above 1 MHz). Some polymers having asymmetry along the chain direction that exhibit an additional relaxation called a normal mode (α -relaxation is observed at ~10 Hz) due to fluctuation of end-to-end dipole moment (Baur & Stockmayer, 1965). Semicrystalline polymer exhibits two relaxation (α - and β - relaxation) processes near 1 Hz to 1 MHz at room temperature and exhibit relaxation due to crystalline motion (Baur & Stockmayer, 1965; Furukawa, 1989). Relaxation spectra can be analyzed in order to provide information on the structure as well as the molecular interaction.

The crystalline relaxation process for the frequency dependence of ϵ' and ϵ'' can be employed from the Havriliak-Negami (HN) function (Furukawa et al., 2004).

$$\epsilon = \epsilon_{\infty} + \frac{\Delta\epsilon}{(1 + (i\omega\tau)^{\beta})^{\alpha}} \quad (6.9)$$

where ϵ_{∞} is the instantaneous permittivity, $\Delta\epsilon$ is the dielectric strength, τ is the relaxation time, α and β are parameters describing a distribution of relaxation time and ω is the angular frequency. The HN function is a combination of the Cole-Cole function ($\beta=1, \alpha \leq 1$) and the Davidson-Cole function ($\alpha=1, \beta \leq 1$). Figure 6.7 shows the observed and fitted spectra of ϵ' and ϵ'' of the unpoled P(VDF-TrFE)/BNT-0.6CeO₂ at various volume fractions. The β -phase relaxation of copolymer is observed from 1 kHz to 1 MHz at room temperature. The intensity of the ϵ' and ϵ'' for copolymer and composite increases and shifts to a higher frequency with the increase in temperature from 25 °C to 120 °C (step size at every 10 °C). When the temperature increases, the β -phase relaxation seems to move to a higher frequency >1 MHz. The β -phase relaxation is reduced as the volume fraction of ceramic inclusions was increased because of the distraction of the additional ceramic inclusions.

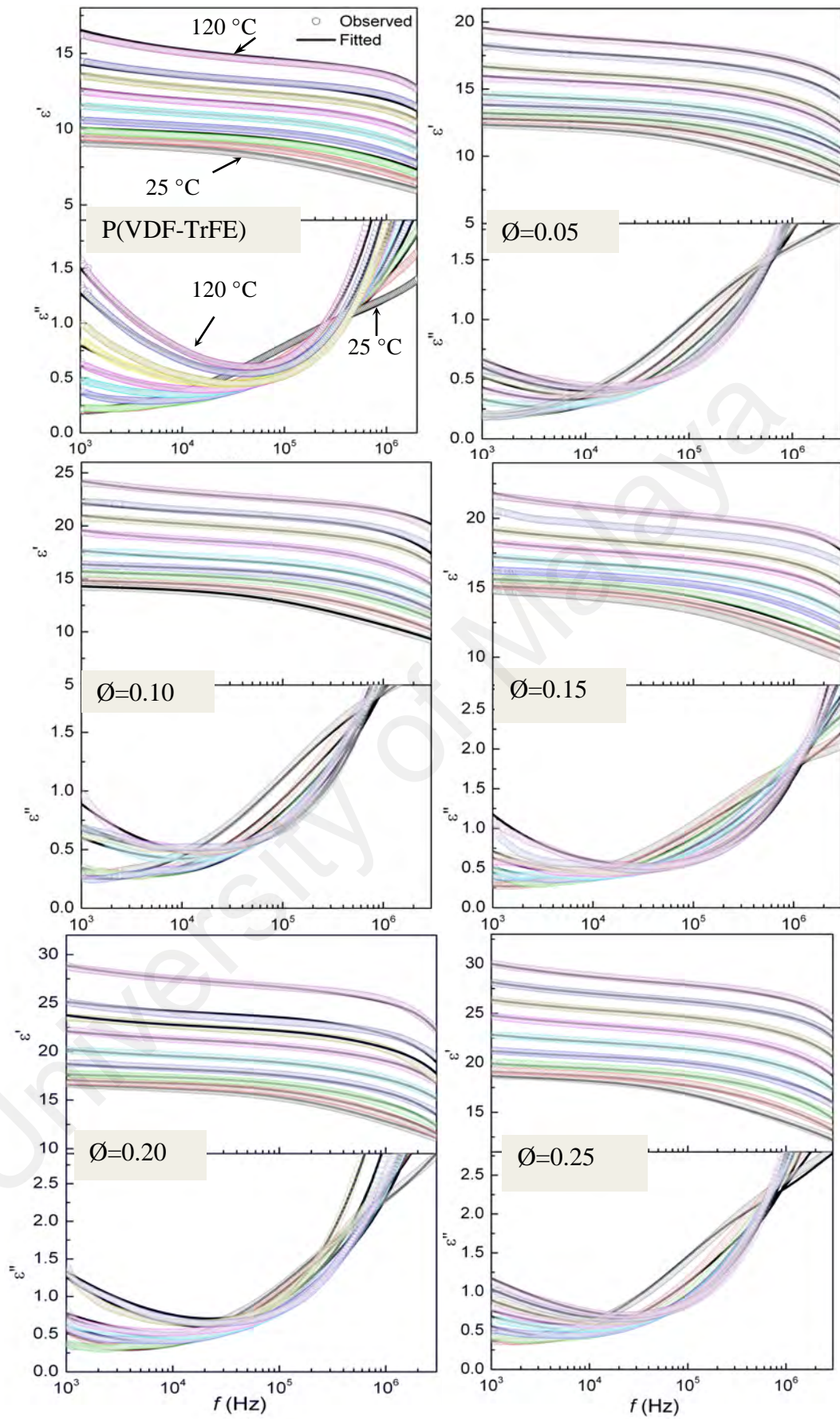


Figure 6.7: Observed (circles) and fitted (solid line) dielectric spectra of P(VDF-TrFE) and P(VDF-TrFE) /BNT-0.6 CeO₂ at 25 °C to 120 °C.

6.6 Ferroelectric properties

The ferroelectric behavior of P(VDF-TrFE) and P(VDF-TrFE) /BNT-0.6 CeO₂ thin film composites at room temperature using a frequency of 100 Hz was studied through the *P-E* hysteresis measurement as shown in Figure 6.8(a). The BNT-0.6 CeO₂ ceramics exhibited a remanent polarization, P_r of 560 mC/m² and a coercive field, E_c of 5 MV/m, whereas P(VDF-TrFE) exhibited $P_r = 80$ mC/m² with an $E_c = 76$ MV/m. Figure 6.8(b) shows that by incorporating BNT-0.6 CeO₂ ceramic as an inclusion has enhanced the remanent polarization and simultaneously reduced the coercive field in the composite system. When the volume fraction increased from 0 to 0.2, the remanent polarization has reached 166 mC/m² and coercive field has been reduced from 76 MV/m to 55 MV/m compared with that of pure P(VDF-TrFE). However, adding more BNT-0.6 CeO₂ to the composite has reduced the remanent polarization further to 79 mC/m².

Enhancing ferroelectricity by adding inclusion of high conductivity will strongly reduce the ferroelectric polarization. This is due to some of the polarization dipoles were neutralized by the additional space charges (Gan & Majid, 2015). The enhancement of pyroelectric and ferroelectric properties in P(VDF-TrFE) are governed by the conductivity in the series model. In the context of the dispersion 0-3 composite systems, the increment of volume fraction of ceramic inclusion leads to aggregation along the direction of thickness to form a similar structure to a parallel model (1-3 composite) that contributed to high leakage current and ultimately to breakdown of the sample. The inclusion of BNT-0.6 CeO₂ increased to $\phi = 0.25$ has obscured the pyroelectric and ferroelectric effect in the polymer phase by the direct current conduction in the parallel model. The current flow from one side of ceramic inclusion to the other side of polymer resulted in a continuous rise of electric displacement with time. Thus, the poling process in the polymer phase was obscured

by the direct current in the ceramic phase. The internal fields, E and the electric displacements, D in the parallel model yields as:

$$E = E_1 = E_2 \quad (6.10)$$

$$D = (1 - \phi)D_1 + \phi D_2 \quad (6.11)$$

where subscript 1 and 2 refer to the phase 1 (polymer) and phase 2 (ceramic), respectively. When the electric field was applied during the polling process, the presence of the BNT-0.6 CeO₂ nanoparticles in the ferroelectric polymer matrix of P(VDF-TrFE) formed space charge layers at the interface between the inclusions and the polymer matrix in the composite. The Maxwell-Wagner's model considers the conductivity of the inclusion of the composite thin film. The mechanism of this model explains that the space charge layers at the interface resulted in an increase of the bound charges on the electrodes in phase with the applied electric field, which give rise to an increase in the conductivity and facilitate the poling mechanism in the composite thin film (Furukawa & Fukada, 1977; Furukawa et al., 1979). Consequently, the space charges in the P(VDF-TrFE) /BNT-0.6 CeO₂ nanocomposite can drift and accumulate at the boundary of the inclusions and the polymer matrix interfaces at the faster rate in order to compensate for the discontinuity of the electric displacement at the location. Without the accumulated space charges at the boundary and also known as interfacial charges, the dipoles may revert to a random orientation because of the presence of depolarizing fields. However, with the interfacial polarization, the local electric field has increased significantly in the inclusion phase and the poling field of the composite thin film decreases. Thus, the poling efficiency of the system is considerably increased and resulted in the improved ferroelectric and pyroelectric properties of the films.

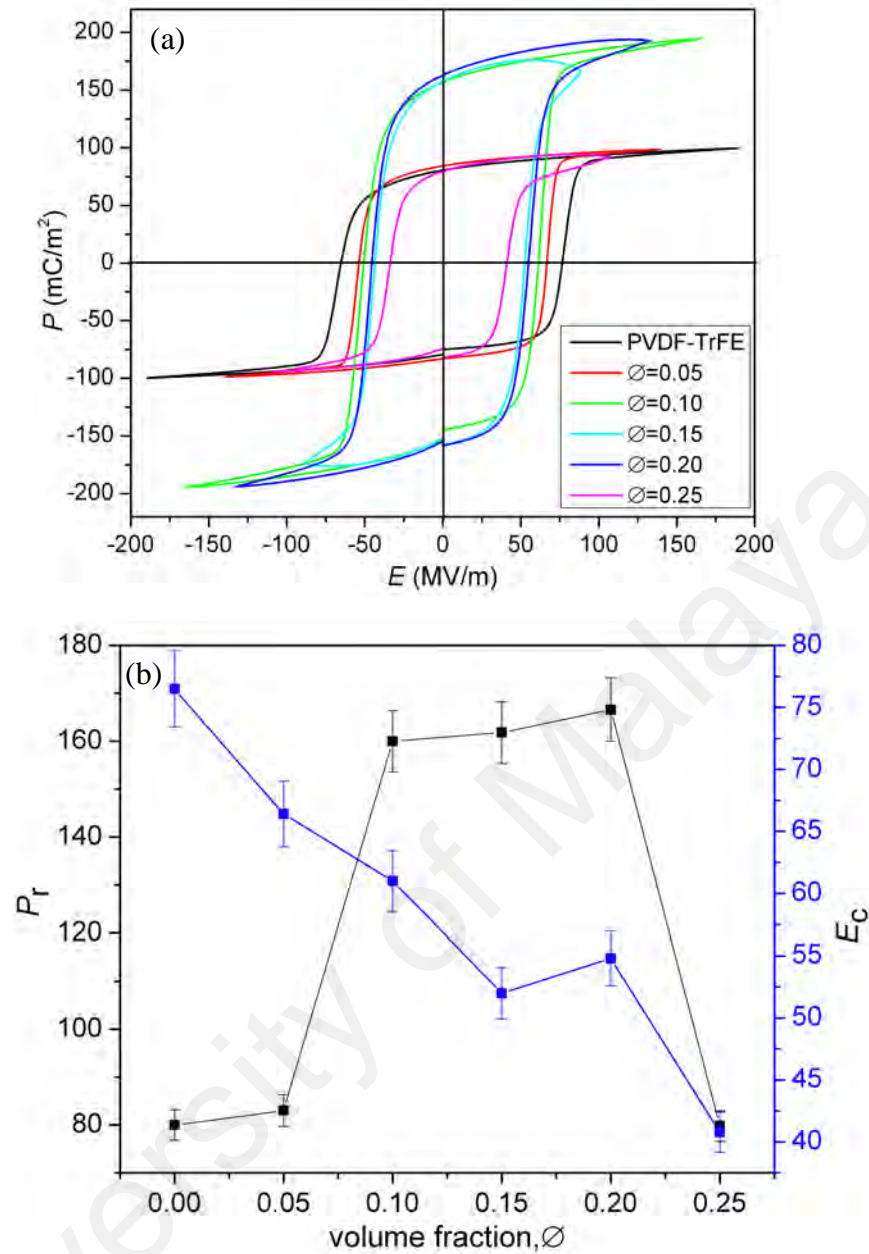


Figure 6.8: (a) P - E hysteresis loops (b) remanent polarization, P_r and coercive field, E_c of P(VDF-TrFE) /BNT-0.6 CeO₂ composite films with various volume fractions, ϕ .

6.7 Pyroelectric properties

Figure 6.9(a) shows the rectangular waveform of pyroelectric current obtained when a triangular temperature waveform was applied to the poled composite. Pyroelectric current, I_p is obtained due to the change in the spontaneous polarization of the sample with temperature. The I_p is defined as the accumulated surface charge density that flows when the temperature change. The pyroelectric coefficient of the

composite thin films with various volume fractions of BNT-0.6 CeO₂ were plotted and shown in Figure 6.9(b). The pyroelectric coefficients of the composite thin films increase proportionately with the increase of the volume fraction of BNT-0.6 CeO₂. The highest pyroelectric coefficient was obtained at $\phi = 0.2$ which is about 43 $\mu\text{C}/\text{m}^2\text{K}$ which is 34 % higher than that of pure P(VDF-TrFE). However, the pyroelectric coefficient for the composite thin film which consist of exceeding $\phi = 0.20$ BNT-0.6 CeO₂ were decreased to 35 $\mu\text{C}/\text{m}^2\text{K}$.

The pyroelectric coefficient of the nanocomposite can be enhanced due to the effective poling process. Since the value of ε_2 is always found to be larger than ε_1 , thus, the local electric field applied on polymer matrix is much higher than local electric field on ceramic inclusion. As a result, the polymer composite can be poled effectively. In addition, both the pyroelectric coefficient of the BNT-0.6 CeO₂ ceramic (650 $\mu\text{C}/\text{m}^2\text{K}$) and the P(VDF-TrFE) (32 $\mu\text{C}/\text{m}^2\text{K}$) have positive sign. Hence, the ceramic and the copolymer phases in the P(VDF-TrFE) / BNT-0.6 CeO₂ nanocomposite are poled in the same direction, probably reinforcing the pyroelectric activity of the composite. If the ceramic and copolymer phase are poled in the opposite direction, the pyroelectric activity of the composite is reduced (Mahdi & Majid, 2016). This poling effect also contributes to an increase in the effective applied field between the interfaces and, consequently reduced the required poling field on the nanocomposite thin film.

In the P(VDF-TrFE)/ BNT-0.6 CeO₂ nanocomposite, the formation of space charge layers at the interface is due to the presence of BNT-0.6 CeO₂ ferroelectric nanoparticles. This is attributed to increase in a potential spontaneous polarization, which has enhanced the pyroelectric coefficient. The nanocomposite interface interactions between the copolymer and nanoparticle of the ceramic are characterized by modified copolymer chain dynamics close to the nanoparticle surface.

Surrounding molecules are more attracted to surface atoms, which have higher energy state compared to that of atoms in the interior of material. The nanoparticles attraction cause copolymer molecules close to the nanoparticle interactive surface to become more mobile. The attributes of the copolymer on the whole can be changed with limited volume fraction addition. This is due to high ratio of free volume areas exhibited by nanoparticles (1000-fold higher compared to particles of micrometer size) (Ding et al., 2003; Liu & Brinson, 2008).

In addition, the mark increase in the pyroelectric coefficient is attributed to conductivity of the ceramic in the composite system, the phase structure of P(VDF-TrFE) and the promotion of non-homogeneous domain at lowered activation field in the absent of inclusions. However, it is important to note that higher dielectric loss, are expected due to higher conductivity as the volume fraction of the inclusion increases. The conductivity of the composite should be limited by reducing the volume fraction of the inclusion; otherwise, it may induce dissipation and degradation of the properties of the materials. Higher volume fraction of BNT-0.6 CeO₂ inclusion in a polymer matrix will contribute to higher d.c conduction in a nanocomposite. The high d.c conduction in nanocomposite will form space charge in between the electrode and the nanocomposite. This may decrease the effective electric field applied in the nanocomposite during the poling process, thus reduced the pyroelectricity in the sample. Thus, the optimum volume fraction of BNT-0.6 CeO₂ dispersed in the polymer nanocomposite thin films is identified $\phi = 0.20$.

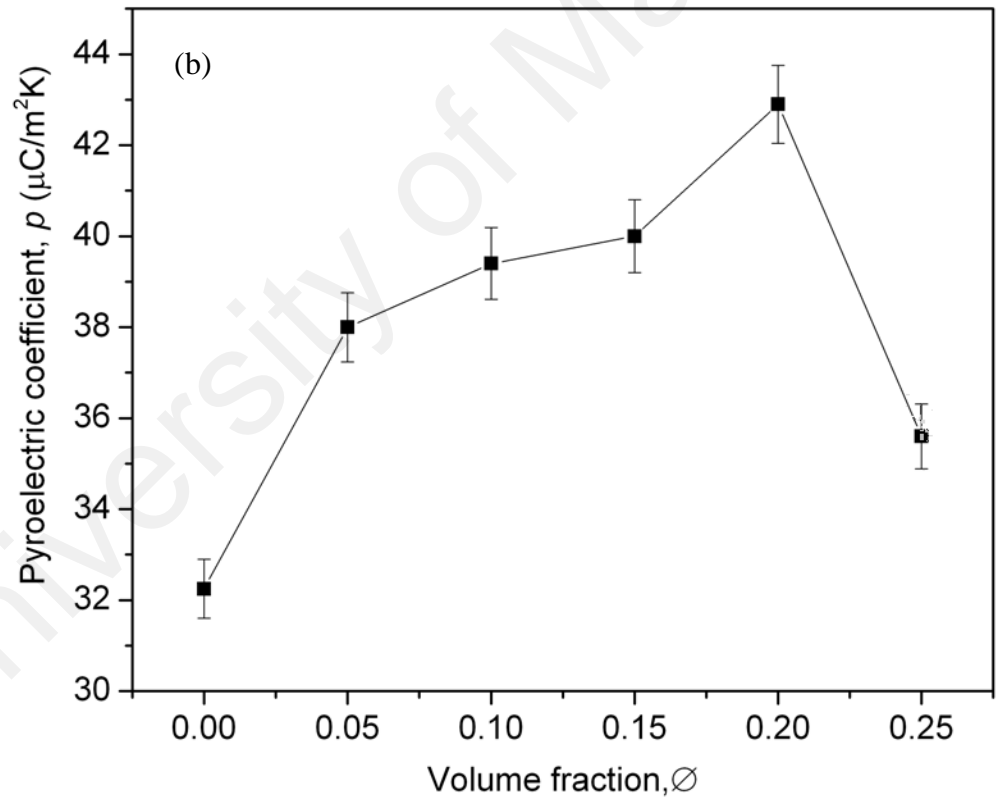
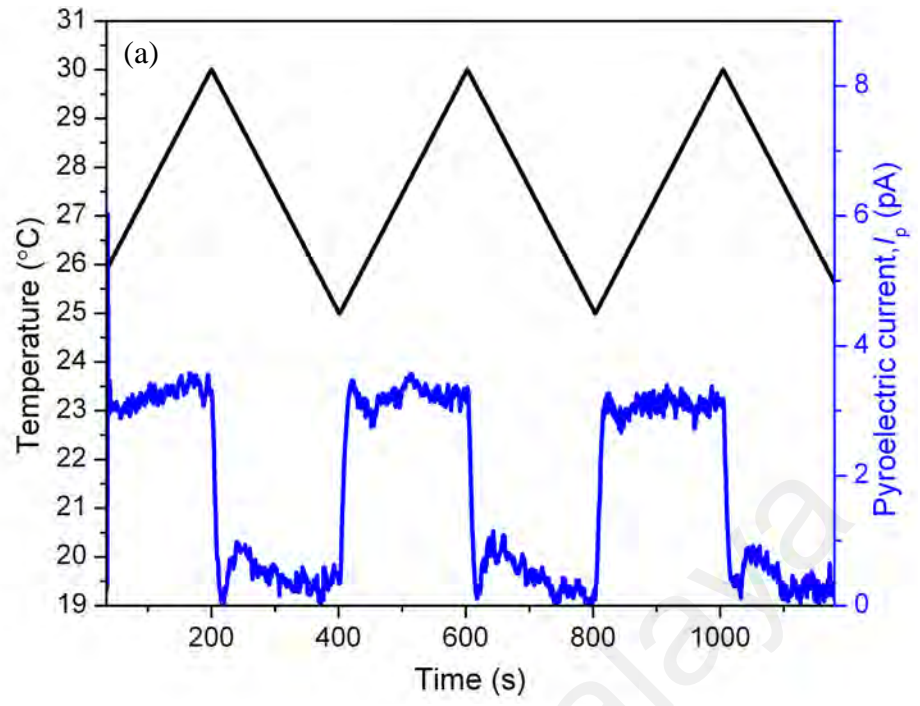


Figure 6.9: (a) Change in pyroelectric current with time and temperature of $\phi = 0.20$ and (b) pyroelectric coefficient, p with volume fraction.

6.8 Leakage current.

Figure 6.10 shows the leakage current density versus electric field (J - E) of P(VDF-TrFE) and P(VDF-TrFE) /BNT-0.6 CeO₂ thin film composites measured at room temperature. The leakage current density increases with the increase of electric field and saturated above 10 MV/m. From the graph, it also can be seen that the leakage current increases from 10⁻⁶ A/cm to 10⁻³ A/cm with increasing the volume fraction of the BNT-0.6 CeO₂ ceramic from $\phi = 0.0$ to $\phi = 0.25$.

The ceramic inclusion with a higher conductivity when embedded in the polymer system has increased the conductivity of the composite system. The leakage current in BNT-0.6 CeO₂ is usually attributed to space charges; such as oxygen vacancies, which are induced by Bi volatilization during sintering process and also space charges between doping ion CeO₂, and BNT with hole-carriers. The leakage current is also likely to be caused by the particle aggregation at higher ceramic volume fraction in the composite system (see Figure 6.3(g)). The particle aggregation causes an increased level of interaction between the ceramic inclusions, which gives rise to percolate pathways throughout the composite and formed a parallel connectivity. This is reflected in the equivalent circuit (see Figure 6.4(b)) through the fact that embedded ceramic parallelepiped almost touches top and bottom electrodes, thus easily break down the samples under a strong electric field.

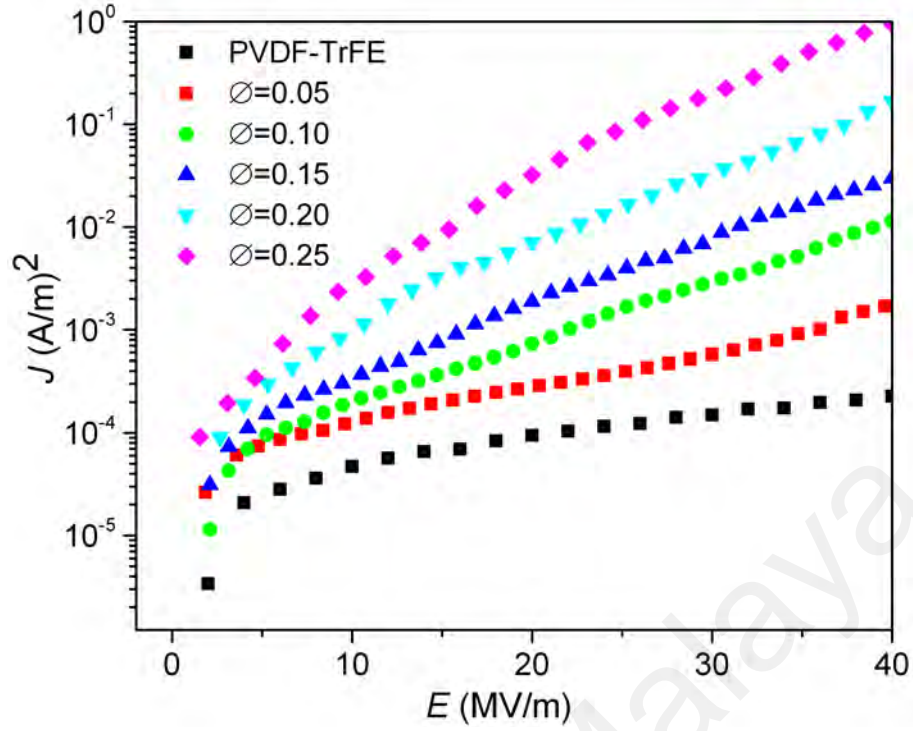


Figure 6.10: Leakage current density of P(VDF-TrFE) and P(VDF-TrFE) /BNT-0.6 CeO₂ composite with various volume fractions.

6.9 Piezoelectric constant, d_{33} of P(VDF-TrFE) /BNT-0.6 CeO₂ thick film at $\text{Ø}=0.20$.

In order to measure piezoelectric constant, d_{33} for the nanocomposite thin film, the sample of P(VDF-TrFE) /BNT-0.6 CeO₂ was prepared in the form of bulk film or free-standing film at the optimized ferroelectric and pyroelectric properties of composite thin film which is the 0.20 volume fraction. The d_{33} constant was measured using d_{33} meter (refer to Figure 6.11).

The piezoelectric constant can be defined as strain/electric field at a constant stress or charge density/stress at a constant electric field. When both stress and electric displacement are aligned with the poling direction which is in the direction of thickness, the coefficient is referred to the longitudinal piezoelectric coefficient, d_{33} . When the ceramic is subjected to a tensile stress, the separation between two charge centres increases and resulting in a longer dipole moment arm and hence a higher spontaneous polarisation (P_s). As P_s increases, positive charges will be

generated on the anode. Where the electrode is subjected to positive voltage during poling, it causes a positive sign of d_{33} ceramic (Chan et al., 1999). Conversely, in the P(VDF-TrFE) polymer which has a semi-crystalline structure; the dipoles exist in the rigid crystal lamellas. The amorphous region will deform giving an increase in thickness when a tensile stress is applied (Broadhurst & Davis, 1984). This shows that the rigid crystal lamellas are dispersed across a larger volume and caused decreasing in P_s . Since P_s is proportional to the dipole moment per unit volume, it produces a decrease in the positive charges on the anode. Therefore, P(VDF-TrFE) copolymer has a negative piezoelectric constant due to the dimensional effect (Broadhurst & Davis, 1984; Chan et al., 1999). Since, the piezoelectric constant of ceramic and copolymer have opposite sign, the piezoelectric activities of two phases in the composite partially cancel each other after poling. The sample was poled in the opposite direction initially show positive and increasing in piezoelectric constant (Mahdi & Majid, 2016). The BNT-0.6 CeO₂ ceramics exhibited a positive signs of $d_{33} = 90$ pC/N, while the P(VDF-TrFE) polymer exhibited a negative sign of $d_{33} = -38$ pC/N (Takeo Furukawa, 2003). The average of d_{33} constant of 0.2 P(VDF-TrFE) /BNT-0.6 CeO₂ is about 49 pC/N. Table 6.1 compares the electrical properties of the P(VDF-TrFE) /BNT-0.6 CeO₂ nanocomposites to the other P(VDF-TrFE) composite systems in the literature. The piezoelectric constant and remanent polarization exhibit fairly high value of $d_{33} = 49$ pC/N and $P_r = 166$ mC/m², with low coercive field, $E_c = 55$ MV/m at the low volume fraction, ϕ of 0.20.



Figure 6.11: The d_{33} meter measurements.

Table 6.1: The P(VDF-TrFE)-based composite systems.

	P_r (mC/m ²)	E_c (MV/m)	d_{33} (pC/N)	p (μ C/m ² K)	ϕ	References
P(VDF-TrFE)-BNT	115	80	-	50	0.2	(Mahdi et al., 2015)
P(VDF-TrFE)-BNT0.6CeO ₂	166	55	49	43	0.2	This work
P(VDF-TrFE)-BaTiO ₃	47	138	-	-	0.8	(Valiyaneerilakkal & Varghese, 2013)
P(VDF-TrFE)-BNT-BKT-BT	-	-	40	95	0.2,0.3	(Mahdi & Majid, 2016)
P(VDF-TrFE)-PZT	105	40	42	49.9	0.3,0.6	(Dietze & Es-Souni, 2008; Ng et al., 2000)

6.10 Conclusion

A significant improvement in ferroelectric and pyroelectric properties in the P(VDF-TrFE) /BNT-0.6 CeO₂ composite have been demonstrated when 0.2 volume fraction of BNT ceramic is dispersed in the composite thin film. Maxwell-Wagner's model considers the conductivity of constituent in the composite thin film which attributed to increase in the conductivity of polymer matrix. The conductivity of constituent is significantly led to a more efficient poling process and as a result, it reduces the coercive field, E_c while increasing the remanent polarization, P_r and

pyroelectric coefficient, p of the composite. The piezoelectric constant, d_{33} of 0.2 volume fraction in bulk film composite exhibit high value of $d_{33}= 49$ pC/N.

University of Malaya

CHAPTER 7: CONCLUSION

7.1 Conclusion

This study is mainly divided into two parts; ceramic and polymer nanocomposite. The first part was focused in synthesizing and analyzing the physical and electrical (ferro-, pyro- and piezoelectric) properties of pure and CeO₂ doped BNT a lead-free ceramic in nano size. From the study, the best sample with optimal physical and electrical property was identified and used in the second part as a filler in a polymeric matrix P(VDF-TrFE) to form a 0-3 nanocomposite. The objective of this study is to improve the electrical properties of the ferroelectric polymer by incorporating ferroelectric ceramic so that it could be used in microelectronic applications.

Initially, the BNT nanostructured ceramic was successfully synthesized by sol-gel method using acetyl acetone as a stabilizing agent. The XRD results showed high crystallinity for the samples sintered at 1100 °C. BNT formed perovskite structure with rhombohedral phase. The FESEM results showed that the size of the BNT nanoparticles were (43 ± 13) nm in average. The sintered BNT samples were well dispersed with homogenous grain growth and minimal porosity. The non-poled and poled samples exhibited a few phase transitions; transition temperature between ferroelectric, anti-ferroelectric and paraelectric phase. Moreover, thickness extensional (TE) resonance peaks were observed in the ferroelectric phase in the dielectric spectrum. The piezoelectric constants and electromechanical coupling coefficient were calculated from the dielectric resonant peaks. At room temperature, the electromechanical coupling coefficient, k_{33} of 0.39, the Young modulus, c_{33} of 170 GPa and the piezoelectric constant, d_{33} of 74 pC/N were obtained. From the P - E hysteresis loop, the remanent polarization, P_r and coercive field which are $47 \mu\text{C}/\text{cm}^2$

and 55 kV/cm were calculated, respectively. The poled samples exhibit the pyroelectric coefficient, p of 141 $\mu\text{C}/\text{m}^2\text{K}$. However, efficient poling (i.e field-cooled polling at 4 kV and 200 °C for 30 minutes) was able to increase the p to 625 $\mu\text{C}/\text{m}^2\text{K}$. The homogenous nanostructure ceramics and an effective poling contribute to high interphase grain boundary, domain pinning neutralize the trap charges at grain boundaries and reduce the coercive field of the samples. The BNT nanoceramic synthesized from the sol-gel method displayed relatively higher dielectric constant, piezo-, pyro- and ferroelectric properties compared to that of the conventional BNT ceramic.

Subsequently, CeO_2 was doped into the BNT ceramic in order to improve the remnant polarization and reduce the coercive field of the pure BNT. The doping gives a remarkable improvement to the phase structure and electrical properties of the BNT ceramic. The XRD results show that the doping induced phase structure changed from single rhombohedral structure to rhombohedral-tetragonal morphotropic phase boundary. Moreover, the grain size gradually reduced from $\sim 0.5 \mu\text{m}$ to $\sim 0.3 \mu\text{m}$ and the morphologies of BNT doped becomes square and rectangular in shapes compared to that of non-doped BNT. The dielectric constant, ϵ' increased to ~ 1276 as the weight percentage of doping CeO_2 increased to 0.6 wt.%. However, further increase of CeO_2 deteriorates the dielectric and ferroelectric properties of the samples. Meanwhile the transition temperatures of the non-poled samples before and after doping remain unchanged. The piezoelectric properties such as the electromechanical coupling coefficient, k_{33} and the piezoelectric constant, d_{33} improved remarkably for the samples doped with 0.6 wt.% of CeO_2 . Likewise, the remanent polarization, P_r improved to 56 $\mu\text{C}/\text{cm}^2$ and the coercive field, E_c was reduced to 53 kV/cm. The P - E loops became rounded and samples were more conductive when an excessive CeO_2 was added into the BNT ceramic. The

pyroelectric coefficient is also correlated with the spontaneous polarization that can be observed from ferroelectric hysteresis loop. The remarkable changes in the samples are due to the change in phase structure and the defects in the lattice structure. The defects are due to the occupation of Ce ions in the B-site of the BNT structure (during sintering process) and the dislocation of Ce ions when the samples are poled at high electric field. However, the leakage current of the samples become excessively high when the CeO₂ dopant surpassing 1.0 wt.%, thus the piezoelectric, pyroelectric and ferroelectric properties of the BNT ceramic deteriorates.

The BNT doped with 0.6 wt.% CeO₂ with the optimized electrical properties was subsequently used as an inclusion into a copolymer P(VDF-TrFE) to form a 0-3 nanocomposite. The P(VDF-TrFE) /BNT-0.6 CeO₂ nanocomposite was examined. The XRD results showed that the crystalline β -phase of P(VDF-TrFE) at (110/200) orientation planes has exhibited an orthorhombic structure and rhombohedral-tetragonal morphotropic phase boundary structure of BNT-0.6 CeO₂. The ceramic inclusions with volume fractions less than 0.20 were uniformly dispersed throughout the polymer matrix and formed 0-3 composite. The dielectric constant and dielectric loss of the nanocomposite thin film increases with increasing volume fraction of the ceramic. The effective dielectric constants of the experiment data were theoretically fitted to the theoretical models of Maxwell and the effective medium theory (EMT) models. The Maxwell-Wagner's model also fitted well with experimental data. This model takes into consideration the conductivities of the constituents that imply an increase in the conductivity of the polymer matrix. It is significantly improving the poling mechanism by reducing the required electric field. Hence it has improved the ferroelectric and pyroelectric properties of the nanocomposite thin film. However, the inclusion of ceramic in a polymer ceramic nanocomposite thin film must be limited to a certain level of volume fraction. Above $\phi = 0.25$, the leakage current

becomes excessively high and deteriorates the ferroelectric and pyroelectric properties of the polymer composite thin film. The bulk film of P(VDF-TrFE)/BNT-0.6 CeO₂ nanocomposite at $\phi = 0.20$ was used for measuring the piezoelectric property of the nanocomposite. The d_{33} value obtained was 49 pC/N.

7.2 Future Works

BNT was currently synthesized by sol-gel method to form bulk ceramics. In the future, the BNT ceramic can be prepared in thin films by spin-coating technique on silicon substrate. These thin films can be used in the thermal-electrical energy conversion applications. Currently, the sol-gel method can only be used to prepare the nanoceramics in a very small scale and might not be applicable for large production. Further study to improve the method of preparation for mass production in a larger-scale can be useful in industry. Moreover, the composite thin films were prepared on substrate. The samples can also be prepared in a thick film and the true piezoelectric constants (without the substrate restriction) can be analyzed using piezoelectric resonance method. These ferroelectric nanoceramic and nanocomposite with the extraordinary electrical responses could be used in many applications such as sensors, actuators, piezo- and pyroelectric energy harvesting applications, functional organic ferroelectric materials in data storage, field effect transistor and microelectromechanical system (MEMs).

REFERENCES

- Alonso-Sanjosé, D., Jimenez, R., Bretos, I., & Calzada, M. L. (2009). Lead-Free Ferroelectric ($\text{Na}_{1/2}\text{Bi}_{1/2}$)/ TiO_3 - BaTiO_3 Thin Films in the Morphotropic Phase Boundary Composition: Solution Processing and Properties. *Journal of the American Ceramic Society*, 92(10), 2218-2225.
- Baur, M. E., & Stockmayer, W. H. (1965). Dielectric relaxation in liquid polypropylene oxides. *The Journal of Chemical Physics*, 43(12), 4319-4325.
- Bergman Jr, J. G., McFee, J. H., & Crane, G. R. (1971). Pyroelectricity and optical second harmonic generation in polyvinylidene fluoride films. *Applied Physics Letters*, 18(5), 203-205.
- Broadhurst, M. G., & Davis, G. T. (1984). Physical basis for piezoelectricity in PVDF. *Ferroelectrics*, 60(1), 3-13.
- Cao, W., & Randall, C. A. (1996). Grain size and domain size relations in bulk ceramic ferroelectric materials. *Journal of Physics and Chemistry of Solids*, 57(10), 1499-1505.
- Cerne, M., Andronescu, E., Radu, R., Fochi, F., & Galassi, C. (2010). Sol-gel synthesis and characterization of BaTiO_3 -doped ($\text{Bi}_{0.5}\text{Na}_{0.5}$)/ TiO_3 piezoelectric ceramics. *Journal of Alloys and Compounds*, 490(1), 690-694.
- Cerne, M., Trupina, L., Dragoi, C., Vasile, B. S., & Trusca, R. (2012). Structural and piezoelectric characteristics of BNT-BT_{0.05} thin films processed by sol-gel technique. *Journal of Alloys and Compounds*, 515, 166-170.
- Cerne, M., Vasile, B. S., Capiati, C., Ioncea, A., & Galassi, C. (2012). Dielectric and piezoelectric behaviors of NBT-BT_{0.05} processed by sol-gel method. *Journal of the European Ceramic Society*, 32(1), 133-139.
- Chan, H. L. W., Chan, W. K., Zhang, Y., & Choy, C. L. (1998). Pyroelectric and piezoelectric parameters of lead titanate/vinylidene fluoride-trifluoroethylene copolymer 0-3 composites. *IEEE Transactions on Dielectrics and Electrical Insulation*, (5), 505-512.
- Chan, H. L. W., Ng, P. K. L., & Choy, C. L. (1999). Effect of poling procedure on the properties of lead zirconate titanate/vinylidene fluoride-trifluoroethylene composites. *Applied Physics Letters*, 74(20), 3029-3031.

- Chen, M., Xu, Q., Kim, B. H., Ahn, B. K., & Chen, W. (2008). Effect of CeO_2 addition on structure and electrical properties of $(\text{Na}_{0.5}\text{Bi}_{0.5})_{0.93}\text{Ba}_{0.07}\text{TiO}_3$ ceramics prepared by citric method. *Materials Research Bulletin*, 43(6), 1420-1430.
- Chu, B.-J., Chen, D.-R., Li, G.-R., & Yin, Q.-R. (2002). Electrical properties of $\text{Na}_{1/2}\text{Bi}_{1/2}\text{TiO}_3$ - BaTiO_3 ceramics. *Journal of the European Ceramic Society*, 22(13), 2115-2121.
- Chu, B.-J., Cho, J.-H., Lee, Y.-H., Kim, B.-I., & Chen, D. R. (2002). The potential application of BNT-based ceramics in large displacement actuation. *Journal of Ceramic Processing Research*, 3(3/2), 231-234.
- Dahiya, R. S., & Valle, M. (2013). Appendix A Fundamentals of piezoelectricity: *Springer*.
- Dang, Z. M., Shen, Y., & Nan, C. W. (2002). Dielectric behavior of three-phase percolative Ni-BaTiO_3 /polyvinylidene fluoride composites. *Applied Physics Letters*, 81(25), 4814-4816.
- Das Gupta, D. K., & Doughty, K. (1977). Changes in x-ray diffraction patterns of polyvinylidene fluoride due to corona charging. *Applied Physics Letters*, 31(9), 585-587.
- Davis, G. T., McKinney, J. E., Broadhurst, M. G., & Roth, S. (1978). Electric-field-induced phase changes in poly (vinylidene fluoride). *Journal of Applied Physics*, 49(10), 4998-5002.
- Dietze, M., & Es-Souni, M. (2008). Structural and functional properties of screen-printed PZT-PVDF-TrFE composites. *Sensors and Actuators A: Physical*, 143(2), 329-334.
- Ding, W., Eitan, A., Fisher, F. T., Chen, X., Dikin, D. A., Andrews, Ruoff, R. S. (2003). Direct observation of polymer sheathing in carbon nanotube-polycarbonate composites. *Nano Letters*, 3(11), 1593-1597.
- Fang, F., Yang, W., Zhang, M. Z., & Wang, Z. (2009). Mechanical response of barium-titanate/polymer 0-3 ferroelectric nano-composite film under uniaxial tension. *Composite Science and Technology*, 69(5), 602-605.

- Fu, P., Xu, Z., Chu, R., Li, W., Zang, G., & Hao, J. (2010a). Piezoelectric, ferroelectric and dielectric properties of La_2O_3 -doped $(\text{Bi}_{0.5}\text{Na}_{0.5})_{0.94}\text{Ba}_{0.06}\text{TiO}_3$ lead-free ceramics. *Materials & Design*, 31(2), 796-801.
- Fu, P., Xu, Z., Chu, R., Li, W., Zang, G., & Hao, J. (2010b). Piezoelectric, ferroelectric and dielectric properties of Nd_2O_3 -doped $(\text{Bi}_{0.5}\text{Na}_{0.5})_{0.94}\text{Ba}_{0.06}\text{TiO}_3$ lead-free ceramics. *Materials Science and Engineering: B*, 167(3), 161-166.
- Furukawa, T. (1989). Ferroelectric properties of vinylidene fluoride copolymers. *Phase Transitions: A Multinational Journal*, 18(3-4), 143-211.
- Furukawa, T. (1997). Structure and functional properties of ferroelectric polymers. *Advances in Colloid and Interface Science*, 71, 183-208.
- Furukawa, T., Fujino, K., & Fukada, E. (1976). Electromechanical properties in the composites of epoxy resin and PZT ceramics. *Japanese Journal of Applied Physics*, 15(11), 2119-2129.
- Furukawa, T., & Fukada, E. (1976). Piezoelectric relaxation in poly (γ -benzyl-glutamate). *Journal of Polymer Science: Polymer Physics Edition*, 14(11), 1979-2010.
- Furukawa, T., & Fukada, E. (1977). Piezoelectric relaxation in composite epoxy-PZT system due to ionic conduction. *Japanese Journal of Applied Physics*, 16(3), 453-458.
- Furukawa, T., Ishida, K., & Fukada, E. (1979). Piezoelectric properties in the composite systems of polymers and PZT ceramics. *Journal of Applied Physics*, 50(7), 4904-4912.
- Furukawa, T., Nakajima, T., & Takahashi, Y. (2006). Factors governing ferroelectric switching characteristics of thin VDF/TrFE copolymer films. *IEEE Transactions on Dielectrics and Electrical Insulation*, 13(5), 1120-1131.
- Furukawa, T., Wen, J. X., Suzuki, K., Takashina, Y., & Date, M. (1984). Piezoelectricity and pyroelectricity in vinylidene fluoride/trifluoroethylene copolymers. *Journal of Applied Physics*, 56(3), 829-834.
- Furukawa, T., Yasuda, K., & Takahashi, Y. (2004). Dielectric and conductive spectra of the composite of barium titanate and LiClO_4 /sub 4/-doped polyethylene oxide. *IEEE Transactions on Dielectrics and Electrical Insulation*, 11(1), 65-71.

- Gan, W. C., & Majid, W. H. A. (2014). Effect of TiO_2 on enhanced pyroelectric activity of PVDF composite. *Smart Materials and Structures*, 23(4), 45026-45035.
- Gan, W. C., & Majid, W. H. A. (2015). Enhancing pyroelectric and ferroelectric properties of PVDF composite thin films by dispersing a non-ferroelectric inclusion La_2O_3 for application in sensors. *Organic Electronics*, 26, 121-128.
- Gan W. C. (2015). Ferroelectric and pyroelectric properties of form IV Poly(vinylidene fluoride) and its composites. (Unpublished PhD's thesis). University of Malaya, Kuala Lumpur.
- Garg, A., & Agrawal, D. C. (1999). Structural and electrical studies of CeO_2 modified lead zirconate titanate ceramics. *Journal of Materials Science: Materials in Electronics*, 10(9), 649-652.
- Ghitulica, C., Cernea, M., Vasile, B. S., Andronescu, E., Vasile, O. R., Dragoi, C., & Trusca, R. (2013). Structural and electrical properties of NBT–BT_{0.08} ceramic prepared by the pyrosol method. *Ceramics International*, 39(5), 5925-5930.
- Gregorio, R., & Borges, D. S. (2008). Effect of crystallization rate on the formation of the polymorphs of solution cast poly (vinylidene fluoride). *Polymer*, 49(18), 4009-4016.
- Hagiyeve, M. S., Ismailzade, I. H., & Abiyev, A. K. (1984). Pyroelectric properties of $(\text{Na}_{1/2}\text{Bi}_{1/2})\text{TiO}_3$ ceramics. *Ferroelectrics*, 56(1), 215-217.
- Halim, N. A., Velayutham, T. S., & Majid, W. H. A. (2016). Pyroelectric, ferroelectric, piezoelectric and dielectric properties of $\text{Na}_{0.5}\text{Bi}_{0.5}\text{TiO}_3$ ceramic prepared by sol-gel method. *Ceramics International*, 42(14), 15664-15670.
- Han K. H., Riman R., Safari A. (1990). Dielectric and piezoelectric properties of flexible 0-3 composites prepared by co-precipitated $(\text{Pb}, \text{Bi})(\text{Ti}, \text{Fe})\text{O}_3$ ceramic powder. *IEEE proceeding of the 7th International Symposium on Applications of Ferroelectrics*, 591-594.
- Hao, J., Wang, X., Chen, R., & Li, L. (2005). Synthesis of $(\text{Bi}_{0.5}\text{Na}_{0.5})\text{TiO}_3$ nanocrystalline powders by stearic acid gel method. *Materials Chemistry and Physics*, 90(2), 282-285.

- Hilczer, B., Kułek, J., Markiewicz, E., Kosec, M., & Malič, B. (2002). Dielectric relaxation in ferroelectric PZT–PVDF nanocomposites. *Journal of Non-Crystalline Solids*, 305(1), 167-173.
- Hiruma, Y., Nagata, H., & Takenaka, T. (2009). Thermal depoling process and piezoelectric properties of bismuth sodium titanate ceramics. *Journal of Applied Physics*, 105(8), 84112-84122.
- Hoshina, T., Takizawa, K., Li, J., Kasama, T., Kakemoto, H., & Tsurumi, T. (2008). Domain size effect on dielectric properties of barium titanate ceramics. *Japanese Journal of Applied Physics*, 47(9S), 7607-7616.
- Jaffe, B. (2012). Piezoelectric ceramics (Vol. 3): *Elsevier*.
- Jaffe, B., Roth, R. S., & Marzullo, S. (1954). Piezoelectric properties of lead zirconate-lead titanate solid-solution ceramics. *Journal of Applied Physics*, 25(6), 809-810.
- Jordan, T. L., & Ounaies, Z. (2001). Piezoelectric ceramics characterization: *DTIC Document*.
- Jumali, H., Hafizuddin, M., Siti, M. M., Awang, R., Yahaya, M., & Salleh, M. M. (2012). Effect of annealing temperatures on nanostructure of NBT ceramics prepared via sol gel method. *Advanced Materials Research*, 364, 412-416.
- Jumali, M. H. H., Said, M. R. M., & Wee, N. Y. (2010). Kelakuan pengesanan tekanan bagi seramik natrium bismut titanat. *Sains Malaysiana*, 39(4), 621-626.
- Kawai, H. (1969). The piezoelectricity of poly (vinylidene fluoride). *Japanese Journal of Applied Physics*, 8(7), 975.
- Kim, B.-H., Han, S.-J., Kim, J.-H., Lee, J.-H., Ahn, B.-K., & Xu, Q. (2007). Electrical properties of $(1-x)(\text{Bi}_{0.5}\text{Na}_{0.5})\text{TiO}_3-x\text{BaTiO}_3$ synthesized by emulsion method. *Ceramics International*, 33(3), 447-452.
- Kobayashi, M., Tashiro, K., & Tadokoro, H. (1975). Molecular vibrations of three crystal forms of poly (vinylidene fluoride). *Macromolecules*, 8(2), 158-171.
- Kocharyan, N. M., & Pachadzhyan, K. B. (1968). The piezoelectric effect in polymers. *Mechanics of Composite Materials*, 4(1), 117-119.

- Kontsos, A., & Landis, C. M. (2009). Computational modeling of domain wall interactions with dislocations in ferroelectric crystals. *International Journal of Solids and Structures*, 46(6), 1491-1498.
- Lando, J. B., & Doll, W. W. (1968). The polymorphism of poly (vinylidene fluoride). I. The effect of head-to-head structure. *Journal of Macromolecular Science, Part B: Physics*, 2(2), 205-218.
- Lang, S. B. (1974). Sourcebook of Pyroelectricity, Gordon and Breach. New York.
- Lang, S. B. (2005). Pyroelectricity: from ancient curiosity to modern imaging tool. *Physics Today*, 58(8), 31-36.
- Li, H.-d., & Yao, W.-l. (2004). Some effects of different additives on dielectric and piezoelectric properties of $(\text{Bi}_{1/2}\text{Na}_{1/2})\text{TiO}_3$ - BaTiO_3 morphotropic-phase-boundary composition. *Materials Letters*, 58(7), 1194-1198.
- Li, Y., Chen, W., Xu, Q., Zhou, J., Wang, Y., & Sun, H. (2007). Piezoelectric and dielectric properties of CeO_2 -doped $\text{Bi}_{0.5}\text{Na}_{0.44}\text{K}_{0.06}\text{TiO}_3$ lead-free ceramics. *Ceramics International*, 33(1), 95-99.
- Liao, Y., Xiao, D., Lin, D., Zhu, J., Yu, P., Wu, L., & Wang, X. (2006). The effects of CeO_2 doping on piezoelectric and dielectric properties of $\text{Bi}_{0.5}(\text{Na}_{1-x-y}\text{K}_x\text{Li}_y)_{0.5}\text{TiO}_3$ piezoelectric ceramics. *Materials Science and Engineering: B*, 133(1), 172-176.
- Liu, H., & Brinson, L. C. (2008). Reinforcing efficiency of nanoparticles: a simple comparison for polymer nanocomposites. *Composites Science and Technology*, 68(6), 1502-1512.
- Lovinger, A. J. (1983). Ferroelectric polymers. *Science*, 220(4602), 1115-1121.
- Lu, Y., Claude, J., Norena-Franco, L. E., & Wang, Q. (2008). Structural Dependence of Phase Transition and Dielectric Relaxation in Ferroelectric Poly (vinylidene fluoride- chlorotrifluoroethylene- trifluoroethylene)s. *The Journal of Physical Chemistry B*, 112(34), 10411-10416.
- Mahdi, R. I., Gan, W. C., Halim, N. A., Velayutham, T. S., & Majid, W. H. A. (2015). Ferroelectric and pyroelectric properties of novel lead-free polyvinylidene fluoride-trifluoroethylene- $\text{Bi}_{0.5}\text{Na}_{0.5}\text{TiO}_3$ nanocomposite thin films for sensing applications. *Ceramics International*, 41(10), 13836-13843.

- Mahdi, R. I., & Majid, W. H. A. (2016). Piezoelectric and pyroelectric properties of BNT-base ternary lead-free ceramic–polymer nanocomposites under different poling conditions. *RSC Advances*, 6(84), 81296-81309.
- McLachlan, D. S., Blaszkiewicz, M., & Newnham, R. E. (1990). Electrical resistivity of composites. *Journal of the American Ceramic Society*, 73(8), 2187-2203.
- Nagata, H. (2008). Electrical properties and tracer diffusion of oxygen in some Bi-based lead-free piezoelectric ceramics. *Journal of the Ceramic Society of Japan*, 116(1350), 271-277.
- Nagata, H., & Takenaka, T. (2001). Additive effects on electrical properties of $(\text{Bi}_{1/2}\text{Na}_{1/2})\text{TiO}_3$ ferroelectric ceramics. *Journal of the European Ceramic Society*, 21(10), 1299-1302.
- Newnham, R. E., Skinner, D. P., & Cross, L. E. (1978). Connectivity and piezoelectric-pyroelectric composites. *Materials Research Bulletin*, 13(5), 525-536.
- Ng, K. L., Chan, H. L. W., & Choy, C. L. (2000). Piezoelectric and pyroelectric properties of PZT/P(VDF-TrFE) composites with constituent phases poled in parallel or antiparallel directions. *IEEE Transactions on Ultrasonics, Ferroelectrics, and Frequency Control*, 47(6), 1308-1315.
- Panigrahi, M. R., & Panigrahi, S. (2010). Structural analysis of 100 % relative intense peak of $\text{Ba}_{1-x}\text{Ca}_x\text{TiO}_3$ ceramics by X-ray powder diffraction method. *Physica B: Condensed Matter*, 405(7), 1787-1791.
- Ploss, B., Ploss, B., Shin, F. G., Chan, H. L. W., & Choy, C. L. (1998). Separate poling of inclusions and matrix in PT/P(VDF-TrFE) 0-3 composites. *IEEE International Symposium on Applications of Ferroelectric*, 299-302.
- Ploss, B., Ng, W.-Y., Chan, H. L.-W., Ploss, B., & Choy, C.-L. (2001). Poling study of PZT/P(VDF-TrFE) composites. *Composites Science and Technology*, 61(7), 957-962.
- Ploss, B., Shin, F. G., Chan, H. L. W., & Choy, C. L. (2000a). Pyroelectric activity of ferroelectric PT/PVDF-TRFE. *IEEE Transactions on Dielectrics and Electrical Insulation*, 7(4), 517-522.

- Ploss, B., Ploss, B., Shin, F. G., Chan, H. L. W., & Choy, C. L. (2000b). Pyroelectric or piezoelectric compensated ferroelectric composites. *Applied Physics Letters*, 76(19), 2776-2778.
- Rao, Y., Qu, J., Marinis, T., & Wong, C. P. (2000). A precise numerical prediction of effective dielectric constant for polymer-ceramic composite based on effective-medium theory. *IEEE Transactions on Components and Packaging Technologies*, 23(4), 680-683.
- Remondiere, F., Malič, B., Kosec, M., & Mercurio, J.-P. (2008). Study of the crystallization pathway of $\text{Na}_{0.5}\text{Bi}_{0.5}\text{TiO}_3$ thin films obtained by chemical solution deposition. *Journal of Sol-Gel Science and Technology*, 46(2), 117-125.
- Reynolds, N. M., Kim, K. J., Chang, C., & Hsu, S. L. (1989). Spectroscopic analysis of the electric field induced structural changes in vinylidene fluoride/trifluoroethylene copolymers. *Macromolecules*, 22(3), 1092-1100.
- Rukmini, H. R., Choudhary, R. N. P., & Rao, V. V. (1998). Effect of doping pairs (La, Na) on structural and electrical properties of PZT ceramics. *Materials Chemistry and Physics*, 55(2), 108-114.
- Schönhals, A., & Kremer, F. (2003). Analysis of dielectric spectra Broadband dielectric spectroscopy. *Springer*, 59-98.
- Scott, J. F. (2007). Applications of modern ferroelectrics. *Science*, 315(5814), 954-959.
- Shan, D., Qu, Y., & Song, J. (2007). Ionic doping effects on crystal structure and relaxation character in $\text{Bi}_{0.5}\text{Na}_{0.5}\text{TiO}_3$ ferroelectric ceramics. *Journal of Materials Research*, 22(03), 730-734.
- Shi, J., & Yang, W. (2009). Piezoelectric and dielectric properties of CeO_2 -doped $(\text{Bi}_{0.5}\text{Na}_{0.5})_{0.94}\text{Ba}_{0.06}\text{TiO}_3$ lead-free ceramics. *Journal of Alloys and Compounds*, 472(1), 267-270.
- Smolenskii, G. A., Isupov, V. A., Agranovskaya, A. I., & Krainik, N. N. (1961). New ferroelectrics of complex composition. *Soviet Physics-Solid State*, 2(11), 2651-2654.
- Suchanicz, J., & Ptak, W. S. (1990). On the phase transition in $\text{Na}_{0.5}\text{Bi}_{0.5}\text{TiO}_3$. *Ferroelectrics Letters Section*, 12(3), 71-78.

- Takenaka, T., Maruyama, K.-i., & Sakata, K. (1991). $(\text{Bi}_{1/2}\text{Na}_{1/2})\text{TiO}_3$ - BaTiO_3 system for lead-free piezoelectric ceramics. *Japanese Journal of Applied Physics*, 30(9S), 2236.
- Takenaka, T., & Sakata, K. (1989). Dielectric, piezoelectric and pyroelectric properties of $(\text{BiNa})_{1/2}\text{TiO}_3$ -based ceramics. *Ferroelectrics*, 95(1), 153-156.
- Takeo Furukawa (2000). Electrical properties of polymer. *Polymer Physics in Japan*.
- Tashiro, K. (1995). Crystal structure and phase transition of PVDF and related copolymers. *Plastics Engineering-New York*-, 28, 63-63.
- Thomas, P., Satapathy, S., Dwarakanath, K., & Varma, K. B. R. (2010). Dielectric properties of poly (vinylidene fluoride)/ $\text{CaCu}_3\text{Ti}_4\text{O}_{12}$ nanocrystal composite thick films. *Polymer Letter*, 632-643.
- Tichý, J., Erhart, J., Kittinger, E., & Přívratská, J. (2010). Fundamentals of piezoelectric sensorics: mechanical, dielectric, and thermodynamical properties of piezoelectric materials: *Springer Science & Business Media*.1-125.
- Tsangaris, G. M., Kouloumbi, N., & Kyvelidis, S. (1996). Interfacial relaxation phenomena in particulate composites of epoxy resin with copper or iron particles. *Materials Chemistry and Physics*, 44(3), 245-250.
- Valiyaneerilakkal, U., & Varghese, S. (2013). Poly (vinylidene fluoride-trifluoroethylene)/barium titanate nanocomposite for ferroelectric nonvolatile memory devices. *AIP Advances*, 3(4), 42131-42136.
- Wada, S., Takeda, K., Muraishi, T., Kakemoto, H., Tsurumi, T., & Kimura, T. (2008). Domain wall engineering in lead-free piezoelectric grain-oriented ceramics. *Ferroelectrics*, 373(1), 11-21.
- Wang, X., Chan, H. L.-W., & Choy, C.-l. (2003). Piezoelectric and dielectric properties of CeO_2 -added $(\text{Bi}_{0.5}\text{Na}_{0.5})_{0.94}\text{Ba}_{0.06}\text{TiO}_3$ lead-free ceramics. *Solid State Communications*, 125(7), 395-399.
- Wang XX, Choy CL, Tang XG, Chan HLW. (2005). Dielectric behavior and microstructure of $\text{Na}_{1/2}\text{Bi}_{1/2}\text{TiO}_3$ - $\text{K}_{1/2}\text{Bi}_{1/2}\text{TiO}_3$ - BaTiO_3 lead-free piezoelectric ceramics. *Journal of Applied Physics*, 97, 104101-10414.

- Weber, N., Lee, Y. S., Shanmugasundaram, S., Jaffe, M., & Arinzeh, T. L. (2010). Characterization and in vitro cytocompatibility of piezoelectric electrospun scaffolds. *Acta Biomaterialia*, 6(9), 3550-3556.
- Wu, J., Wang, Y., & Wang, H. (2014). Phase boundary, poling conditions, and piezoelectric activity and their relationships in $(K_{0.42}Na_{0.58})(Nb_{0.96}Sb_{0.04})O_3-(Bi_{0.5}K_{0.5})_{0.90}Zn_{0.10}ZrO_3$ lead-free ceramics. *RSC Advances*, 4(110), 64835-64842.
- Xu, Q., Chen, X., Chen, W., Chen, S., Kim, B., & Lee, J. (2005). Synthesis, ferroelectric and piezoelectric properties of some $(Na_{0.5}Bi_{0.5})TiO_3$ system compositions. *Materials Letters*, 59(19), 2437-2441.
- Xu, Y. (1991). Ferroelectric Materials and Their Applications. *The Netherlands: North-Holland*.
- Yordanov, S. P., Ivanov, I., & Carapanov, C. P. (1998). Dielectric properties of the ferroelectric ceramics. *Journal of Physics D: Applied Physics*, 31(7), 800-806.
- Yu, T., Kwok, K. W., & Chan, H. L. W. (2007). Preparation and properties of sol-gel-derived $Bi_{0.5}Na_{0.5}TiO_3$ lead-free ferroelectric thin film. *Thin Solid Films*, 515(7), 3563-3566.
- Zhang, R., Yang, Z., Chao, X., & Kang, C. (2009). Effects of CeO_2 addition on the piezoelectric properties of PNW–PMN–PZT ceramics. *Ceramics International*, 35(1), 199-204.
- Zhao, M. L., Wang, C. L., Zhong, W. L., Wang, J. F., & Chen, H. C. (2003). Electrical properties of $(Bi_{0.5}Na_{0.5})TiO_3$ ceramic prepared by sol-gel method. *Acta Physica Sinica*, 52(1), 229-232.
- Zhao, S., Wu, H., & Sun, Q. (2005). Study on PSN–PZN–PZT quaternary piezoelectric ceramics near the morphotropic phase boundary. *Materials Science and Engineering: B*, 123(3), 203-210.
- Zheng, P., Zhang, J. L., Tan, Y. Q., & Wang, C. L. (2012). Grain-size effects on dielectric and piezoelectric properties of poled $BaTiO_3$ ceramics. *Acta Materialia*, 60(13), 5022-5030.
- Zhou, C., Liu, X., Li, W., & Yuan, C. (2009). Dielectric and piezoelectric properties of Y_2O_3 doped $(Bi_{0.5}Na_{0.5})_{0.94}Ba_{0.06}TiO_3$ lead-free piezoelectric ceramics. *Materials Research Bulletin*, 44(4), 724-727.

LIST OF PUBLICATIONS

- N. A. Halim**, T. S. Velayutham, W. H. Abd. Majid. (2016). Pyroelectric, ferroelectric, piezoelectric and dielectric properties of $\text{Na}_{0.5}\text{Bi}_{0.5}\text{TiO}_3$ ceramic prepared by sol-gel method. *Ceramics International* 42, 15664–15670.
- R. I. Mahdi, W. C. Gan, **N. A. Halim**, T. S. Velayutham, W. H. Abd. Majid. (2015). Ferroelectric and pyroelectric properties of novel lead-free polyvinylidene fluoride-trifluoroethylene- $\text{Bi}_{0.5}\text{Na}_{0.5}\text{TiO}_3$ nanocomposite thin films for sensing applications. *Ceramics International* 41, 13836–13843.
- Muhammad Zharfan Mohd Halizan, Nur Adilah Roslan, Shahino Mah Abdullah, **N. A. Halim**, Thamir Selvi Velayutham, Kai Lin Woon, Azzuliani Supangat (2017). Improving the operational voltage of vertical organic field effect transistor (VOFET) by altering the morphology of dielectric layer. *Journal of Materials Science: Materials in Electronics*.ISSN, 4522-4529.